NEW TECHNIQUES IN ASTRODYNAMICS FOR MOON SYSTEMS EXPLORATION

by

Stefano Campagnola

A Dissertation Presented to the
FACULTY OF THE USC GRADUATE SCHOOL
UNIVERSITY OF SOUTHERN CALIFORNIA
In Partial Fulfillment of the
Requirements for the Degree
DOCTOR OF PHILOSOPHY
(AEROSPACE ENGINEERING)

May 2010

To all my mentors,
and especially to my first:
Silvana and Sergio.

Acknowledgments

I would like to thank those who made this thesis possible, starting first and foremost with Paul Newton for his encouragement and guidance since our first meeting. He has offered precious advice throughout my graduate career, and enthusiastically supported my collaborations with many other scholars and colleagues. I owe my deepest gratitude to Ryan Russell for a very fruitful collaboration, and for his tireless support and true friendship. I am also grateful to Martin Lo for helping me start this Ph.D. and for many stimulating conversations.

I would like to thank many of my colleagues at JPL, ESA, and JAXA for sharing their expertise. In particular, I am grateful to Nathan Strange for involving me in his work and offering his ideas and enthusiasm; to Jon Sims, for suggesting I work on endgames; to Anastassios Petropoulos and Arnaud Boutonnet for their valuable input during many meetings.

I am grateful to Jerry Marsden for including me in several research activities in his group and for many productive discussions with him and with his students. In particular, I wish to thank Paul Skerritt, who spent several hours helping me improve my mathematical skills.

I am very indebted to Al Barr for mentoring me in numerous ways I cannot count. His advice has been fundamental not only for the development of this work, but also to my approach to completing it. I will carry his nuggets of wisdom into my future years as a researcher.

I'd like also to thank the Viterbi School of engineering for financial support through the Dean's Fellowship Program, and my committee members: Eva Kanso, Henryk Flashner, Roger Ghanem, Peter Baxendale.

Finally, I wish to express my gratitude to my family and friends for their support and friendship these four years: to my parents Sergio and Silvana and my sister Sonia and Sandrino for their constant support; my Caltech companions Dado, Valerio, and Andrea; my USC fellows Pedro, Tak, Eric, Fangxu, and Babak; the Hellman Avenue crew Jason and Skip; my artist friends Piero and Matt. Last but not least, I am grateful to Ava for her infinite patience, support, and continuous love.

Table of Contents

List of Tables

List of Figures

Abstract

ESA and NASA scientific missions to the Jupiter and Saturn systems will answer fundamental questions on the habitability of icy worlds. The missions include unprecedented challenges, as the spacecraft will be placed in closed, stable orbits near the surface of the moons. This thesis presents methods to design trajectories that tour the moons and ultimately insert the spacecraft into orbits around them, while mitigating the mission costs and/or risks.

A first technique is the endgame, a sequence of moon flyby preceding the orbit insertion. Historically, the endgame is designed with two approaches with different results: the v_∞-leveraging transfer (VILT) approach leads to high-Δv (hundreds of m/s), short time-of-flight (months) endgames, while the multi-body approach leads to low-Δv (tens of m/s), long time-of-flight (years) endgames. This work analyzes and develops both approaches.

We introduce a fast design method to automatically compute VILT endgames, which were previously designed in an ad-hoc manner. We also derive an important simple quadrature formula for the minimum Δv attainable with this approach. This formula is the first important result of this work, as it provides a lower bound for assessment studies.

We explain and develop the complex multi-body approach introducing the Tisserand-Poincaré (T-P) graph, which is the second important result of this work. It provides a link between the two approaches, and shows the intersections between low-energy trajectories around different moons. With the T-P graph we design a five-month transfer between

low-altitude orbits at Europa and Ganymede, using almost half the Δv of the Hohmann transfer.

We then focus on missions to low-mass moons, like Enceladus. We show that non-tangent VILT (an extension of the traditional VILT) significantly reduce the Δv while maintaining a satisfactory transfer time ($<$ 4 years in the Saturn system). With a new design method we compute a 52 gravity-assist trajectory from Titan to Enceladus. The time of flight is 2.7 years, and the Δv is almost 10 times better then the Titan-Enceladus Hohmann-like transfer. This trajectory and the design method are the third important contribution of this work; they enable a new class of missions which were previously considered unfeasible.

Finally we study the capture problem, which seeks chaotic trajectories with multiple orbit insertion opportunities. We explore the solution space extending the design techniques used by ESA for the BepiColombo mission capture to Mercury. Such problems are better modeled in the spatial, elliptic, restricted three-body problem, which we analyze in detail. We define new regions of motions and to compute new families of periodic orbits and their stability properties. This analysis is the fourth important contribution of this work. Finally we show that capture trajectories shadow the manifolds of special periodic and quasi periodic orbits. This is the last important contribution of this report, as if both explains the complex dynamics of capture trajectories, and suggests new ways to design them.

Chapter 1

Introduction

1.1 Motivations

In recent years both NASA and ESA have studied a variety of mission options to the Galilean moons at Jupiter and to the moons of Saturn including Enceladus and Titan. These moons are very interesting for the scientific community; their exploration will help understanding the habitability of icy worlds orbiting giant planets.

On February 2009, NASA and ESA announced their cooperation in the design of the Europa Jupiter System Mission, to be launched around 2020. NASA will design the Europa orbiter, while ESA will design the Ganymede orbiter. JAXA (Japan) and Roscosmos (Russia) might also contribute with the Jupiter Magnetospheric Orbiter and the Europa lander.

In the same year it was announced that the NASA/ESA Titan Saturn System Mission will explore Titan and Enceladus, and is currently planned to be launched sometime in the 2020s. In part as a result of the work presented in this thesis, JPL is also studying mission scenarios for an Enceladus orbiter.

Both missions are very challenging. The long distance from the Sun and the Earth affect all the subsystems, starting with power, thermal and telecommunications. Differently from the spacecraft Voyager 1 and 2, Galileo, and Cassini-Huygens, which successfully explored the outer solar system, the new planned missions include moon orbiters, with an additional set of challenges. The orbit insertion, which place the spacecraft in orbit around the moon, becomes one of the most critical and expensive part of the missions. With the exception of the Titan orbiter, which can use aerobraking techniques, all the other orbiters need to carry large amount of propellant to provide the change in energy (or speed, Δv) for the orbit insertion maneuver.

To mitigate the costs and risks of orbit insertion maneuver, and to enhance the exploration of moon systems, the spacecraft must perform complicated sequences of flyby and impulsive maneuvers. A few of such trajectories were computed in an ad-hoc manner; however, the astrodynamic community is seeking new design methods and new techniques for the computation of more and diverse solutions. By reducing costs and/or risks, these solutions can save the missions from future cancellations.

This thesis study, compare, extend old, and create anew astrodynamic techniques for moon system explorations. The techniques exploit the fast dynamics of the moon systems, where the time scale is on the order of days, rather then of years as in the planet explorations. The results presented in this report are published in conference proceedings and peer-reviewed journals[CR10a, CR10b, CSR10, SCR09, CL08, CLN08].

1.2 Background

In this section we introduce the astrodynamic techniques currently in use to design the mission to the moons.

1.2.1 Endgames and begin-games

The endgame [JD99] is the last part of a trajectory before the insertion maneuver into the science orbit. An example of endgame is the last part of the trajectory to Mercury of the NASA Messenger Mission (see Fig. 1.1). The endgame aims at a low-Δv orbit insertion maneuver. The “begin-game” is the symmetric problem and starts with a low Δv escape from an initial orbit around a minor body. Both strategies have been studied, designed and implemented in space missions with two distinct approaches.

The first approach uses the $v_\infty-$ leveraging transfer (VILT) technique, where the combined effect of gravity assists and impulsive maneuvers (at the almost opposite apsidal point of the spacecraft orbit) changes the spacecraft velocity relative to the minor body[Hol75, SLS97]. Typically the transfer is first computed in the linked-conic model (i.e. the zero-sphere-of-influence, patched-conic model), and then optimized in a real ephemeris model and patched together to the rest of the trajectory. The VILT approach is very intuitive and quickly provides solutions. NASA and ESA use the VILT approach for the design of the endgame trajectories to Europa [JD99, RS07], Ganymede [BdPC] and Titan. The VILT originates and is used frequently with interplanetary trajectories [Hol75, SLS97]. The Messenger mission to Mercury implements a VILT sequence for the endgame at Mercury [MDF$^+$06]; the BepiColombo mission to Mercury implements a low-thrust version of the VILT at Earth and at Mercury [Lan00], followed by a gravitational capture at Mercury [JCGK04]. A The Cassini spacecraft performed a VILT at Venus before the last Earth gravity assist [GGH98]. The Juno mission, targeted to launch in 2011, implements a VILT at Earth to reach Jupiter [KJT08].

The second approach uses the multi-body technique[RL03, SPC99], where small Δvs (if any) are applied when the spacecraft is far from the minor body, typically to target high altitude flyby passages which produce the desired effects (e.g. behind or in front of the minor body to increase or decrease the spacecraft energy). The trajectory is computed directly in the real ephemeris model, or in the restricted three, four, or five body model. This approach cannot be explained with the linked-conics model, where ballistic transfers cannot change the arrival conditions at the minor body. Trajectories are typically found with some heuristic method. Recently, nonlinear dynamical system theory has been used to help the design of endgames or multi-moon orbiters [RS07, GR09] (See Fig 1.2). Usually the multi-body technique results in low-cost trajectories with long times of flight. The Smart1 mission successfully implemented this strategy to get the spacecraft gravitationally captured around the Moon [SPC99].

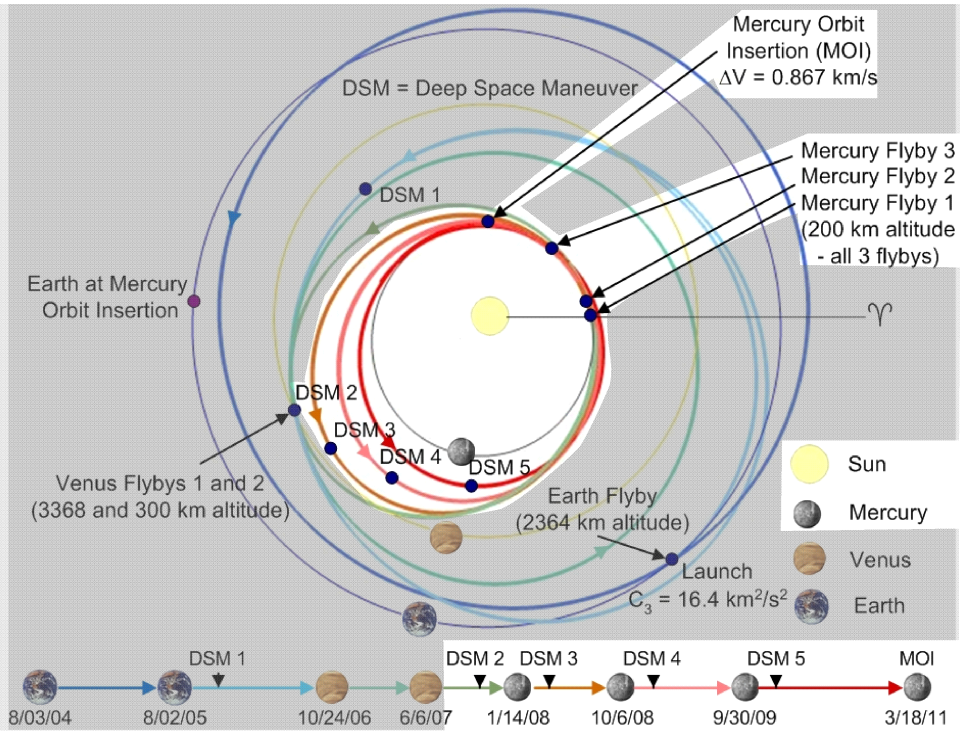

Figure 1.1: Endgame trajectory in the Messenger mission to Mercury (picture from NASA).

1.2.2 Capture trajectories

Capture trajectories allow the spacecraft to approach a moon and to be temporarily captured around it without any insertion maneuver. This feature can be used to explore moons at no additional cost before transferring into another minor body, or to increase the robustness of the orbit insertion maneuver by providing back-up orbit insertion opportunities. An example of capture trajectory is the gravitational capture at Mercury of the ESA BepiColombo mission to Mercury to be launched in 2014 (see Fig. 1.3).

There are two different approaches to the design of capture trajectories. The first approach is a systematic search of the solution space by varying the orbital parameters before the orbit insertion maneuver. This approach was partly implemented at the European Space agency for the design of the nominal trajectory of the BepiColombo Mission to Mercury[JCGK04].

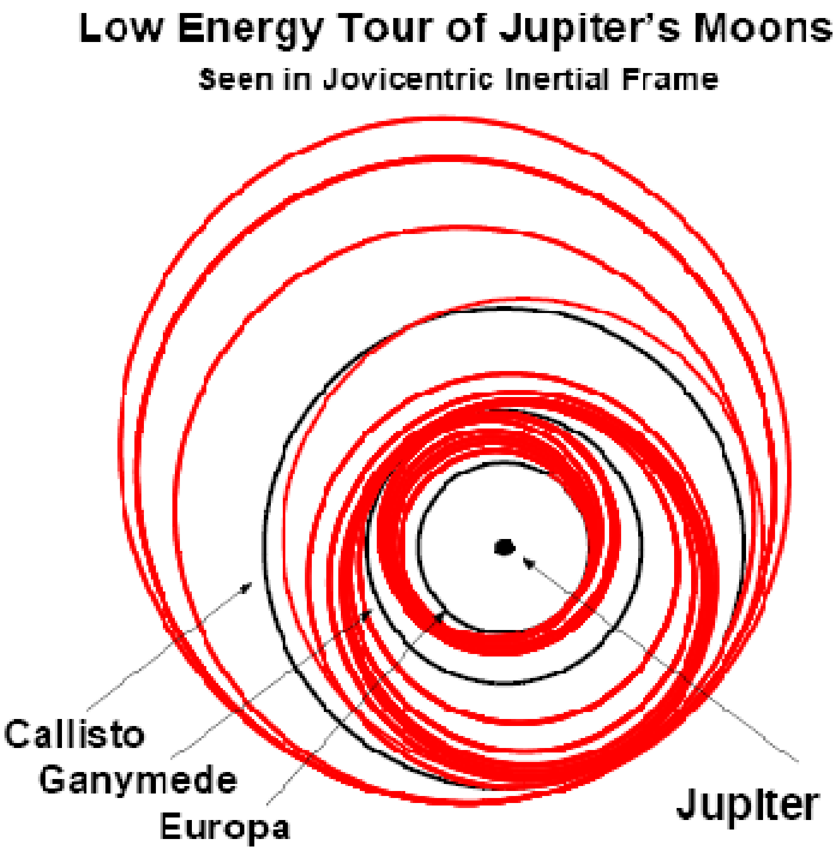

Figure 1.2: Multi-moon Orbiter (From [RL03])

The second approach consists of computing suitable unstable periodic and their manifolds. The periodic orbits are computed in the circular, restricted three-body problem (CR3BP) [RL07, vKZA$^+$05].

1.3 Dissertation overview

Chapter 2 introduces the main mathematical models used in this work. In particular we recall the 2-body problem (2BP), the patched-2BP model, the circular, restricted, 3-body problem (CR3BP) and the patched-CR3BP model.

Chapter 3 and 4 analyze the endgame problems with the two approaches (VILT and multi-body techniques) and draw connections between them. In particular, in chapter

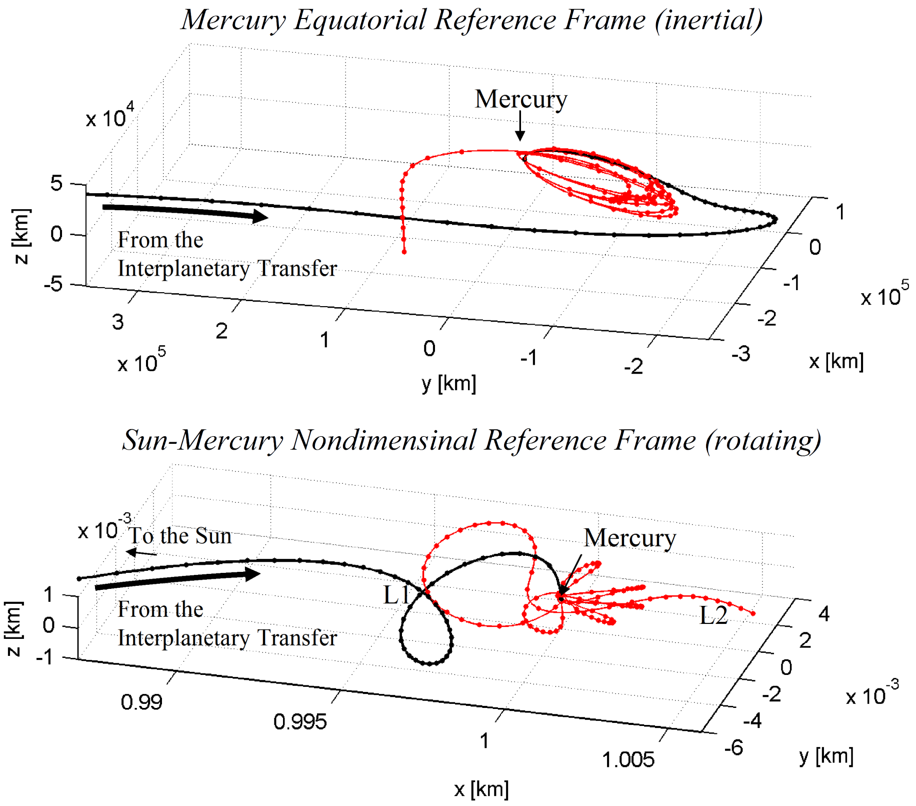

Mercury Equatorial Reference Frame (inertial)

Sun-Mercury Nondimensinal Reference Frame (rotating)

Figure 1.3: Capture trajectory for the BepiColombo mission to Mercury (approved ESA mission to be launched in 2014)

3 we derive new formulae for the VILT and build the leveraging graph to be used as a reference guide for designing endgame tours. We prove that the cost of a VILT sequence decreases when using high altitude flybys (as done in the multi-body technique). Finally we find a simple quadrature formula to compute the minimum Δv transfer between moons using VILTs, which is the main result of the chapter. The leveraging graphs and associated formulae are derived in canonical units and therefore apply to any celestial system with a smaller body in a circular orbit around a primary. Specifically we demonstrate the new method to provide rapid calculations of the theoretical boundary values for Δv requirements for moon tours in the Saturn and Jupiter systems using the VILT model.

In chapter 4 we focus on the multi-body approach using a new graphical tool, the Tisserand-Poincaré (T-P) graph. The T-P graph shows that ballistic endgames are energetically possible and it explains why they require resonant orbits patched with high altitude flybys, whereas in the VILT approach flybys alone are not effective without impulsive maneuvers in between them. We then use the T-P graph to design quasi-ballistic transfers. Unlike previous methods, the T-P graph provides a valuable, energy-based, target point for the design of the endgame and begin-game, and a simple way to patch them. We finally present two transfers. The first transfer is between low-altitude orbits at Europa and Ganymede using almost half the Δv of the Hohmann transfer; the second transfer is a 300-day quasi-ballistic transfer between halo orbits of the Jupiter-Ganymede and Jupiter-Europa. With approximately 50 m/s the transfer can be reduced by two months.

In chapter 5 we focus on tour of low-mass moons. In such systems the strategies presented in the previous chapter lead to too long transfers. For this reason, we had to extend the theory of chapter 3 and study non-tangent (or generalized) VILTs. We start studying the solution space of the generalized VILT and to derive a linear approximation which greatly simplifies the computation of the transfers. Using this approximation, Tisserand graphs, and a heuristic optimization procedure we introduce a fast design method for multiple-VILT tours. We use this method to design a trajectory from a highly eccentric orbit around Saturn to a 200 km science orbit at Enceladus. The trajectory is then recomputed removing the linear approximation, showing a Δv change of less than 4%. The trajectory is 2.7 years long and comprises 52 gravity assists at Titan, Rhea, Dione, Tethys, and Enceladus, and several deterministic maneuvers. Total Δv is only 445 m/s , including the Enceladus orbit insertion, almost 10 times better then the 3.9 km/s of the Enceladus orbit insertion from the Titan-Enceladus Hohmann transfer. The new method and demonstrated results in this chapter enable a new class of missions that tour and ultimately orbit small mass moons. Such missions were previously considered infeasible due to flight time and Δv constraints.

In chapters 6 and 7 we study the capture problem. The capture problem is more affected by the science orbit constraints, and less by the time scale. Because the science orbit constraints for the mission to the Jupiter and Saturn systems are currently under definition, we consider the capture problem for a mission to Mercury, where the constrains on the science orbit are given. In chapter 6 we define regions of motion and periodic orbits in the ER3BP. A deep understanding of the ER3BP is required for the design of capture trajectories at Mercury presented in the next chapter. We replace the Hill's zero-velocity surfaces in the CR3BP by the low-velocity regions, which divides the subregions of motion from the forbidden subregions. We compute periodic trajectories using a continuation method, starting with orbits in the CR3BP with period synchronous to the period of the primaries. We show that different branches of periodic orbits bifurcates in the ER3BP and that the new branches have different linear stability properties.

In Chapter 7 we present two approaches to the design of capture trajectories. We first develop and use the dedicated software tool GraCE to explore the solution space. Then we reproduce the BepiColombo trajectory in the model of the elliptic restricted three body problem, showing that it follows the stable and unstable manifolds of quasi-periodic orbits. In particular, we show that the manifolds of a symmetric quasi-periodic orbit around Mercury play a key role as their symmetry properties provide several recovery opportunities to the mission.

Chapter 2

Models

In this chapter we recall the mathematical models. Throughout this work we use the tilde for dimensional variables.

2.1 The 2-body problem and the linked-conics model

2.1.1 The 2-body problem

The 2-body problems studies the motion of two bodies moving under their gravitational attraction. The position of the second body $\tilde{m}_2$ relative to the first body $\tilde{m}_1$ is defined by the equations of motion

$$\ddot{\tilde{r}}_{12} = -\frac{G\left(\tilde{m}_1 + \tilde{m}_2\right)}{\tilde{r}_{12}^3}\tilde{\mathbf{r}}_{12} \tag{2.1}$$

where $\tilde{\mathbf{r}}_{12}$ is the position of the second body with respect to the first body, and G is the universal gravitational constant.

The *restricted* problem assumes that the one of the two body (M) has much smaller mass then the other (P), so that Eq. 2.1 can be written as

$$\ddot{\tilde{\mathbf{r}}} = -\frac{\tilde{\mu}_P}{\tilde{r}^3}\tilde{\mathbf{r}} \tag{2.2}$$

where $\tilde{\mu}_P = G\tilde{m}_P$ is the gravitational constant of the body P, and $\tilde{\mathbf{r}}$ is the position of M in the inertial reference frame centered in P. The energy per unit mass of the second body is

$$\tilde{E} = \frac{1}{2}\left\|\tilde{\mathbf{v}}\right\|^2 - \frac{\tilde{\mu}_P}{\left\|\tilde{\mathbf{r}}\right\|} = -\frac{\tilde{\mu}_P}{2\tilde{a}}$$

The momentum is

$$\tilde{\mathbf{h}} = \tilde{\mathbf{r}} \times \tilde{\mathbf{v}}$$

The eccentricity vector is

$$\mathbf{e} = \frac{\|\tilde{\mathbf{v}}\|^2 \, \tilde{\mathbf{r}}}{\tilde{\mu}_P} - \frac{(\tilde{\mathbf{r}} \cdot \tilde{\mathbf{v}})\tilde{\mathbf{v}}}{\tilde{\mu}_P} - \frac{\tilde{\mathbf{r}}}{\|\tilde{\mathbf{r}}\|}$$

The motion in the orbital reference plane, with the z-axis aligned with the momentum and the x axis aligned with the eccentricity vector, is defined in polar coordinates by

$$\tilde{r} = \frac{\tilde{h}^2/\tilde{\mu}_P}{1 + e\cos f}$$

where f is the true anomaly. We also recall the definition of pericenter and apocenter for elliptical orbits

$$\tilde{r}_p = \tilde{a}\,(1-e) \quad \tilde{r}_a = \tilde{a}\,(1-e)$$

and, for hyperbolic orbits, the velocity at infinity and deviation angle

$$\tilde{v}_\infty = \sqrt{2\tilde{E}}$$

$$\delta = 2 \arcsin\left(\frac{\tilde{\mu}_P}{\tilde{\mu}_P + \tilde{r}_p \tilde{v}_\infty^2}\right) \tag{2.3}$$

Figure 2.1 shows the orbital plane and the associated orbital parameters: the inclination i, the right ascension of the ascending node RAAN, and the argument of pericenter ω . Figure 2.2 on the left shows the pericenter, apocenter and semi-major axis of the elliptic orbit; on the right, the semi-major axis, pericenter, deviation angle and v_∞ of a hyperbolic orbit.

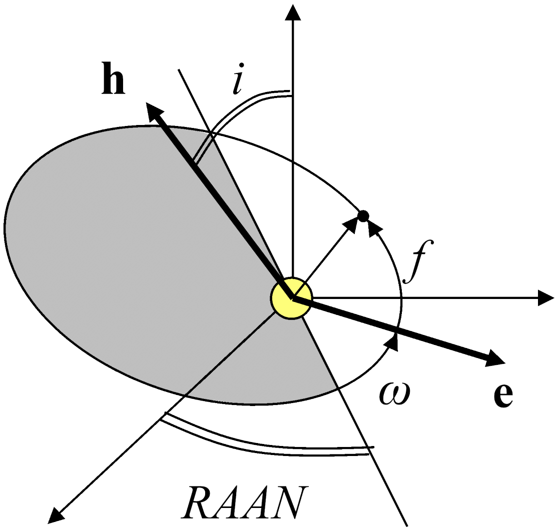

Figure 2.1: The orbital parameters solution of the 2-body problem

2.1.2 Sphere of influence, gravity assists and linked-conics model

The sphere of influence of a minor body M orbiting a major body P is the region in space where the gravitational attraction due to M dominates the gravitational attraction due to P. This regions is called sphere of influence and has a radius

$$\tilde{r}_{SOI} = \tilde{a}_M \left(\frac{m_M}{m_P} \right)^{2/5}$$

The flyby is a technique by which a spacecraft orbiting P can change its orbital parameter with respect to a major body by using the gravitation attraction of a minor body M. Figure 2.3 shows the flyby of a spacecraft and the sphere of influence.

The gravity assist is similar in definition to a flyby, except that usually the spacecraft closest approach to the minor body is well within the sphere of influence.

Gravity assists can be modeled as an instantaneous change in the velocity of the spacecraft, as shown in Figure 2.4 , satisfying the equations

$$\left\|\mathbf{v}_{\infty}^{out}\right\| = \left\|\mathbf{v}_{\infty}^{in}\right\| = v_{\infty} \tag{2.4}$$

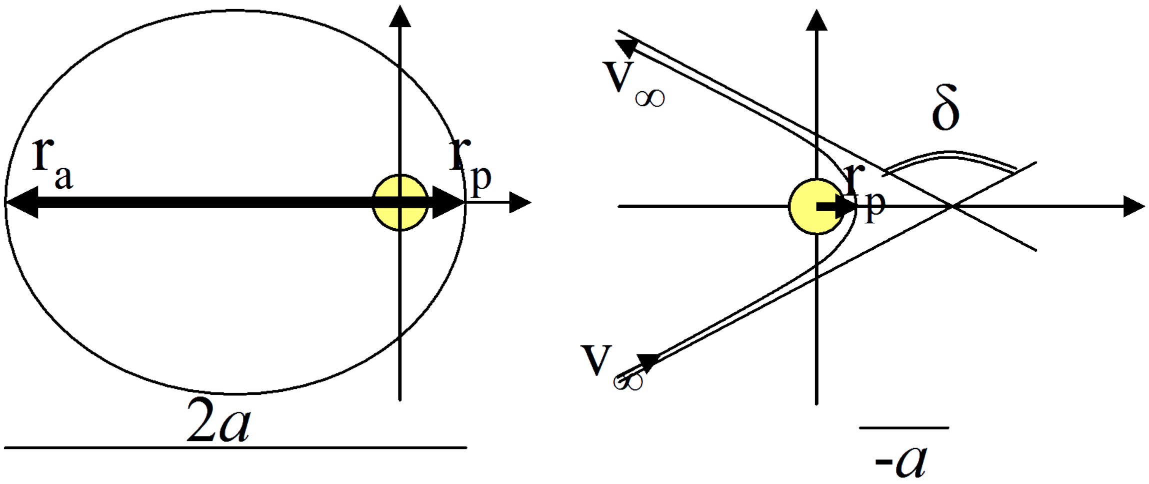

Figure 2.2: On the left, the semi-major axis, pericenter and apocenter of an elliptic orbit. On the right, the semi-major axis, v_∞ and deviation angle of a hyperbolic orbit.

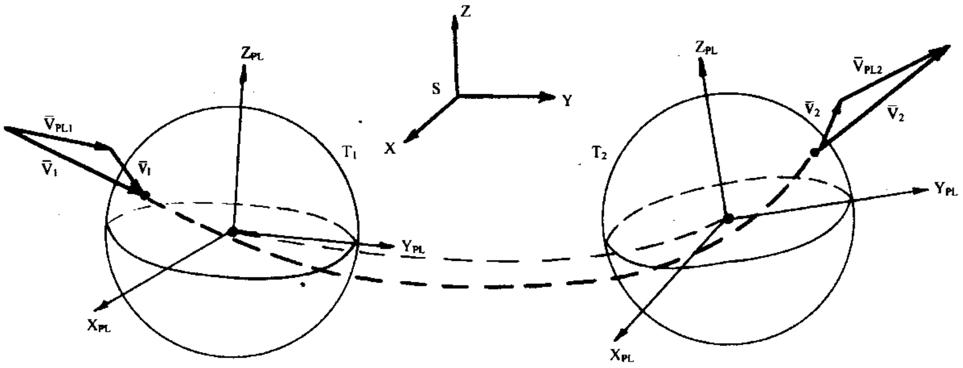

Figure 2.3: Flyby and the sphere of influence (from [LPS98])

$$< \mathbf{v}_\infty^{in}, \mathbf{v}_\infty^{out} >= v_\infty^2 \cos\delta \tag{2.5}$$

where δ is defined in Eq. 2.3.

The linked-conics model is a commonly used model in the design of interplanetary trajectories. The idea is to represent a trajectory as a sequence of conic sections, which are solution of the equation 2.2. Conic arcs are patched by instantaneous changes of velocities, provided by gravity assists or impulsive maneuvers performed with on-board thrusters.

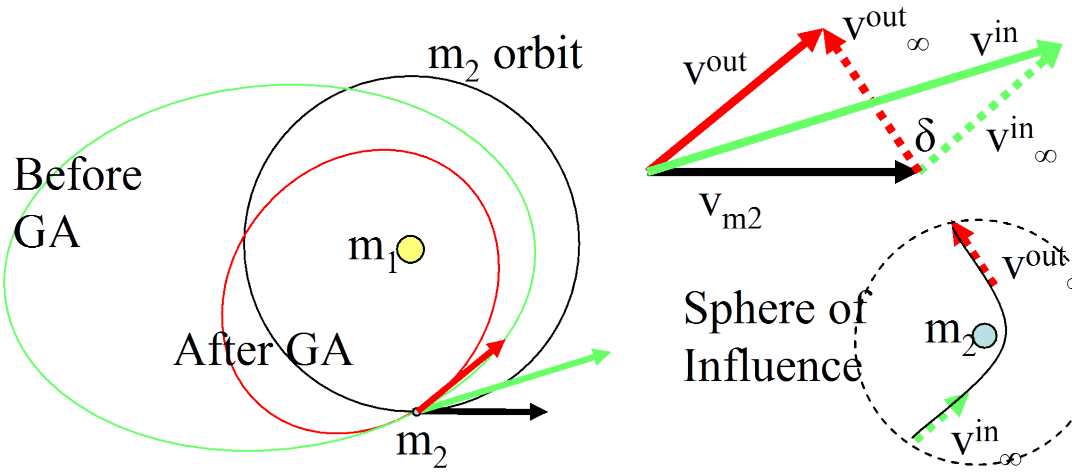

Figure 2.4: Gravity assist modeled as instantaneous change of the spacecraft velocity.

2.2 The circular, restricted 3-body problem and the patched-CR3BP model

2.2.1 The circular, restricted 3-body problem

In this section we briefly recall some key features of the circular restricted three body problem[Sze67a]. In the *general* restricted three-body problem, an infinitesimal mass moves under the gravitational attraction of two primaries P and M ($\tilde{m}_M < \tilde{m}_P$), without affecting them. The motion of the infinitesimal mass is usually described in a nondimensional, rotating reference frame, where the position of the primaries is fixed along the $X-axis$ (also called the *syzygy* axis) and their mutual distance is normalized to 1; the Z-axis is perpendicular to the primary orbit, and we call the XZ plane the *normal plane.*

In the *circular* restricted three body problem (CR3BP), the primaries move on circular orbits. Using the scale factors

$$l^* = \tilde{a}_M, \qquad t^* = \sqrt{\frac{\tilde{a}_M^3}{\tilde{\mu}_P + \tilde{\mu}_M}} \qquad m^* = \tilde{m}_M + \tilde{m}_P$$

the equation of motion for the spacecraft in the rotating frame are [Sze67a]

$$\begin{cases} \ddot{X} - 2\dot{Y} & = & \frac{\partial \Omega}{\partial X} \\ \ddot{Y} + 2\dot{X} & = & \frac{\partial \Omega}{\partial Y} \\ \ddot{Z} & = & \frac{\partial \Omega}{\partial Z} \end{cases} \tag{2.6}$$

$$\Omega(X,Y,Z) \equiv \frac{1}{2}\left(X^2+Y^2\right) + \frac{1-\mu}{R_1} + \frac{\mu}{R_2} + \frac{1}{2}\left(1-\mu\right)\mu \tag{2.7}$$

where $R_1 = \sqrt{\left(X+\mu\right)^2 + Y^2 + Z^2}$ and $R_2 = \sqrt{\left(X+\mu-1\right)^2 + Y^2 + Z^2}$ are the distances to the primaries, and $\mu = \mu_M = \frac{\tilde{m}_M}{\tilde{m}_M + \tilde{m}_P}$ is the mass parameter. It is well known [Jac36, Sze67b] that the system of Eq. (2.6) has one integral of motion, the Jacobi constant[1]

$$J = 2\Omega - V^2 = \left(X^2+Y^2\right) + 2\frac{1-\mu}{R_1} + 2\frac{\mu}{R_2} + \left(1-\mu\right)\mu - V^2 \tag{2.8}$$

where $V^2 = \left(\dot{X}^2 + \dot{Y}^2 + \dot{Z}^2\right)$ is the velocity in the rotating frame. The Jacobi constant is used to define regions of motion. The system of Eq. (2.6) has five fixed points, the Lagrangian points $L_i, i = 1, \ldots, 5$. The positions of the Lagrangian points depend on the parameter μ.

Transfer trajectories are possible only if $J_C < J_{L1}$, where $J_{L1}(\mu)$ is the Jacobi constant associated to the first libration point.

2.2.2 Zero velocity surfaces

Hill used Eq. (2.8) to define zero-velocity surfaces which separate regions of motion from the forbidden regions[Hil78]. Given a set of initial condition $(t_0, \mathbf{X}_0)$, Hill's zero-velocity surfaces are level sets of $2\Omega_C$:

$$2\Omega_C = J_C(\mathbf{X_0})$$

---

[1] The Hamiltonian $\mathcal{H}$, which is time-independent and is therefore an integral of motion, is related to the Jacobi constant: $2\mathcal{H} = -J_C + \mu\left(1-\mu\right)$.

If the initial conditions are such that $J_C < 3$, the motion of the third body in the xy plane is unbounded. If the initial conditions are such that $J_C > J_{L1}$, the motion of the third body is bounded around either of the primary, or far away from both. Figure 2.5 shows the zero-velocity surfaces for the Pluto-Charon system.

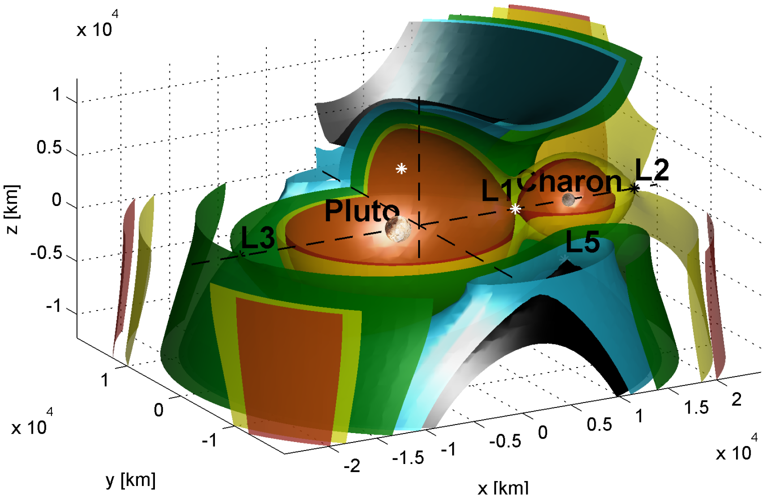

Figure 2.5: Level sets of the function 2Ω in the Pluto-Charon system ($\mu \simeq 0.123$). In the circular restricted three-body problem, the level sets are the Hill's zero-velocity surfaces, and separate regions of motion from the forbidden regions.

2.2.3 Periodic orbits

A fundamental step in understanding any dynamical system is to identify its periodic orbits and classify their linear and nonlinear stability [Poi92]. For a fixed value of the mass parameter μ, the CR3BP possesses *families* of periodic orbits parametrized by the Jacobi constant J_C , as implied by the Cylinder Theorem[Mey99]:

> An elementary periodic orbit of a system with an integral I lies in a smooth cylinder of solutions parametrized by I.

Several authors computed families of periodic orbits in the CR3BP [Con68, BB79, DRP$^+$07, Góm79, How84]. In this work we use orbits of the halo orbit families. Their linear stability is determined by computing the linear map

$$\varphi_C : \delta\mathbf{X}(t_0) \to \delta\mathbf{X}(T + t_0) = M\delta\mathbf{X}(t_0)$$

between consecutive crossings through a Poincar section. Here $\delta\mathbf{X}(t_0)$ is an arbitrary initial perturbation of the state $\mathbf{X} = [X, Y, Z, U, V, W]$, M is the monodromy matrix and T is the principal period of the orbit. The stability of the map φ, and hence of the orbit, is related to the eigenvalues λ of the monodromy matrix M: eigenvalues inside the unit circle ($\lambda < 1$) are associated to the stable manifold W_s ; eigenvalues outside the unit circle are associated to the unstable manifold W_u ; and pure imaginary eigenvalues are associated with tori of quasi periodic orbits.

In the restricted three-body problem, the eigenvalues λ of the monodromy matrix come in reciprocal pairs, so that the periodic orbit is linearly stable if and only if all the eigenvalues are on the unit circle. Also, in the CR3BP two eigenvalues are real unitary, and are associated to eigenvectors $\delta\mathbf{X}_0$ tangent to the trajectory: because the system is autonomous, such perturbation corresponds to a small phase change along the orbit.

2.2.4 The patched, CR3BP model

The patched CR3BP model is an approximation of an n-body problem, where the mass of the spacecraft is negligible, and where at any time only two gravitational body are affecting its motion. The spacecraft trajectory is approximated by a sequence of trajectories, each one solution of the system of Eq. 2.6 for a choice of the major and minor body. For instance, a trajectory flying by Europa and Ganymede can be split in two parts: the first is well approximated by a solution of the Jupiter-Europa-spacecraft CR3BP, the second is well approximated by a solution of the Jupiter-Ganymede-spacecraft CR3BP.

Chapter 3

The endgame problem using the v_∞-leveraging technique and the leveraging graph

In this Chapter and in the next one we study the endgame transfers and show the connections between two different approaches: the v_∞-leveraging transfer (VILT) approach, which uses a patched 2-body problem model, and the multi-body approach which uses multibody dynamics. This chapter studies the anatomy of the VILT.

In the first section we derive formulae to show that VILTs are efficient only for v_∞ greater than a minimum value. In the second section we use the formulae to introduce the leveraging graph, which has broad endgame design applications. Based on the graph we demonstrate a branch and bound search to globally explore the flight time vs. Δv solution space. The canonical form of the leveraging graphs and formulae are applicable to any planet system or moon system modeled as a smaller body in a circular orbit around a primary. A simple scaling transforms the problem to any dimensioned system of interest. In the third section we define and study the efficiency of the VILT. We prove that the cost of a sequence of VILTs decreases when using high altitude gravity assists (as done when using the multi-body technique). Finally we find the theoretical minimum Δv for transfer between moons computed using the VILT approach. This new design capability is the main result of this chapter.

In the next chapter, we will focus on the multi-body technique and will explain the connection to the VILT approach.

Nomenclature

a_M	Semi-major axis of the minor body (=1 in nondimensional units).
A/B	Point in the spacecraft trajectory where the impulsive maneuver takes place. The point A belongs to the orbit ending / starting at L, the point B belongs to the orbit ending/starting at H.
E/I	Superscript indicates the quantity is referred to an exterior/interior VILT.
h_π	Altitude of the spacecraft's closest approach to the minor body.
$H^{\pm}$	Points of the $v_\infty-$leveraging transfer where the spacecraft orbit crosses the minor-body orbit. There are two possible crossings: H^+ corresponds to the longer transfer and H^- corresponds to the shorter transfer. Subscripts indicate a quantity evaluated at the corresponding point.
L	Point of the $v_\infty-$leveraging transfer (VILT) where the spacecraft orbit is tangent to the minor body orbit with a low relative velocity $v_{\infty L}$. Subscript indicates a quantity evaluated at this point.
$n:m_K^{\pm}$	$v_\infty-$leveraging transfer classification. n is the number of moon revolutions, m is the number of spacecraft revolutions, K is the number of full revolutions in the arc HB, ± refers to the long/short transfer.
P/M	Subscript indicates the quantity is referred to the major body (P) or minor body (M).
r_A	Distance from the point A, B to the major body.
r_M	Radius of the minor body.
v_c	Velocity of the spacecraft at a circular orbit with altitude h_π around a moon with gravitational constant μ_M.

v_M	Velocity of the minor body with respect to the major body (=1 in nondimensional units).
v_∞	Relative velocity of the spacecraft at the minor body.
$v_{\infty H}$	Velocity of the minor body relative to the major body at the point H.
$v_{\infty L}$	Velocity of the minor body relative to the major body at the point L.
v_π	Velocity of the spacecraft with respect to the minor body at the pericenter of the hyperbola.
Δv_{AB}	Impulsive transfer at the point A, B.
μ	Gravitational constant.
$\tilde{x}$	Tilde indicates dimensional variable.
$\pm$	In the formulae, the plus sign is used for exterior VILTs and the minus is used for the interior VILT. If superscript of H, it refers to the long/short transfer.

3.1 v_∞−leveraging

A v_∞−leveraging transfer (VILT) is a technique by which a spacecraft orbiting around a major body (P) can change its speed relative to a minor body (M) [Hol75, SLS97]. The technique consists of a gravity assist and a small impulsive maneuver (Δv_{AB}) that occurs at opposite apses in the spacecraft orbit around the major body (see Figure 3.1) . VILTs are typically modeled in the linked-conic model (or zero-sphere-of-influence, patched-conic model) where the minor body is considered massless and is on a circular orbit around the major body. The spacecraft trajectory is coplanar and starts and ends at the minor body. The gravity assist is modeled as an instantaneous change in the direction of v_∞ vector by angle δ.

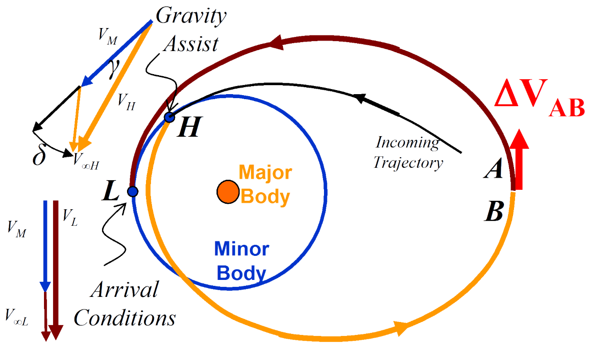

Figure 3.1: Example of a v_∞−leveraging transfer (VILT) to reduce the relative velocity at a minor body: The spacecraft approaches the minor body tangentially and the gravity assist at H rotates the relative velocity $v_{\infty H}$ of an angle δ. At the apocenter of the new orbit (point B), the impulsive maneuver Δv_{AB} changes the shape of the spacecraft orbit so that it becomes tangent again to the minor body orbit at the point L. Although the maneuver actually increases the spacecraft energy, at the point L the spacecraft has a new relative velocity $v_{\infty L} < v_{\infty H}$.

3.1.1 Nondimensional variables

Throughout this chapter we will use nondimensional variables, so that the results are general and can be applied to any endgame problem. To obtain the nondimensional variables we divide the dimensional variable (denoted with the tilde) by the time and length scale factors

$$l_{scale} = \tilde{a}_M \qquad t_{scale} = \sqrt{\frac{\tilde{a}_M^3}{\tilde{\mu}_P}}$$

Then the velocity scale factor becomes the velocity of the minor body $\tilde{v}_M$, and the nondimensional velocity, the semi-major axis of the minor body, and the gravitational constant of the major body are one.

We also define v_c as the nondimensional velocity of the circular orbit of radius $\tilde{r}_\pi = \tilde{r}_M + \tilde{h}_\pi$ around the minor body

$$v_c = \sqrt{\frac{\tilde{\mu}_M}{\tilde{r}_\pi}}/\tilde{v}_M$$

This nondimensional parameter groups the problem dependency on the minor body gravity constant, minor body radius and altitude of the final/initial orbit insertion/escape.

In nondimensional units, the gravity assist deflection angle is

$$\delta = 2 \arcsin \left(1 / \left(1 + (v_\infty / v_c)^2 \right) \right) \tag{3.1}$$

and the spacecraft velocity at the closest approach to the minor body, v_π, is

$$v_\pi \left(v_\infty, h_\pi \right) = \sqrt{v_\infty^2 + 2 v_c^2} \tag{3.2}$$

3.1.2 VILT model and classification

In this section we refer to Figures 3.2 and 3.3 to define the general variations and associated relevant variables of the VILT. We assume that the impulsive maneuver is tangential and is performed exactly at the apses. This assumption is typically included when studying VILTs because the Jacobi constant in the rotating frame is maximally changed by performing the maneuver when the rotating velocity is the greatest - this occurs at apses [Swe93]. We also assume that the spacecraft departs/arrives at point L tangent to the minor body orbit. This condition guarantees the lowest $v_{\infty L}$ [VC09] and greatly simplifies the tour problem because we can decouple each VILT as opposed to having to optimize a large sequence of VILTs altogether.

We divide the trajectory into two legs ($A - L$ and $B - H$) joining four different states of the spacecraft (L,A,B,H). At the point L the spacecraft is at an apse with a relative velocity $v_{\infty L}$ with respect to the minor body. At the point A the spacecraft is at the opposite apsidal point, at a distance r_A from the major body and with a velocity v_A. In between states A and B the spacecraft performs the impulsive maneuver $\Delta v_{AB} = |v_A - v_B|$. At the point H^+ *or* H^- the spacecraft intersects the minor body orbit with a relative velocity $v_{\infty H} > v_{\infty L}$.

We recall from the literature [SLS97] that there are four types of $v_\infty-$leveraging transfers, depending on the following features:

- *forward (backward)* if the Δv_{AB} is in the same (opposite) direction of the spacecraft velocity.
- *exterior (interior)* if the Δv_{AB} occurs at apocenter (pericenter) , thus if $r_A > a_M$ ($r_A < a_M$).

From these definitions it follows that the forward-exterior $v_\infty-$leveraging and backward-interior $v_\infty-$leveraging *decrease* the v_∞, while the forward-interior $v_\infty-$leveraging and backward-exterior $v_\infty-$leveraging *increase* the v_∞.

From our definitions it also follows that

$$v_L^{(E,I)} = 1 \pm v_{\infty L} \tag{3.3}$$

$$v_A^{(E,I)} = v_B \pm \Delta v_{AB} \tag{3.4}$$

where the upper sign refers to the exterior VILT and the lower sign refers to the interior VILT. Note that from these definitions and from Figure 3.2 we find boundary values for v_∞. In particular, $0 < v_{\infty L} < \sqrt{2} - 1$ for the exterior VILT for r_A to be bounded, and $0 < v_{\infty L} < 1$ for the interior VILT for v_L to be positive.

For each type of VILT we also specify:

- the resonant ratio: $n : m$, where n (m) is the approximate number of the minor body (spacecraft) revolutions during the VILT.
- K, the number of full revolutions in the arc $H - B$ [1].
- the point H^-or H^+ where the spacecraft encounters the minor body, resulting in a *long-transfer* VILT or *short-transfer* VILT respectively. Exterior, long-transfer

---

[1] In literature we can find a different choice of letters: $K : L(M)^\pm$ where $K \equiv n$, $L \equiv m$, and $M \equiv K$ for exterior VILT

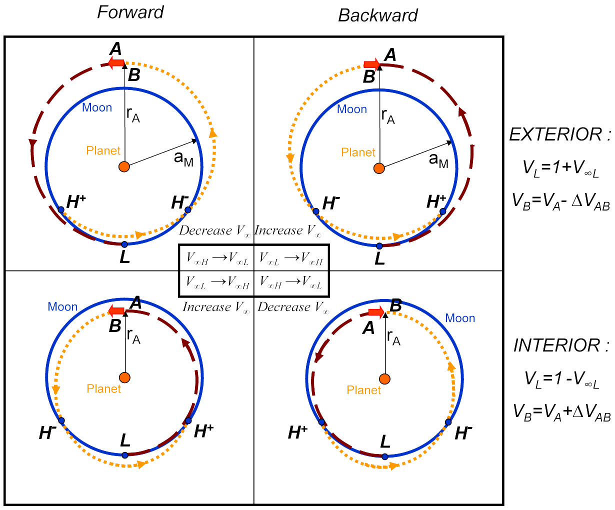

Figure 3.2: Four variations of the $v_\infty-$leveraging transfer (VILT).

> VILTs and interior, short-transfer VILTs are linked by prograde gravity assists. Exterior, short-transfer VILTs and interior, long-transfer VILTs are linked by retrograde gravity assists.

As an example, Figure 3.3 shows the schematic of a $5:4^+$ and of a $5:4^-$VILT. In the rest of the chapter we refer to “backward/forward, interior/exterior $n:m_K^\pm$” VILTs. For example the Europa endgame when approached from Ganymede is a sequence of forward exterior VILTs.

3.1.3 Phase-free formulae

In this section we present a general formulation that is valid for all the four types of VILT. We start by considering the phase-free problem that does not require the spacecraft and the minor body to be at the points L and $H^\pm$ at the same time. The formulae presented in this section are new and allow us to perform many useful, fast, preliminary and global analyses which we present in the next sections. The details of the following calculations are in appendix A.

We first define the function

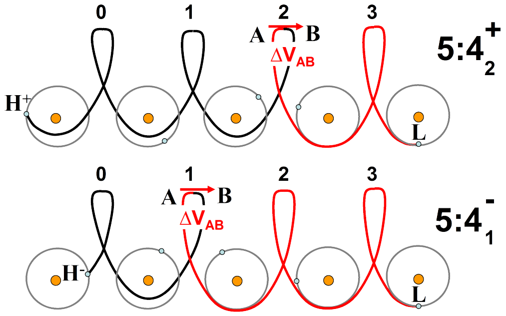

Figure 3.3: Schematic of two different $5:4$ VILTs. In one case the Δv_{AB} occurs after two full revolutions of the spacecraft on the leg $H^{+}-B$. Also, the transfer lasts a bit more than 5 revolutions of the minor body; hence the notation $5:4_{2}^{+}$. In the other case the Δv_{AB} occurs after one full revolution of the spacecraft on the leg $H^{-}-B$. Also, the transfer lasts a bit less than 5 revolutions of the minor body; hence the notation $5:4_{1}^{-}$.

$$\Gamma^{(E,I)}\left(v_{\infty L}\right) \equiv \pm\left(r_{A}-v_{A}\right)=v_{\infty L}\frac{v_{\infty L}^{3} \pm 3v_{\infty L}^{2}-v_{\infty L} \mp 7}{v_{\infty L}^{3} \pm 3v_{\infty L}^{2}+v_{\infty L} \mp 1}$$

where $\Gamma^{(E)}$ is computed for the exterior VILT , and $\Gamma^{(I)}$ for the interior VILT. If no distinction is necessary we simply refer to Γ. We can show that Γ is a positive strictly monotonic function of v_{∞}. Later, we will see that Γ is convenient because it provides a minimum bound on v_{∞} values where VILTs are useful.

With this notation we can explicitly state the high relative velocity $v_{\infty H}$ as a function of the low relative velocity $v_{\infty L}$ and of the Δv_{AB}

$$v_{\infty H}\left(v_{\infty L}, \Delta v_{AB}\right)=\sqrt{\left(v_{\infty L}\right)^{2}+\left(\Delta v_{AB}\right)^{2}+2\Delta v_{AB}\Gamma} \tag{3.5}$$

Equivalently , we can explicitly state the Δv_{AB} as a function of the high and low relative velocity

$$\Delta v_{AB}\left(v_{\infty L}, v_{\infty H}\right)=-\Gamma+\sqrt{\Gamma^{2}+\left(v_{\infty H}^{2}-v_{\infty L}^{2}\right)} \tag{3.6}$$

Finally we define the *phase-free efficiency* of the VILT. The phase-free efficiency of backward-interior or forward-exterior VILT ϵ_{BI-FE} is the increase of the final relative velocity $v_{\infty H}$ due to a change in cost Δv_{AB}, for a fixed initial relative velocity $v_{\infty L}$

$$\epsilon_{BI-FE} \equiv \frac{\partial v_{\infty H}}{\partial \Delta v_{AB}} \equiv D_2 v_{\infty H} = \frac{\Delta v_{AB} + \Gamma}{v_{\infty H}\left(v_{\infty L}, \Delta v_{AB}\right)} \tag{3.7}$$

where D_i is the derivative with respect to the $i-th$ argument. The *phase-free efficiency* of a backward-exterior or forward-interior VILTs ϵ_{BE-FI} is the decrease of the final relative velocity $v_{\infty L}$ due to a change in cost Δv_{AB}, for a fixed initial relative velocity $v_{\infty H}$

$$\epsilon_{BE-FI} \equiv -\frac{\partial v_{\infty L}}{\partial \Delta v_{AB}}$$

We derive an expression for ϵ_{BE-FI} by first taking the partial derivative of $v_{\infty H}$ with respect to $v_{\infty L}$

$$D_1 v_{\infty H} \equiv \frac{\partial v_{\infty H}}{\partial v_{\infty L}} = \frac{v_{\infty L} + \Delta v_{AB} \frac{d\Gamma}{dv_{\infty L}}}{v_{\infty H}\left(v_{\infty L}, \Delta v_{AB}\right)} \tag{3.8}$$

We then use the Implicit Function Theorem[AMR88] to compute

$$\epsilon_{BE-FI} = -\frac{\partial v_{\infty L}}{\partial \Delta v_{AB}} = D_2 v_{\infty H} \circ \left[D_1 v_{\infty H}\right]^{-1} = \frac{\Delta v_{AB} + \Gamma}{v_{\infty L} + \Delta v_{AB} \frac{d\Gamma}{dv_{\infty L}}} \tag{3.9}$$

3.1.4 Phase-fixed solutions

In this section we restore the phasing constraint and introduce the concept of leveraging graphs. A numerical solution to this constrained problem can be computed using an algorithm described by Sims et al. [SLS97]. In general, given $v_{\infty H}$:

- We assume the minor body and the spacecraft are both at the point H at time t_H;
- We guess the flight-path angle γ at H (see Figure 3.1), and find the orbital parameters of the leg $H-B$.
- We compute the orbital parameters of the leg $L-A$ with apses at L and r_A.
- We compute the transfer time and the time t_L when the spacecraft is at L

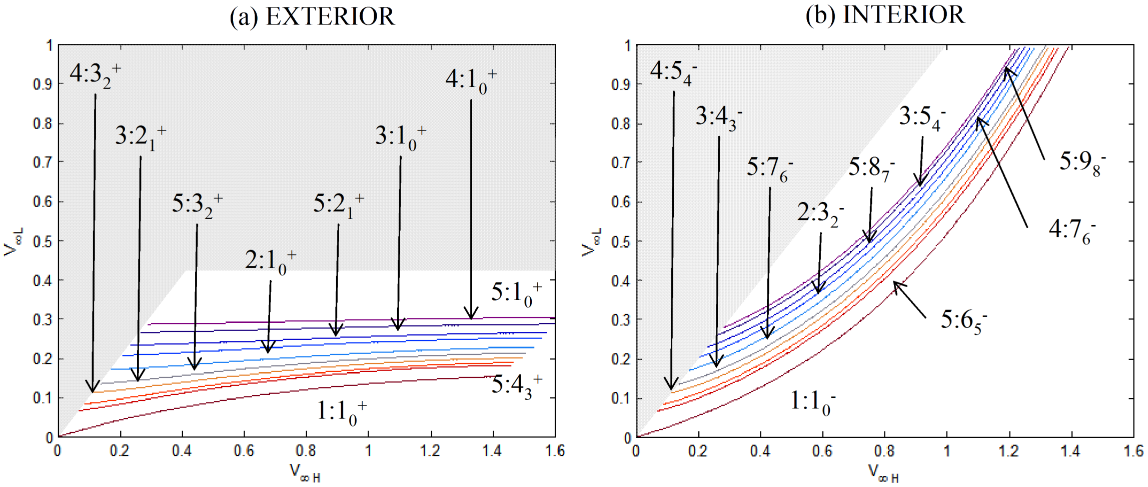
(a) EXTERIOR

(b) INTERIOR

Figure 3.4: $(v_{\infty L} - v_{\infty H})$ leveraging graph for the exterior (a) and interior (b) VILT. for each resonance $n : m$ we only plot the VILT $n : m^{+}_{m-1}$, which we show to be the most efficient. The domain of feasible $v_{\infty L}$ is discussed in the previous section.

- We compute the distance from the point L to the position of the minor body at time t_L and differentially correct the flight-path angle γ until the distance vanishes.

The numerical solutions to the VILT problem are one set of $v_{\infty H}$ $(v_{\infty L})$ curves for exterior $n : m^{\pm}_{K}$ VILTs, and one set of $v_{\infty H}$ $(v_{\infty L})$ curves for the interior $n : m^{\pm}_{K}$ VILTs. We plot these solutions on a special graph , which we call $(v_{\infty L} - v_{\infty H})$ *leveraging graph.* We can also plot these solutions using other variables related to v_{∞}, thus defining different leveraging graphs. In the next section we build and use the *Tisserand leveraging graph.* Following this definition, the graphs in literature can be referred as $(r_{aphelion} - v_{\infty Earth})$ *leveraging graph* or $(r_{aphelion} - \Delta v_{TOT})$ *leveraging graph* etc.([Hol75, SLS97]).

Figure 3.4 shows the $(v_{\infty L} - v_{\infty H})$ leveraging graphs for the exterior (a) and interior (b) VILT (The domain of feasible $v_{\infty L}$ is discussed in the previous section). In these graphs, for simplicity and clarity, we plot only one VILT (the most efficient) for each $n : m$ case. We emphasize that the leveraging transfers and graphs are computed only once in nondimensional units, so that they can be applied to any endgame problem using the scale factors. Note that all of the numerical solutions presented in Figure

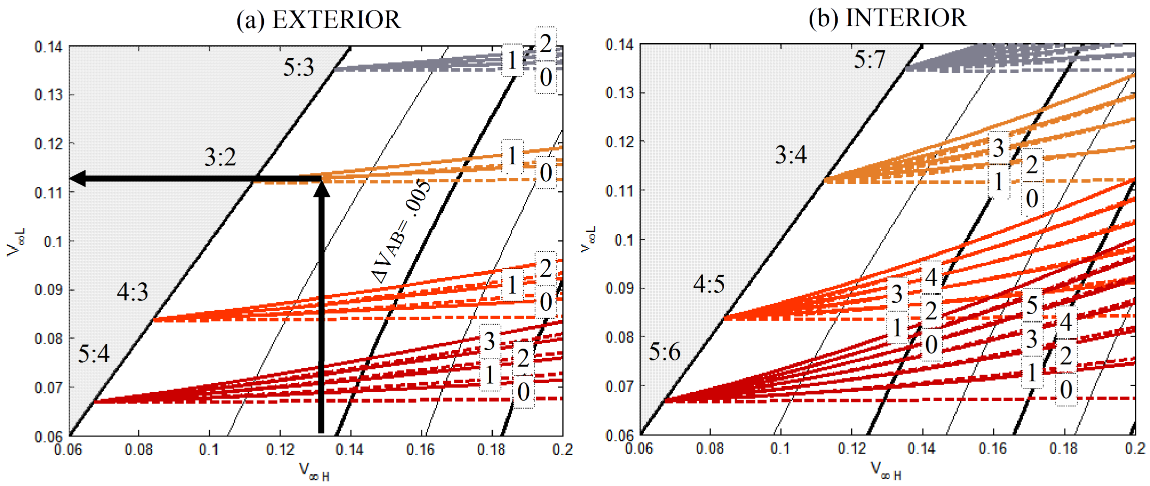

Figure 3.5: $(v_{\infty L} - v_{\infty H})$ leveraging graph for the exterior (a) and interior (b) VILT. In these close-ups,we plot $2m$ curves for each $n : m$ resonance. The dash curves are the short-transfer VILTs (one dash curve for each K , $0 < K < m - 1$). The solid curves are the long-transfer VILTs (one solid curve for each K, $0 < K < m-1$). The K parameter is indicated in the box. We also plot contour lines representing constant-Δv_{AB}.

5 are computed using a 200 line code written in Matlab. The computational time is approximately 1 minute using a dual-core 1.83 GHz laptop processor.

Figure 3.5 shows a close-up of the exterior (a) and interior (b) VILT. In contrast to Figure 3.4, all VILT solutions are plotted for each $n : m$ case. As an example , we show that the 3 : 2 exterior VILT reduces the v_∞ from $v_{\infty H} = 0.131$ to $v_{\infty L} = 0.1135$. By plotting the level sets of the phase free function $\Delta v_{AB}(v_{\infty L}, v_{\infty H})$ of Eq. (3.6) we estimate the $\Delta v_{AB} \approx 0.0022$. For a VILT at Europa, we multiply these values by the average velocity of Europa of approximately 13.7 km/s to find that we decrease $\tilde{v}_{\infty H} = 1.8$ km/s to $\tilde{v}_{\infty L} = 1.56$ km/s using approximately 30 m/s.

Finally we define the *phase-fixed efficiency* E of the VILT as the ratio between the variation of v_∞ and the Δv_{AB}

$$E = \frac{v_{\infty H} - v_{\infty L}}{\Delta v_{AB}}$$

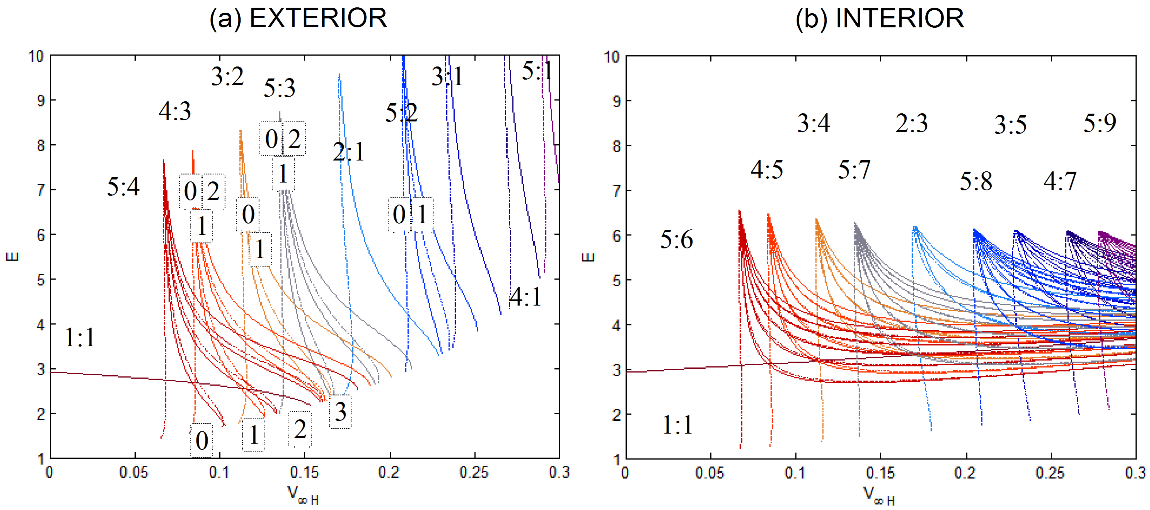

Figure 3.6: Efficiency of the exterior (a) and interior (b) VILT. The dash curves are the short-transfer VILTs, while the solid curves are the long-transfer VILTs. The numbers in the boxes represent the values of the parameter K. For any given resonance $n : m$, the most efficient VILT is $n : m^{+}_{m-1}$

Figure 3.6 shows the phase-fixed efficiency of the exterior (a) and interior (b) VILT. The figure shows that the most efficient VILTs are the one with the largest possible value of K ($K_{best} = m - 1$) and longest transfer time. However, we avoid discarding the less efficient solutions because the difference in efficiency can often be compensated when computing the VILT in more accurate models.

3.1.5 Minimum $v_{\infty L}$

In the previous example we showed that a Δv_{AB} of approximately 30 m/s reduces the relative velocity by approximately 240 m/s. However it is not always true that the Δv_{AB} is smaller than the actual gain/loss in relative velocity magnitude at the flyby body. In what follows we show that this occurs only if $v_{\infty L}$ is larger than a given value, which depends on v_c.

Let's assume an endgame problem where the spacecraft initially approaches the minor body with $v_{\infty H}$. The spacecraft needs $\Delta v_{\pi H} = v_{\pi H} - v_c$ to be captured in the target orbit. Alternatively, the spacecraft can perform a VILT which reduces the relative velocity to $v_{\infty L}$, and the new orbit insertion maneuver requires $\Delta v_{\pi L} = v_{\pi L} - v_c$. Then the VILT is efficient as long as the reduction of v_π is greater than the VILT cost Δv_{AB}.

Proposition The VILT strategy is efficient iff $v_{\infty L} > \overline{v}_\infty$ where $\overline{v}_\infty = \sqrt{\overline{v}_\pi^2 - 2v_c^2}$ and $\overline{v}_\pi\left(v_c\right)$ is the root of the function

$$f(v_\pi) = \Gamma \circ v_\infty\left(v_\pi; v_c\right) - v_\pi \tag{3.10}$$

where v_c is a parameter for f, and $\circ$ denotes function composition.

PROOF From Eq. (3.2) we find

$$v_{\infty H}^2 = v_{\pi H}^2 - 2v_c^2 \quad , \quad v_{\infty L}^2 = v_{\pi L}^2 - 2v_c^2 \tag{3.11}$$

We square Eq. (3.5) and use Eq. (3.11) to find

$$\left(v_{\pi H}\right)^2 = \left(v_{\pi L} + \Delta v_{AB}\right)^2 + 2\Delta v_{AB}\left(\Gamma - v_{\pi L}\right)$$

The VILT strategy is efficient if Δv_{AB} is less than the change in v_π, thus if

$$v_{\pi H} > \left(v_{\pi L} + \Delta v_{AB}\right) \longrightarrow \Gamma - v_{\pi L} > 0$$

To solve the problem we need to study the function $f(v_{\pi L}) = \Gamma \circ v_\infty\left(v_{\pi L}; v_c\right) - v_{\pi L}$, where v_c is a parameter.

For $v_{\pi L} = \sqrt{2}v_c$, we have $v_{\infty L} = \Gamma = 0$, thus $f(\sqrt{2}v_c) = -v_c$. Also $df/dv_\pi = d\Gamma/dv_{\infty L} * v_{\pi L}/v_{\infty L} - 1 > 0$ [2]. Then $f(v_\pi) > 0$ iff $V > \overline{v}_\pi$, where $\overline{v}_\pi\left(v_c\right)$ is the only root of $f\left(v_\pi\right) = 0$. Note that the root for the exterior VILT is different from the root of the interior VILT, as $\Gamma^{(E)} \neq \Gamma^{(I)}$.

To compute $\overline{v}_\pi$ we find numerically the root of the function in Eq. (3.10). Then we use Eq. (3.2) to find $\overline{v}_\infty$. $\overline{v}_\infty$ as function of the parameter v_C for

---

[2] An expression for $d\Gamma/dv_{\infty L}$ is given in appendix A

the exterior and interior case can be approximated by the following cubic splines:

$$\begin{aligned}
\overline{v}_{\infty}^{E} &= +\,(5.9561662273454e-5)\,v_c^3-(5.1344907043886e-2)\,v_c^2+\\
&\quad +\,(2.0441849005940e-1)\,v_c-(7.2712278793706e-6)\\
\overline{v}_{\infty}^{I} &= -\,(1.9176499488104e-2)\,v_c^3+(5.1814140491440e-2)\,v_c^2+\\
&\quad +\,(2.0377335047117e-1)\,v_c+(8.7463066767540e-6)
\end{aligned}$$

3.2 Leveraging graph and the Europa endgame

In this section we introduce the Tisserand leveraging graph which we use to design endgame strategies.

The Tisserand graph is a graph representing the pericenter r_p and period T of a Keplerian coplanar orbit around a major body [LPS98, SL02]. Certain points (r_p,T) on the graph represent orbits that intersect the orbits of minor bodies of the system. For these points we can compute the v_∞s with respect to the minor bodies that the given orbits intersect. We can then populate the Tisserand graphs with a set of $v_\infty-$level sets for each minor body. When a spacecraft performs a gravity assist at one minor body, it changes its location on the graph while staying on the $v_\infty-$level set. For this reason the Tisserand graph is a useful graph of the planetary / moon systems, and it has been used to design complicated multiple gravity assist trajectories [SS01, PLB00, VC09].

The Tisserand leveraging graph is an extension of the Tisserand graph which includes the numerical solutions of the VILT. Because we use nondimensional units we need only compute the graph once, and then scale it for the different minor bodies we want to include. To build the graph we begin by computing the Tisserand graph[LPS98, SL02] and representing it with the apocenter on the $x-$axis and the pericenter on the $y-$axis. This choice of the axes results in rectangular, semi-infinite sub domains of the minor bodies, and in period level sets which are straight diagonal lines with a slope of -1.

Starting with a (r_a, r_p) orbit, the new (r_a, r_p) following a VILT is aligned horizontally or vertically with the initial state. In particular:

- The Δv_{AB} of the interior VILT changes the apocenter but not the pericenter of the initial orbit. We represent the interior VILT with a horizontal shift from/to the line $r_a = 1$.
- The Δv_{AB} of the exterior VILT changes the pericenter but not the apocenter of the spacecraft orbit. We represent the exterior VILT with a vertical shift from/to the line $r_p = 1$.

In Figure 3.7 we show a schematic Tisserand graph. We use the apocenter-pericenter representation, and show the effect of an interior and exterior VILT. We also plot the period level sets and the v_∞ level sets, and the effect of a gravity assist. We clearly see how the Δv_{AB} changes the v_∞.

We proceed by including the numerical solutions of the VILT. We plot the curves in Figure 3.4 onto the Tisserand graph, and we obtain the *Tisserand leveraging graph.* Figure 3.8 shows the Tisserand leveraging graph in nondimensional units. We only include the VILTs with $K = m - 1$, as we showed in the previous section they are the most efficient. The solid thick lines are the long transfer VILTs, and the dotted thick lines are the short transfer VILTs.

3.2.1 Endgame at Europa using the Tisserand leveraging graph

In this section we use the Tisserand leveraging graph to design Europa endgames starting at $\tilde{v}_{\infty INITIAL} = 1.8$ km/s [3]. We assume the endgame consists of a series of forward-exterior VILTs. We first design one single endgame and then apply the same design strategy in a branch and bound search, storing the total time of flight (ToF) and the

---

[3] 1.8 km/s is slighty above the $\tilde{v}_\infty$which can be achieved by multiple gravity assists only [KCC04, VC09].

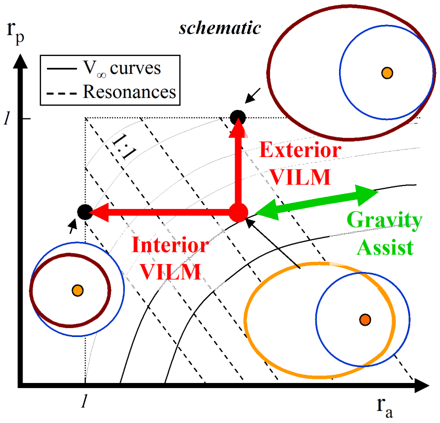

Figure 3.7: A schematic apocenter-pericenter Tisserand graph and the effect of an interior and exterior VILT. We also plot the period level sets and the v_∞ level sets. A gravity assist moves the spacecraft (r_a, r_p) along the v_∞level set. The VILT Δv_{AB} moves the spacecraft (r_a, r_p) horizonally or vertically, thus changing the v_∞.

total $\Delta\tilde{v}_{TOT} = \sum_i (\Delta\tilde{v}_{AB})_i + \Delta\tilde{v}_{\pi EOI}$, where $\Delta v_{\pi EOI}$ is the Europa orbit insertion maneuver

$$\Delta\tilde{v}_{\pi EOI} = \tilde{v}_\pi\left(\tilde{v}_{\infty FINAL}, \tilde{h}_\pi\right) - \tilde{v}_c$$

We start designing one Europa endgame, which is a sequence of forward interior VILTs. Figure 3.9 is a close-up of the Tisserand leveraging graph scaled to Europa by multiplying the distances by the semi-major axis of the Europa orbit, and by multiplying the velocities by the velocity of Europa. We also plot the level sets of the function $\Delta\tilde{v}_{AB}(\tilde{v}_{\infty L}, \tilde{v}_{\infty H})$ in Eq. (3.6). The starting point of the endgame is the point A on the figure. The first VILT is composed of a gravity assist and a $(\Delta\tilde{v}_{AB})_1$. During the gravity assist, the spacecraft moves along the $\tilde{v}_\infty = 1.8$ km/s level set until it intersects , e.g., the $3:2_1^+$ curve (point B). Then the $\Delta\tilde{v}_{AB}$ at apocenter raises the pericenter to a_M (point C). Using the $\Delta\tilde{v}_{AB}$ level sets we estimate $(\Delta\tilde{v}_{AB})_1 \approx 30$ m/s. The transfer time is approximately 3 Europa revolutions (around 10 days) and the new $\tilde{v}_\infty$ is around 1.6 km/s. The second VILT consists again of a gravity assist and an impulsive maneuver. The gravity assist moves the spacecraft (r_a, r_p) left and down on the graph

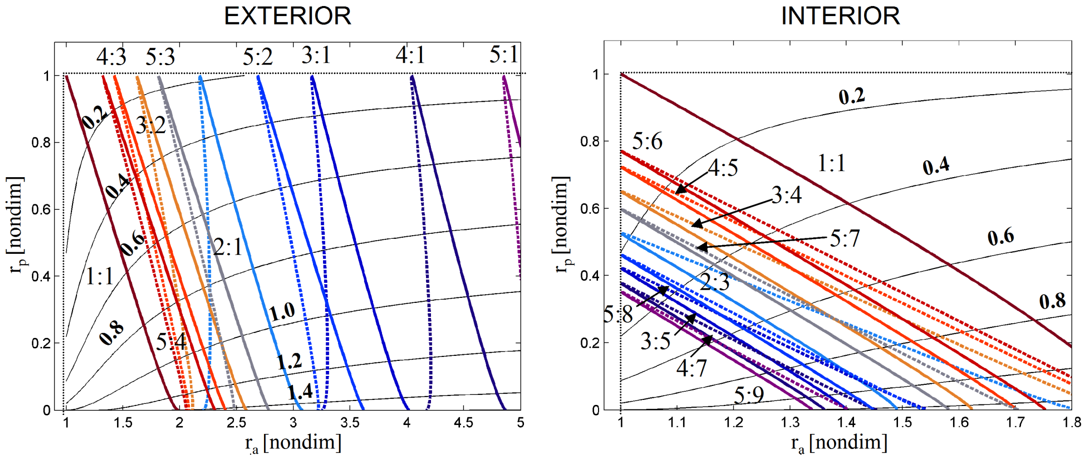

Figure 3.8: The *Tisserand leveraging graph* in nondimensional units obtained plotting the numerical solutions of the VILTs onto the Tisserand graph. We only include the VILTs with $K = m - 1$, as we showed in the previous section they are the most efficient. The solid thick lines are the long transfer VILTs, and the dotted thick lines are the short transfer VILTs. The contour lines are the v_∞ level sets.

until intersecting the $5:4_0^+$ curve (point D). The second VILT takes some 5 Europa revolutions, it costs some 60 m/s and it reduces the v_∞ to less than 1.2 km/s. We design the third VILT in the same way and end up with a total transfer time of $6 + 4 + 3 = 13$ Europa revolutions and a total cost of approx $60 + 60 + 30 = 150$ m/s, to which we can add the orbit insertion $\Delta\tilde{v}_\pi$ for $\tilde{v}_{\infty FINAL} = 0.8$ km/s and the desired $\tilde{h}_\pi$.

This design strategy is well-suited for a "branch and bound"[LD60], a global minimization algorithm composed of three steps. The first step (branching) split the solution space in subsets (nodes) which are linked in a tree structure. The second step (bounding) evaluates the upper and lower bounds of the merit function for a given node. The third step (pruning) discards the nodes with lower bound greater then a chosen pruning global variable (typically the minimum solution). Using a recursive function, the tree can be explored efficiently because suboptimal solutions are pruned early in the search. In our problem, starting from a fixed $\tilde{v}_{\infty INITIAL}$ the algorithm recursively applies forward-exterior VILTs and stores the ToF and total cost of the endgame, which are used to prune the branches. The result of the branch and bound search is shown in Figure

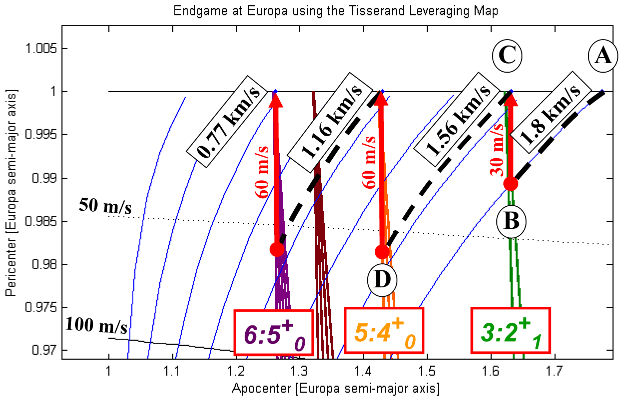

Figure 3.9: Simple endgame design using the Tisserand leveraging graph. Gravity assists move the spacecraft along the v_∞ level sets. The VILTs movethe spacecraft up to the $r_p = 1$ line.

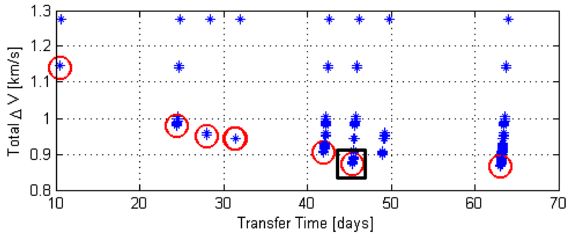

Figure 3.10: The result of the branch and bound search for the Europa endgame problem with initial velocity of 1.8km/s. The circles are the non-dominated solutions. Among those, the square is the test case presented previously.

3.10, where we plot some of the solutions (the stars) and the non-dominated solutions (circle). The test case explained previously is one of the non-dominated solutions (the square). The branch and bound solutions from Figure 3.10 on the right agree qualitatively with those from [BR09] that are found using an enumerative method based on dynamic programming principles.

3.3 Minimum and maximum Δv endgame using VILTs

In this section we use the phase-free formula introduced previously to discuss the efficiency of the endgame in terms of total Δv. We first prove that the cost of a sequence of VILTs decreases when favoring high altitude gravity assist. Then we use this result to compute the minimum and maximum cost of a multiple v_∞ -leveraging transfer, with a focus on the Europa endgame. Future works will include minimum time estimates. Finally we compute the minimum and maximum cost of a multiple v_∞- leveraging transfer between different moons, with focus on the Ganymede-Europa transfer.

3.3.1 Efficiency of the v_∞- leveraging

In this section we are interested in the efficiency of the VILTs in terms of Δv.

Theorem - The total Δv of a sequence of VILTs decreases if one low altitude gravity-assist VILT is replaced with two or more high altitude gravity-assist VILTs. That is, the total Δv of a sequence of VILTs decreases when favoring VILTs with high altitude gravity assists.

PROOF: We recall the definition of the phase-free efficiencies of Eq. (3.7) and Eq. (3.9)

$$\epsilon_{BI-FE} \equiv \frac{\Delta v_{AB} + \Gamma}{v_{\infty H}} \qquad \epsilon_{BE-FI} \equiv \frac{\Delta v_{AB} + \Gamma}{v_{\infty L} + \Delta v_{AB} \frac{d\Gamma}{dv_{\infty L}}}$$

We recall that $\Gamma > 0$. Thus for $\Delta v_{AB} \longrightarrow 0$, $\epsilon_{BI-FE} > 0$ and $\epsilon_{BE-FI} > 0$. Now compute the variation of the efficiency due to a variation of Δv_{AB}

$$\begin{aligned} \frac{\partial \epsilon_{BI-FE}}{\partial \Delta v_{AB}} (\Delta v_{AB}) &= \frac{v_{\infty H} - (\Delta v_{AB} + \Gamma)(D_2 v_{\infty H})}{v_{\infty H}^2} = \\ &= \frac{v_{\infty H}^2 - (\Delta v_{AB} + \Gamma)^2}{v_{\infty H}^3} = -\frac{\Gamma^2 - v_{\infty L}^2}{v_{\infty H}^2} < 0 \end{aligned}$$

$$\frac{\partial \epsilon_{BE-FI}}{\partial \Delta v_{AB}} (\Delta v_{AB}) = -\frac{\Gamma \frac{d\Gamma}{dV_{\infty L}} - v_{\infty L}}{\left(v_{\infty L} + \Delta v_{AB} \frac{d\Gamma}{dv_{\infty L}}\right)^2} < 0$$

where we used $\Gamma > v_{\pi L} > v_{\infty L}$ for the first equation , and $\Gamma \frac{d\Gamma}{dv_{\infty L}} > v_{\infty L}$ (proved in appendix A) for the second equation. Thus both ϵ_{BI-FE} and

> ϵ_{BE-FI} are positive at $\Delta v_{AB} = 0$ and strictly decreasing with Δv_{AB}: The efficiencies are at their maximum when $\Delta v_{AB} \longrightarrow 0$, i.e. for small impulsive maneuvers that - when multiple VILTs are patched together - requires high altitude gravity assist. Because this is true for any initial relative velocity, the cost of a sequence of VILTs decreases if we use more VILTs with low-Δv_{AB} as opposed to fewer VILTs with large Δv_{AB}. In practice, flight time consideration will limit the number of feasible VILTs.

The previous theorem is more intuitive when looking at the level sets of $v_{\infty H}\left(v_{\infty L}, \Delta v_{AB}\right)$ in Eq. (3.5), as explained in the following.

Figure 3.11 shows the curves $v_{\infty H}\left(v_{\infty L}, \Delta v_{AB}\right)$ for the Europa endgame case. At each gravity assist the spacecraft moves along a $v_{\infty H}$ level set. The VILT moves the spacecraft coordinates vertically from top to bottom.

The endgame discussed in the previous section and shown in Figure 3.11(a) is composed of three VILTs for a total transfer time of 46 days and a total Δv of 154 m/s to reduce the $\tilde{v}_{\infty}$ from 1.8 km/s to 0.77 km/s. Figure 3.11(b) shows a hypothetical endgame composed of fourteen VILTs, each using 10 m/s for a total of 140 m/s. The second strategy is cheaper in terms of Δv (it certainly has a much larger transfer time), because the slope of the curves $\Delta v(v_{\infty L})$ is larger for higher Δv. Note in fact that

$$\frac{\partial \Delta v_{AB}}{\partial v_{\infty L}} = -\left(\epsilon_{BE-FI}\right)^{-1} \tag{3.12}$$

Thus the cheapest way to move from an initial to a final v_{∞} is by zigzagging “low” on the $x - axis$. This suggests a simple strategy to compute the the minimum Δv of the VILT, which we explain in the next section. Conversely the more expensive way to move from an initial to a final v_{∞} is to perform one large VILT.

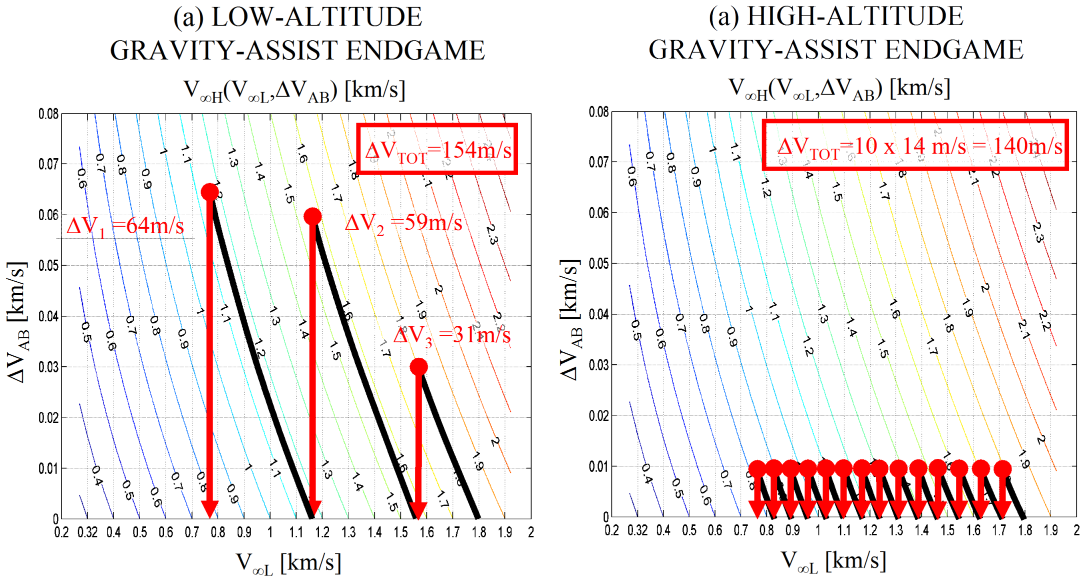

Figure 3.11: In this figure we compare the endgame at Europa computed in the previous section (a), with a hypothetical endgame composed of 14 VILTs (b). The countour lines are level sets of $v_{\infty H}$. The hypothetical endgame (b) is composed of several low-Δv_{AB}, high altitude gravity assist. The cost of the hypothetical endgame is lower because of the slope of the level sets, which is also related to the phase-free efficiency.

3.3.2 Theoretical minimum and maximum Δv for VILT with v_∞ boundary conditions

In this section we compute the minimum and maximum Δv cost to transfer from a $v_{\infty H}$ to $v_{\infty L}$ through a sequence of VILTs. We also compute the minimum and maximum cost for a transfer between two minor bodies $M1$ and $M2$ (with $\tilde{a}_{(M1)} < \tilde{a}_{(M2)}$) , where the boundary conditions are expressed as relative velocity at the first minor body $v_{\infty(M1)}$ and at the second minor body $v_{\infty(M2)}$ (we assume both velocities are larger than the respective $\overline{v}_\infty$).

In the previous section we showed that the minimum Δv is achieved for infinite transfer times , and infinite altitude gravity assists. We recall that the linked-conics model is less and less accurate for high altitude gravity assist, thus we do not exclude the existence of cheaper transfers computed in more accurate models. The interested reader is referred to [RL03, RS07, GR09, GMCM09]. In fact, in the next chapter we

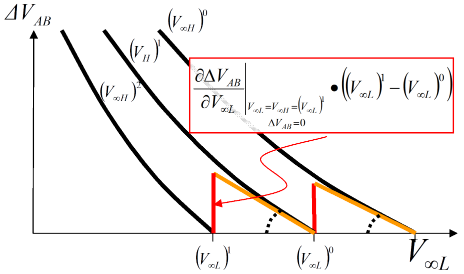

Figure 3.12: The slope of the $v_{\infty H}$ level sets at $\Delta v_{AB} = 0$ can be used to estimate the Δv_{AB} for a sequence of VILTs between infinitesimally close v_∞'s .

explain how the patched three-body problem allows for cheaper (even ballistic) transfers even when the VILT sequence requires a minimum Δv of several hundred meters per second. However, cheaper transfers are at the expense of larger times of flight - and larger radiation doses for missions to Europa; thus the VILT approach and fast transfers are still used by ESA and NASA to compute the nominal trajectories to Europa and Ganymede. In this context, the theoretical minimum Δv is a valuable piece of information during the design of resonant transfers as it sets the limit of the VILT approach. Further, as the non-dominated front in Figure 3.10 on the right shows, the variation in Δv across the full flight time spectrum is generally not more than 10% . The minimum Δv calculation is the main result of this chapter as it provides a simple, fast, and accurate estimate for a preliminary total Δv cost for any moon tour.

From the previously discussed theorem , and also looking at Figures 3.11 and 3.12, it follows that the minimum Δv needed to transfer from two different v_∞'s is the integral of the slope of the level sets $v_{\infty H}\left(v_{\infty L}, \Delta v_{AB}\right)$ at Δv= 0.

From Eq. (3.12) and Eq. (3.9) we find

$$\left.\frac{\partial \Delta v_{AB}}{\partial v_{\infty L}}\right|_{\substack{v_{\infty L} = v_\infty \\ \Delta v_{AB} = 0}} = -\frac{v_\infty}{\Gamma(v_\infty)}$$

where we recall that for $v_{\infty L} = v_{\infty H} = v_\infty$ when $\Delta v_{AB} = 0$. Then the minimum cost problem between $v_{\infty L}$ and $v_{\infty H}$ is reduced to simple quadrature

$$\Delta v_{min}^{(E,I)}\left(v_{\infty L}, v_{\infty H}\right) = \int_{v_{\infty L}}^{v_{\infty H}} \frac{v_\infty}{\Gamma^{(E,I)}(v_\infty)} dv_\infty \tag{3.13}$$

Using the definition of Γ in Eq. (9), we rewrite Eq. (3.13) as

$$\Delta v_{min}^{(E,I)}\left(v_{\infty L}, v_{\infty H}\right) = \int_{v_{\infty L}}^{v_{\infty H}} \frac{v_\infty^3 \pm 3v_\infty^2 + v_\infty \mp 1}{v_\infty^3 \pm 3v_\infty^2 - v_\infty \mp 7} dt \tag{3.14}$$

where the integral can be solved numerically with quadrature or with partial fractions. We recall that $0 \le v_\infty \le \sqrt{2} - 1$ for the exterior VILT, and $0 \le v_\infty \le 1$ for the interior VILT.

The maximum Δv is obtained by performing one unique VILT connecting $v_{\infty H}$ and $v_{\infty L}$, and the formula is given by Eq. (3.6):

$$\Delta v_{max}\left(v_{\infty L}, v_{\infty H}\right) = -\Gamma + \sqrt{\Gamma^2 + \left(v_{\infty H}^2 - v_{\infty L}^2\right)} \tag{3.15}$$

Note that $\Delta v_{max} = v_{\infty H}$ if $v_{\infty L} = 0$. Using Eq(3.14) and Eq.(3.15) we can compute the minimum and maximum Δv to increase or reduce the v_∞using a sequence of exterior or interior VILTs.

Now we compute the minimum Δv for transfers between two minor bodies $M1$ and $M2$ (with $\tilde{a}_{(M1)} < \tilde{a}_{(M2)}$). $\tilde{v}_{\infty(M2)}$ is the initial velocity relative to the outer minor body $M2$, while $\tilde{v}_{\infty(M1)}$ is the final velocity relative to the inner minor body $M1$. We define $\tilde{v}_{\infty(M1)}^{(h)}$ and $\tilde{v}_{\infty(M2)}^{(h)}$ as the (dimensional) relative velocities at $M1$ and $M2$ of the Hohmann transfer between the two minor bodies. We can use the scale factors associated with $M1$ and $M2$ respectively to compute:

$$v_{\infty(M1)}^{(h)} = \sqrt{\frac{2a_{M2}}{1 + a_{M2}}} - 1 \qquad v_{\infty(M2)}^{(h)} = 1 - \sqrt{\frac{2a_{M1}}{a_{M1} + 1}} \tag{3.16}$$

The Tisserand graph in Figure 3.13(a) shows that the transfer is free if the initial and final relative velocities ($\tilde{v}_{\infty(M2)}$ and $\tilde{v}_{\infty(M1)}$, respectively) are greater than the Hohmann transfer relative velocities ($\tilde{v}_{\infty(M1)}^{(h)}$ and $\tilde{v}_{\infty(M2)}^{(h)}$, respectively). Figure 3.13(a) also suggests that the logical strategy for the minimum Δv transfer consists of a sequence of

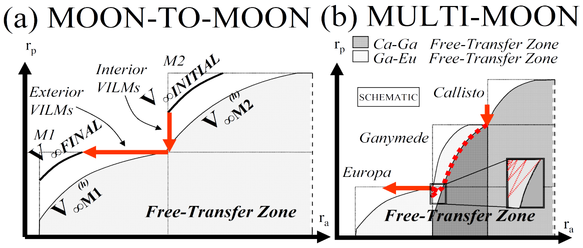
(a) MOON-TO-MOON (b) MULTI-MOON

Figure 3.13: Minimum VILT moon-to-moon transfer (a) and multi-moon transfer (b).

interior VILTs at $M2$, followed by the Hohmann transfer, and finally a sequence of exterior VILT at $M1$. Then Δv_{min} is computed by applying Eq. (3.14) twice, first from $v_{\infty H} = v_{\infty(M2)}$ to $v_{\infty L} = v^{(h)}_{\infty(M2)}$, and then from $v_{\infty H} = v^{(h)}_{\infty(M1)}$ to $v_{\infty L} = v_{\infty(M1)}$. The Δv_{max} is then computed using Eq. (3.15) instead of Eq. (3.14).

Figure 3.13(b) shows that other minor bodies can be used to decrease the total $\Delta\tilde{v}$. In the case of a transfer from Callisto to Europa using Ganymede, for example, we only need to increase the initial $\tilde{v}_{\infty(Ca)}$ until $\tilde{v}^{(h)}_{\infty(Ca)}$ to reach the free-transfer zone. Then gravity assists at Ganymede, Europa and Callisto can move the spacecraft to $\tilde{v}^{(h)}_{\infty(Eu)}$, where we start using VILTs at Europa until reaching the desired $\tilde{v}_{\infty(Eu)}$.

Using this notion, together with Eq. (3.14), Eq. (3.15), and Eq. (3.16), we can compute the minimum and maximum $\Delta\tilde{v}$ for any VILT. We apply these formulae for a transfer between Europa and Ganymede, and plot the results in Figure 3.14.

3.3.3 Theoretical minimum and maximum $\Delta\tilde{v}$ for transfers with h_π boundary conditions

In this section we compute the $\Delta\tilde{v}$ for a sequence of VILTs connecting a circular orbit at $M1$ with a circular orbit at $M2$. Pushing the VILT model to its limit, we start considering $r_\pi \to \infty$. In this case $v_c, \overline{v}_\infty, v_\pi, v_{\infty L} \to 0$ and the maximum Δv given by the formula Eq. (3.15), which also corresponds to the cost of a Hohmann transfer Δv when no VILT is implemented. In general, we consider the Hohmann transfer as the Δv_{max} to transfer from given circular orbits.

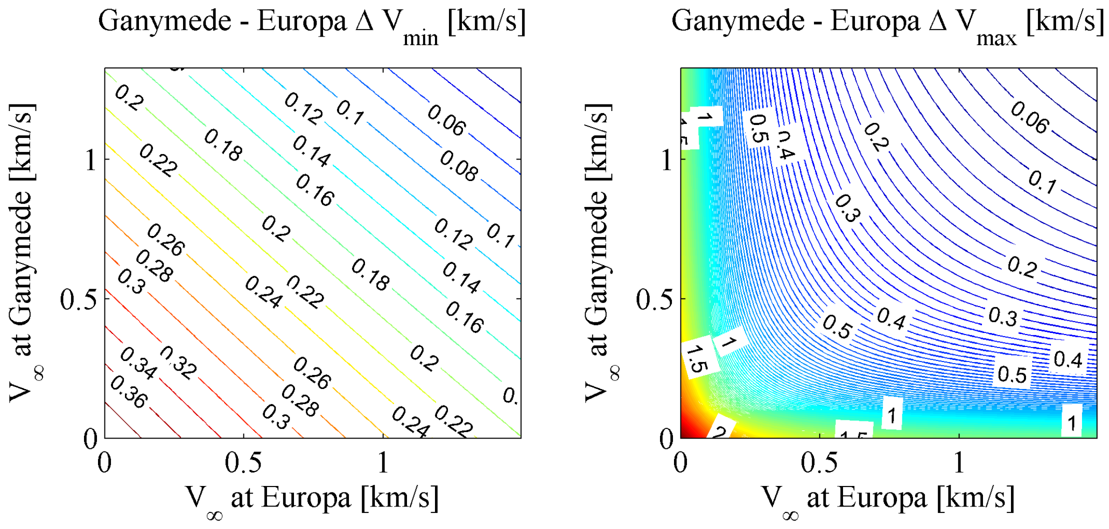

Figure 3.14: Minimum and Maximum cost for VILTs between Ganymede and Europa with v_∞ boundary conditions. The contour lines are the total Δv level sets in km/s.

The minimum cost is computed using Eq. (3.14). In particular, the cost to reach the $\tilde{v}^{(h)}_{\infty(M1)}$ and $\tilde{v}^{(h)}_{\infty(M2)}$ in the $M1$ and $M2$ nondimensional units are

$$\Delta v_{(Mi)}\left(v_{c(Mi)}\right) = \overline{v}_{\pi(Mi)}\left(v_{c(Mi)}\right) - v_{c(Mi)} + \int_{\overline{v}_{\infty(Mi)}\left(v_{c(Mi)}\right)}^{v^{(h)}_{\infty(Mi)}} \frac{v_\infty}{\Gamma}\, dv_\infty \quad i = 1, 2 \tag{3.17}$$

The first two terms on the right-hand side of Eq. (3.17) represent a propulsive maneuver at pericenter of the escape or insertion hyperbola. This maneuver is the escape or capture orbit insertion maneuver($\Delta v_{escape}, \Delta v_{capture}$) required to reach the $\overline{v}_\infty$ (the minimum v_∞ where it becomes efficient to start using VILT). The integral term represents the minimum endgame or begin-game ($\Delta v_{endgame}, \Delta v_{begingame}$) to reach the Hohmann transfer conditions. Note that the total cost is a function of v_c, i.e. of the altitudes h_π.

The total minimum cost in dimensional units is:

$$\Delta\tilde{v} = \Delta v_{(M1)}\tilde{v}_{M1} + \Delta v_{(M2)}\tilde{v}_{M2}$$

Table 3.1 and 3.2 show the minimum and maximum $\Delta\tilde{v}$ [km/s] for transfers between moons in the Jupiter System and in the Saturn System. The minimum $\Delta\tilde{v}$ is the cost of the escape, begin-game, endgame, and capture. All the initial and final circular orbits are at 100 km altitude, except for the orbits at Titan, which are at 1500 km altitude.

Table 3.2 shows the same results for transfers with intermoon gravity assists. In this case the cost of the transfer is significantly reduced because the spacecraft only need to reach the closest moons where it can start performing several gravity assists at different moons, as explained previously and suggested in Figure 3.13(b).

Table 3.3 shows the semi-major axis and physical data[4] used in the computation of the minimum $\Delta\tilde{v}$. We also show the radius of the circular orbits, and the corresponding $\tilde{\tilde{v}}_\infty$ in case of exterior and interior VILTs. The velocity of the moon $\tilde{v}_M$ is the scale factor for all the velocities.

---

[4] http://ssd.jpl.nasa.gov/

Table 3.1: Minimum and maximum $\Delta\tilde{v}$ for transfers between moons using VILTs. The transfers start and end at two circular orbits with high or low altitude. The minimum $\Delta\tilde{v}$ is computed assuming infinite transfer time, and consists of a $\Delta\tilde{v}_{escape}$,$\Delta\tilde{v}_{begingame}$,$\Delta\tilde{v}_{endgame}$,$\Delta\tilde{v}_{capture}$. The maximum $\Delta\tilde{v}$ is the cost of the Hohmann transfer without VILTs. In the estimated transfer time NaN indicates a flight time $>$ 25 years. Note that using multi-body dynamics it can be possible to find long transfers which require lower $\Delta\tilde{v}$s than the one in this table. Also, in transfers involving low-mass flyby bodies or large separation distances, shorter flight time solutions are possible if considering the non-tangent class of VILTs.

Transfer	Δv_{min}	Δv_{max}	Δv_{min} (km/s) - *details*			
	(km/s)	(km/s)	Δv_{esc}	Δv_{beg}	Δv_{end}	Δv_{cap}
Callisto-Ganymede	1.81	2.13	0.73	0.13	0.13	0.81
Callisto-Europa	1.94	3.75	0.73	0.3	0.31	0.59
Callisto-Io	2.43	6.00	0.73	0.46	0.48	0.75
Ganymede-Europa	1.71	2.18	0.82	0.14	0.16	0.59
Ganymede-Io	2.3	4.38	0.82	0.36	0.37	0.75
Europa-Io	1.76	2.54	0.6	0.21	0.2	0.75
Titan-Rhea	1.15	2.19	0.64	0.15	0.18	0.18
Titan-Dione	1.28	3.33	0.64	0.23	0.27	0.14
Titan-Tethys	1.37	4.31	0.64	0.29	0.33	0.11
Titan-Enceladus	1.43	5.27	0.64	0.33	0.4	0.06
Rhea-Dione	0.52	1.12	0.18	0.10	0.10	0.14
Rhea-Tethys	0.66	2.3	0.18	0.19	0.19	0.11
Rhea-Enceladus	0.78	3.53	0.18	0.27	0.27	0.06
Dione-Tethys	0.42	0.97	0.14	0.08	0.09	0.11
Dione-Enceladus	0.55	2.19	0.14	0.17	0.18	0.06
Tethys-Enceladus	0.34	1.00	0.11	0.08	0.09	0.06

Table 3.2: Minimum $\Delta\tilde{v}$ for transfers between moons using VILTs and gravity assists. The minimum $\Delta\tilde{v}$ is computed assuming infinite transfer time. The maximum $\Delta\tilde{v}$ is the cost of the Hohmann transfers to the closest inner/outer moons. Using multi-body dynamics it might be possible to find long transfers which require lower $\Delta\tilde{v}$s than the one in this table.

Transfer	Δv_{min}	Δv_{max}	Δv_{min} (km/s) - *details*			
	(km/s)	(km/s)	Δv_{esc}	Δv_{beg}	Δv_{end}	Δv_{cap}
Callisto-G-Europa	1.61	2.07	0.73	0.13	0.16	0.59
Callisto-G-E-Io	1.81	2.35	0.73	0.13	0.2	0.75
Ganymede-E-Io	1.91	2.45	0.82	0.14	0.2	0.75
Titan-R-Dione	1.03	1.55	0.64	0.15	0.099	0.14
Titan-R-D-Tethys	0.98	1.47	0.64	0.15	0.086	0.11
Titan-R-D-T-Enceladus	0.93	1.5	0.64	0.15	0.086	0.061
Rhea-D-Tethys	0.47	1.04	0.18	0.097	0.086	0.11
Rhea-D-T-Enceladus	0.43	1.07	0.18	0.097	0.086	0.061
Dione-T-Enceladus	0.37	1	0.14	0.084	0.086	0.061

Table 3.3: Moon data used for the computation of the Δvs and transfer times.

Moon	$\tilde{\mu}_M\left(km^3/s^2\right)$	$\tilde{a}_M(km)$	$\tilde{v}_M(km/s)$	$\tilde{r}_\pi(km)$	$\tilde{\tilde{v}}_\infty(\tilde{r}_\pi)$ E/I (km/s)
Io	5960	421800	17.330	1922	0.351 / 0.368
Europa	3203	671100	13.739	1661	0.277 / 0.290
Ganymede	9888	1070400	10.879	2731	0.372 / 0.404
Callisto	7179	1882700	8.203	2510	0.328 / 0.361
Enceladus	7	238040	12.624	352	0.029 / 0.029
Tethys	41	294670	11.346	633	0.052 / 0.052
Dione	73	377420	10.025	662	0.067 / 0.068
Rhea	154	527070	8.484	864	0.085 / 0.087
Titan	8978	1221870	5.572	4076	0.283 / 0.321

Chapter 4

The endgame problem using the multi-body technique and the T-P graph

In this chapter we continue studying the endgame problem, focusing on the multi-body technique.

In the first section we show how to transform the linked-conic gravity assist parameter in a state vector to be used in the CR3BP. We then consider two VILT endgames at Europa which were presented in Part A and use them as first guesses for the design of endgames in the CR3BP. The results show that although some VILT solutions cost almost the same, their total Δv might differ by as much as 10% when computed in a more accurate model. In general, the VILT approach should be used for fast preliminary design only if lower-cost longer-transfer solutions are *not* an option. Quasi-ballistic endgames and transfers cannot be designed either using the VILT approach or starting from VILT solutions, hence the need for a more accurate model and design strategy.

In the second section we introduce a Poincaré section in the negative x-axis of the rotating reference frame of the CR3BP. Far from the minor body the spacecraft trajectory is very similar to a Keplerian orbit; thus we can compute the osculating orbital elements of the spacecraft as it crosses the section, and plot them in a pericenter vs apocenter graph. On the same graph we plot Tisserand parameter level sets: the Tisserand parameter T is an approximation of the Jacobi constant, and it is very accurate when far from the minor body and for small mass parameters. The result is the Tisserand-Poincaré

(T-P) graph, which is a natural extension of the Tisserand graph, as the v_∞ level sets are synonymous to Tisserand level sets noting that $T = 3 - v_\infty^2$ (see appendix B). Yet the Tisserand level sets extend beyond the v_∞curves well into the regions where v_∞ is not feasible in the linked-conic models ($v_\infty^2 < 0$ if $T > 3$). Therefore when considering the conservation of the Tisserand parameter, the T-P graph demonstrates that ballistic transfers between moons are energetically possible despite the contrary conclusion derived from linked-conics theory. This is the first important result of the T-P graph.

In the third section we analyze the T-P graph in more detail. We use it to explain the multi-moon orbiter[RL03] and to explain in general the anatomy of multi-body techniques. We focus on ballistic endgames and question the need for multiple flybys and resonant orbits, noting that ballistic transfers do not change the Jacobi constant and hence do not change the arrival speed at the minor body (the *ballistic endgame paradox*). Then we use the T-P graph to solve the paradox, showing that at low energy levels, high altitude flybys of the minor body are the only ballistic mechanism to move along the Tisserand curves and to reach the target altitude at the minor body.

In the last section we design transfers between Europa and Ganymede. Using the considerations from the previous section, we find trajectories that move through the graph in the shortest time and reach a prespecified target point on the T-P graph, which is the intersection of the Tisserand level sets of the endgame at Europa and begin-game at Ganymede. In particular we compute a transfer from a circular orbit at Ganymede to a circular orbit at Europa for comparison with the VILTs solutions. We also compute a transfer between a halo orbit at Ganymede and a halo orbit at Callisto; in both cases the T-P graph provides an estimate of Δv. We argue that, while the total cost might increase in the full ephemeris model due to the fourth-body perturbations, non-circular orbits, and change-of-plane maneuvers. We also argue however that a robust optimization algorithm should reduce the conservatively estimated costs with the introduction of several small mid-course maneuvers. Finally we recall that in the Jupiter system long time-of-flight trajectories are prohibited the radiation exposure.

Nomenclature

a, e, i	Semi-major axis, eccentricity, inclination with respect to the major body.
J	Jacobi constant.
M	Subscript indicates the quantity is referred to the minor body.
P	Subscript indicates the quantity is referred to the major body.
r_a, r_p	Pericenter, apocenter with respect to the major body.
r_π, v_π	Position and velocity of the spacecraft with respect to the minor body at the closest approach.
T	Tisserand Parameter.
v_∞	Relative velocity of the spacecraft at the minor body.
X, x	Upper case for variables in the rotating frame, lower case for variables in the inertial frame.
μ	Gravitational constant.
$\tilde{x}$	Tilde indicates dimensional variables.

4.1 Endgames from linked-2BP to CR3BP

The conventional method for designing endgame trajectories is by patching v_∞-leveraging maneuvers (VILTs) in the linked-conic model [BdPC, JD99, CR10a].Yet near ballistic endgames have been designed only in more accurate models, like the restricted 5-body problem[RL03] or the full ephemeris model[SPC99]. In this work, we use the circular restricted three-body problem (CR3BP) model to design ballistic endgames, and patched CR3BP models to design transfers between moons.

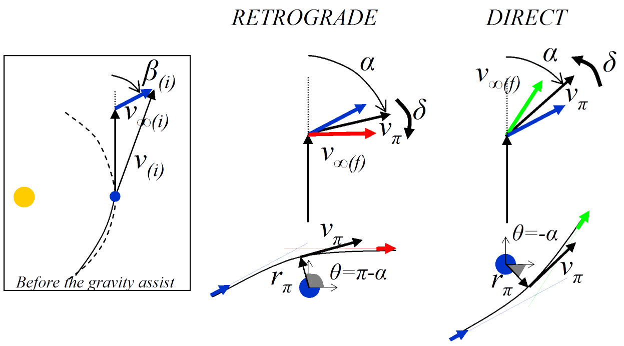

Figure 4.1: Direct and retrograde gravity assists.

In this section we show how to reproduce a linked-conics gravity assist in the planar CR3BP. We then consider two very similar Europa endgames in the linked-conics model (designed using the leveraging graphs, from the previous chapter) and optimize them in the CR3BP model. The results give insight into the difference between the two models, and into the limitations of the lower fidelity VILT approach when designing long flight time, low-cost endgame trajectories.

In this chapter, variables without the tilde have been normalized using the usual space, time, and mass scale factors

$$l^* = \tilde{a}_M, \qquad t^* = \sqrt{\frac{\tilde{a}_M^3}{\tilde{\mu}_P + \tilde{\mu}_M}} \qquad m^* = \tilde{m}_M + \tilde{m}_P$$

4.1.1 Flyby

In this section we reproduce a linked-conic gravity assist in the CR3BP. In particular we use the parameters of the linked-conic gravity assist to generate the vector state of the spacecraft at r_π, the closet approach to the minor body. We focus on the planar case, because we will use the results to reproduce VILTs in the CR3BP. Figure 4.1 shows the schematic of the direct and retrograde gravity assists.

From the velocity $v_{(i)}$ and flight-path angle γ of the spacecraft just before the encounter we find

$$v_\infty = \sqrt{1 + v_{(i)}^2 - 2v_{(i)} \cos\gamma} \quad , \quad \beta_{(i)} = \arcsin \frac{v_{(i)} \cos\gamma}{v_\infty} \tag{4.1}$$

The gravity assist parameters r_π and σ ($\sigma = 1$ for direct gravity assists and $\sigma = -1$ for retrograde gravity assists) provide the deviation angle with Eq. (3.1), but also the norm and direction of the velocity at pericenter v_π, as shown in Figure 4.1 and in the following equations

$$v_\pi = \sqrt{v_\infty^2 + 2\mu/r_\pi} \quad , \quad \alpha = \beta_{(i)} - \sigma\delta/2 \tag{4.2}$$

Now we can write the state $s = (x, y, \dot{x}, \dot{y})$ of the spacecraft at the closest approach in the inertial reference frame centered in the minor body. Always referring to figure 4.1, we find

$$\theta = -\alpha + (1-\sigma)\,\pi/2 \quad , \quad s = (r_\pi \cos\theta, r_\pi \sin\theta, -\sigma v_\pi \sin\theta, \sigma v_\pi \cos\theta) \tag{4.3}$$

Finally we apply the transformation of coordinate (see appendix B) to find the state vector in the rotating reference frame

$$S = ((1-\mu) + r_\pi \cos\theta, r_\pi \sin\theta, -(\sigma v_\pi - r_\pi)\sin\theta, (\sigma v_\pi - r_\pi)\cos\theta) \tag{4.4}$$

We now consider the special case $\beta_{(i)} = 0$ (the case when the v_∞ vector is aligned with the body velocity vector), which we use in the next section. From Eq. (4.2) and Eq. (4.3) we find

$$\theta = -\frac{\pi}{2} + \sigma\left(\frac{\pi}{2} + \delta\right) \tag{4.5}$$

4.1.2 Endgame optimization in the CR3BP

In this section we compute two endgames in the CR3BP. We take two VILT endgames at Europa rom the previous chapter, reproduce them in the CR3BP and use them as first guesses for an optimization algorithm which minimize the total Δv.

The first endgame is a sequence of long-transfer VILTs: $3:2_1^+, 4:3_0^+, 5:6_0^+$, where the plus sign refers to a long-transfer VILT. The second endgame is a sequence of short-transfer VILTs: $3:2_1^-, 4:3_0^-, 5:6_0^-$, where the minus sign in refers to a short-transfer VILT. Both endgames require some 150m/s to decrease the v_∞ from 1.8 km/s to approx. 0.8 km/s, and both endgames are composed by VILTs in which $\beta_{(i)} = 0$. However the long-transfer VILTs are linked by direct gravity assists ($\sigma = 1$) while the short transfer VILTs are linked by retrograde gravity assists ($\sigma = -1$).

As a consequence, Eq. (4.5) shows that the closest approaches of the first endgame occur on the L2 side ($-\pi/2 < \theta < \pi/2$), while the closest approaches of the second endgame occur on the L1 side ($\pi/2 < \theta < 3\pi/2$). Although the two endgames have similar costs, sequence of resonances and transfer time, they are significantly different in the region around the minor body, and they belong to two different basins of attraction for the optimization problem in the CR3BP. This subtlety justifies the choice of optimizing both of them.

The trajectory optimization problem in the CR3BP is formulated as a nonlinear parameter optimization problem, where the dynamics constraints (equations of motion) are solved implicitly. The control variables are the times, altitudes $r_\pi - \tilde{r}_M$, speeds V_π and angles θ of all the closest approaches and the times of the mid-course maneuvers.

The optimizer first propagates the states of every close approach backward and forward in time until the mid-course maneuvers time. The position of the last point of the forward propagation is then constrained to match the position of the last point of the backward propagation from the next closest approach[1]. The corresponding velocities are free but their difference, in norm, is added to the merit function.

---

[1] Because the problem is formulated in the rotating reference frame, the approach is robust despite the several revolutions (in the inertial frame) which occur between the flybys and the mid-course maneuvers.

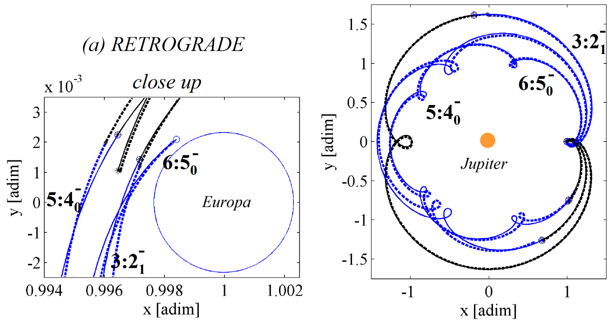
(a) RETROGRADE

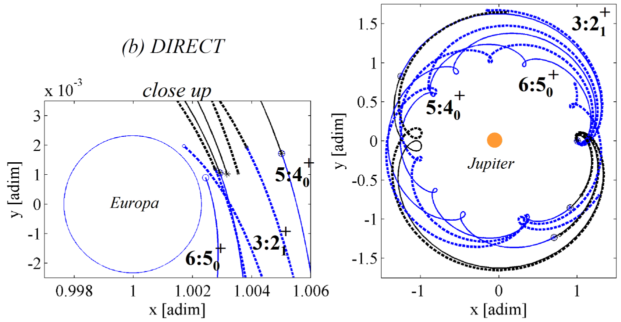
(b) DIRECT

Figure 4.2: Long-transfer (direct) and short-transfer (retrograde) endgames at Europa optimized in the CR3BP (solid lines). Initially the VILT solutions are used to find the times of the midcourse and the states and times of the spacecraft at the close approaches. Those states are then propagated backward and forward in time in the CR3BP generating the first guess solutions (dash lines) for the optimization problem.

As we are ultimately interested to compare the VILT solutions to the CR3BP endgame, we add constraints to fix the boundary conditions. In particular, we constrain the first closest approach to keep the first guess $\beta_{(i)}$ and v_∞, and we constrain the last closest approach to a given altitude and v_∞.

The first guess is generated using the VILT approach. The VILT solutions provide the times of the mid-course maneuvers and the flyby times, altitudes, and v_∞. Eq. (4.2), Eq. (4.5) , and Eq. (4.4) are used to compute the angles θ and the velocities V_π. Finally the parameter optimization problem is fed into the Matlab solver *fmincon*, which implements a sequential quadratic programming (SQP) method. For both endgames, Figure 4.2 shows the initial guesses (dash lines) and the optimized solutions (solid lines). The total cost of the optimized long-transfer endgame is 147 m/s (the VILT solution costs 154 m/s) with a time of flight of 47.0 days, while the cost of the optimized short-transfer endgame is 165 m/s (the VILT solution costs 155 m/s) with a time of flight of 45.4 days.

4.1.3 Limitations of the VILT approach

The VILT approach is very fast and intuitive, and we envision using it for preliminary design of endgame and begin-game trajectories whenever long- transfer time low-cost solutions are not an option. However the previous section showed that the VILT approach has some important limitations that deserve attention.

First, the cost of the VILT endgames can be off up to ±5% when compared to the more accurate CR3BP solutions[2]. We expect this error to increase as more resonances and high-altitude gravity assists are added.

Second, while the VILT approach estimates approximately the same Δv for the short-transfer solution and the long-transfer solution, the CR3BP shows that one kind of transfer is preferable (the long-transfer in the case shown in the previous section).

Finally, and most importantly , quasi-ballistic endgames cannot be found by simply designing a VILT endgame and optimizing it in the CR3BP. The linked-conic approach cannot explain the existence of ballistic endgames - not even in the limit of infinite transfer time where a minimum $\Delta v \neq 0$ can be computed (ee prevous chapter). In addition, the last chapter showed that the VILT solutions do not converge to quasi-ballistic endgames in the CR3BP. In fact the multi-resonant transfers are chaotic in nature where the design space is plagued by multiple local minima[RS07] that can easily trap gradient based optimizers. Clearly local minima exist in the CR3BP when using the VILT as an initial guess, but it's unrealistic for the optimizer to climb out of that basin en route to quasi ballistic solutions. Instead we should seek solutions that start in the correct basin!

---

[2] These values are consistent with the ±10% difference observed during the design of the Cassini tour when comparing Δv costs in the linked conics model with more accurate models (personal communication from Nathan Strange).

For the above reasons we seek to further our understanding of the dynamics of near ballistic endgame transfers. Ultimately, we seek systematic methods and tools to design such transfers. While the patched CR3BP is the first step towards solutions in a fully perturbed n-body model, the CR3BP indeed captures the dominant dynamics. Further, the system is Hamiltonian, allows for rapid computations, and preserves the Jacobi constant (or equivalently, in the case of this study, the Tisserand Parameter).

4.2 The Tisserand parameter and the T-P graph

In this section we introduce the T-P graph (named after Tisserand and Poincaré). The graph is a fundamental tool that provides dynamical justification for the multi-body technique and can be used to design quasi-ballistic transfers between moons. The T-P graph is built plotting Poincaré sections of different CR3BP models in one unique r_a, r_p graph. In the same graph the level sets of the respective Tisserand parameters are also plotted. The result is the T-P graph, which can be interpreted as an extension of the Tisserand graph [LPS98, SL02] from the linked-conic model to the patched CR3BP model.

4.2.1 Poincaré section

The first step in building the T-P graph is the introduction of a Poincaré section in the negative x-axis of the rotating reference frame of each CR3BP. When the spacecraft crosses the Poincaré section, far from the minor body, its trajectory is very well approximated by a Keplerian orbit around the major body. From the state vector at the crossing point we compute the osculating pericenter and apocenter relative to the main body, which we plot in a $r_a - r_p$ graph, similar to the one described in the previous chapter. Figure 4.3 shows a schematic of the Poincaré section and the corresponding $r_a - r_p$ graph.

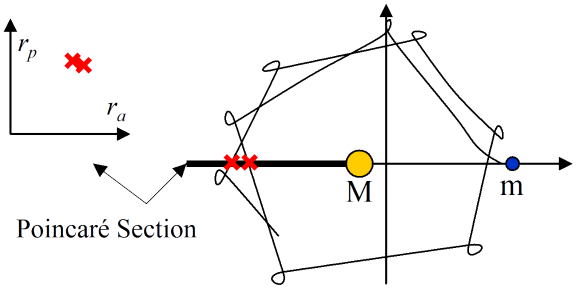

Figure 4.3: The Poincaré section for the definition of the T-P graph (schematic).

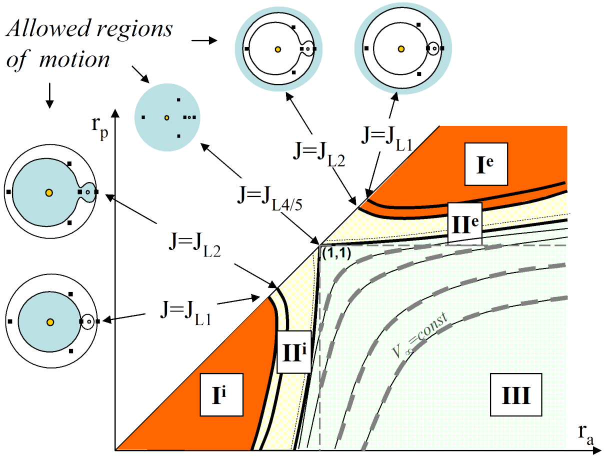

Figure 4.4: Tisserand parameter level sets on the T-P graph and corresponding regions of motion in the CR3BP (schematic).

4.2.2 The Tisserand parameter

On the same graph we plot the level sets of constant Tisserand parameter . The Tisserand parameter T is a function of the semi-major axis a (in normalized units: $a = \tilde{a}/\tilde{a}_M$), inclination i and eccentricity e of a spacecraft orbiting a major body[Tis96]

$$T\left(a,e,i\right) = \frac{1}{a} + 2\sqrt{a\left(1-e^2\right)}\cos i \tag{4.6}$$

In this work we consider the planar problem and rewrite Eq. (4.6) as a function of the pericenter and apocenter only

$$T\left(r_a,r_p\right) = \frac{2}{r_a+r_p} + 2\sqrt{\frac{2r_ar_p}{r_a+r_p}} \tag{4.7}$$

The Tisserand parameter remains approximately constant even after a close encounter with a minor body. This is known as the *Tisserand criterion* [Tis96]. It is well-known in fact that the Tisserand parameter is an approximation of the Jacobi constant J of the CR3BP, .i.e $T \approx J$.

The approximation is increasingly accurate for smaller mass parameters μ and when the spacecraft is far from the minor body (e.g. when it crosses the Poincaré section defined previously). In appendix B we show how to derive the Tisserand parameter from the Jacobi constant; similar derivations are found in literature [Tis96, MW].

4.2.3 The T-P graph

Now we are ready to plot the level sets of the Tisserand parameter onto the $r_a - r_p$ graph. We start plotting the four level sets $T = J_{Li}$, $i = 1, \ldots, 4$, where J_{Li} is the value of the Jacobi constant associated to the i^{th} Lagrangian points (note that $J_{L4} = J_{L5} = 3$). The level sets divide the $r_a - r_p$ graph into regions of motion, as shown in Figure 4.4.

As the spacecraft crosses the Poincaré section, the osculating orbital elements are represented with a point on the T-P graph. If the point is in the region I^i, the spacecraft position is bounded in a region close to the major body and no transfer to the minor body is possible. Similarly, if the spacecraft is in the region I^e, the spacecraft is bounded in a region far from the major body and no transfer to the minor body is possible.

Transfers to the minor body are possible only when the spacecraft is in the regions II^i, II^e, III. In particular, we expect low-energy transfer and capture trajectories to occur in the region II^i (if coming from the inner moons) or II^e(if coming from the outer moons).

Note that inside the box $r_p < 1$, $r_a > 1$ (within region III) we can also plot the constant v_∞ level sets, as done in the Tisserand graph [SL02]. The v_∞-infinity level sets overlap with the constant Tisserand level sets[3]. In fact it can be proved that (see appendix B)

---

[3] Then we can think of the Tisserand level sets as J level set or C3=v_∞^2 level sets

$$T = 3 - v_\infty^2 \approx J$$

In the $r_a - r_p$ graph we can plot curves at constant resonance $n : m$ (where n is the number of body revolutions and m is the number of spacecraft revolutions), which are lines with slope -1

$$a = \left(\frac{n}{m}\right)^{2/3} \rightarrow r_p = -r_a + 2\left(\frac{n}{m}\right)^{2/3}$$

In order to study transfers between minor bodies, we plot on the same graph several Tisserand level sets, each in the dimensioned coordinates of the corresponding minor body. The Tisserand parameter with respect to the minor body M is

$$T_M = \frac{2\tilde{a}_M}{\tilde{r}_a + \tilde{r}_p} + 2\sqrt{\frac{2\tilde{r}_a\tilde{r}_p}{\left(\tilde{r}_a + \tilde{r}_p\right)\tilde{a}_M}} \tag{4.8}$$

Finally we include a grid which shows the Δv required to change the pericenter/apocenter using an impulsive maneuver.

The result is the T-P graph , which we show in Figure 4.5(b). In Figure 4.5(a) we plot the $r_a - r_p$ Tisserand graph . We see how the extension from a linked-conics model (for the Tisserand graph) to patched CR3BP model (T-P graph) results in level sets which extend over the feasible domain of the Tisserand graph. As a consequence, even low-energy (low v_∞) level sets reach very high apocenters.

Figure 4.6 shows the T-P graph for the Saturn system. We can see that the low-energy level sets (region II^e and II^i) of any two moons cross, in contrast to the linked conics model where ballistic intermoon transfers are only possible for v_∞ greater than that of the corresponding Hohmann transfer. From an *energetic* point of view, then, a ballistic transfer between any two moons in the patched CR3BP is always possible. This does not guarantee that such transfers can be found, especially within a practical transfer time. Some recent works demonstrate that such transfers can exist[RJJ09].

(a)
Tisserand Graph

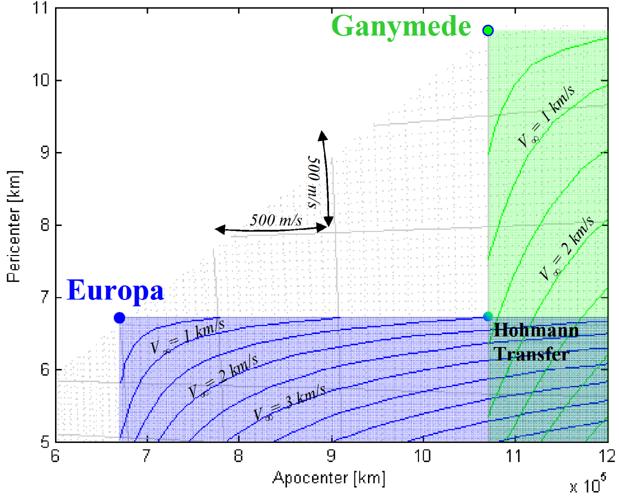

(b)
T-P Graph

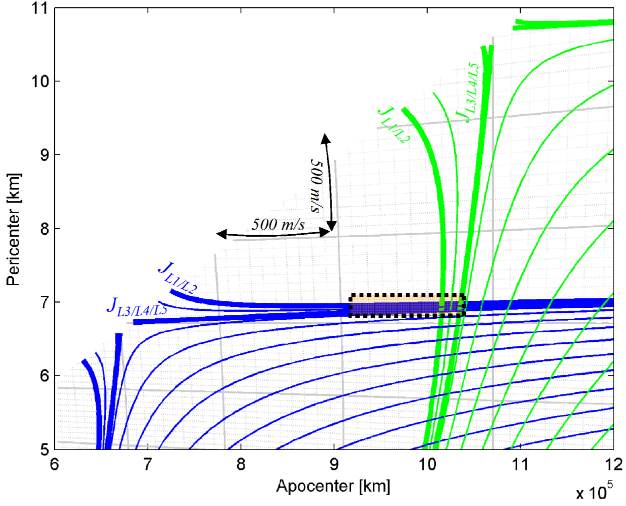

Figure 4.5: Tisserand Graph (a) and T-P graph (b).

The intersection point between the Tisserand level sets of two different moons is the solution of the system:

$$\begin{cases} T_{M1} &= \frac{2\tilde{a}_{M1}}{\tilde{r}_a+\tilde{r}_p} + 2\sqrt{\frac{2\tilde{r}_a\tilde{r}_p}{(\tilde{r}_a+\tilde{r}_p)\tilde{a}_{M1}}} \\ T_{M2} &= \frac{2\tilde{a}_{M2}}{\tilde{r}_a+\tilde{r}_p} + 2\sqrt{\frac{2\tilde{r}_a\tilde{r}_p}{(\tilde{r}_a+\tilde{r}_p)\tilde{a}_{M2}}} \end{cases} \tag{4.9}$$

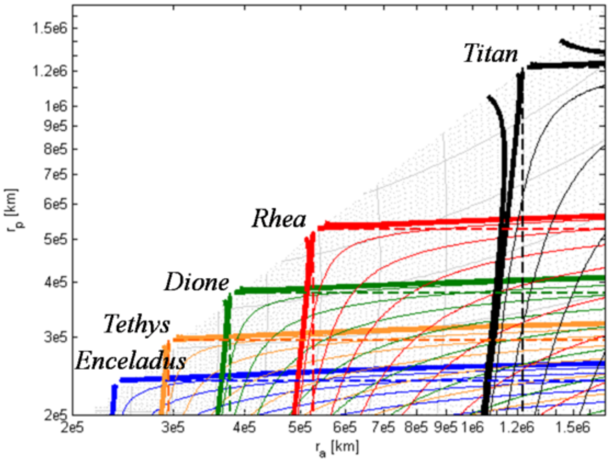

Figure 4.6: The T-P graph of the Saturn System.

where we solve for r_a, r_p giving the desired T_{M1} and T_{M2} along with the $\tilde{a}_{M1}$ and $\tilde{a}_{M2}$ for the systems of interest. We emphasize that the T-P graph provides a reliable energetic based strategy to patch the two CRTBP systems. The patch point target provides a significant advantage over prior multi-body design methodologies.

4.2.4 Three-dimensional T-P graph

In this section we consider the 3D case, where the Tisserand parameter is function of the apocenter, the pericenter, and the inclination:

$$T_M = \frac{2\tilde{a}_M}{\tilde{r}_a + \tilde{r}_p} + 2\sqrt{\frac{2\tilde{r}_a\tilde{r}_p}{(\tilde{r}_a + \tilde{r}_p)\,\tilde{a}_M}}\cos i \tag{4.10}$$

The 3D T-P graph can be used to visualize families of asteroids in the solar system[Geh09], or to analyze missions like the Solar Orbiter which uses resonant gravity assists at Venus to reach high inclinations over the ecliptic [JBC05]. Figure 4.7 shows the Earth and Jupiter Tisserand level sets, and the main-belt asteroids. Most of the main-belt asteroids are outside the surfaces $T_{Earth} = J_{L1Earth}$ and $T_{Jupiter} = J_{L1Jupiter}$. We also can see the Kirkwood gaps at the resonances[MD00] $1:4$, $3:1$, $2:5$, and $1:2$. Figure 4.8 shows the Near Earth Asteroids and, among those, the Potentially Hazardous

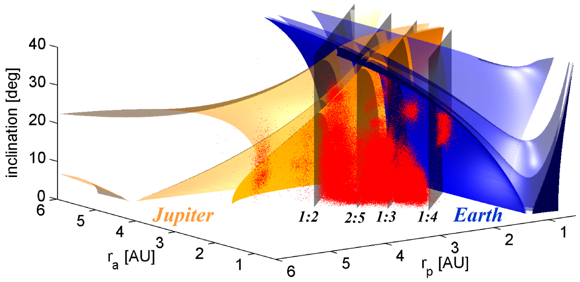

Figure 4.7: Example of a 3D T-P graph: the Earth and Jupiter level sets and the main-belt asteroids.

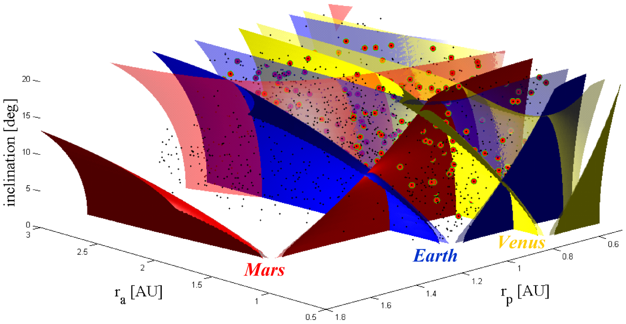

Figure 4.8: Examples of a 3D T-P graph: the Near Earth Asteroids and, among those, the Potentially Hazardous Asteroids.

Asteroids. We can see the Potentially Hazardous Asteroids are all within the level set $T_{Earth} = J_{L1Earth}$.

4.3 The anatomy of the multi-body technique

In this section we use the T-P graph to explain how the multi-body techniques are used to design endgame trajectories.

The multi-body techniques propagate the state of the spacecraft in multi-body dynamics, targeting high altitude encounters with a minor body to achieve the most suitable effect (typically a reduction or an increase of the one of the apses). Trajectories designed with multi-body techniques include the Smart1 mission to the Moon [SPC99], and the multi-moon orbiter by Ross and Lo [RL03].

4.3.1 The multi-moon orbiter

The multi-moon orbiter is a trajectory designed by Ross and Lo [RL03] for a mission to the Jovian moons. The trajectory was computed in the planar, restricted 5 body problem.

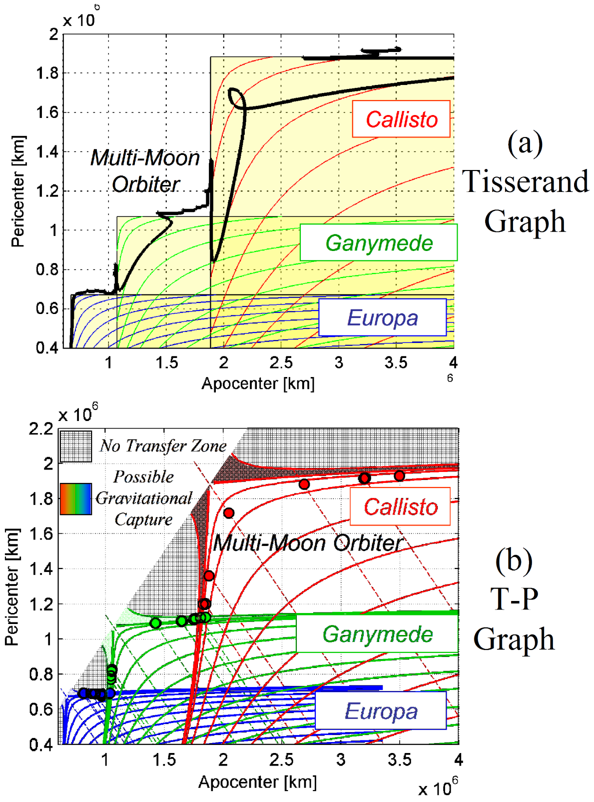

Figure 4.9: The multi-moon orbiter [RL03]. (a) The trajectory osculating parameters are plotted in the (ra,rp) conventional Tisserand graph. (b) The same trajectory is represented with the T-P graph. The T-P graphs shows that the trajectory jumps between resonances and is mostly ballistic. We can see the no-transfer zones (light gray) and the capture zones. At the end of the trajectory, the spacecraft is inside the Europa capture zone.

Figure 4.9(a) shows the Tisserand graph of the trajectory in the Jupiter system. The orbital elements vary mostly during short time intervals when the spacecraft approaches a moon, making the Tisserand graph not easy to read. Also, the osculating pericenter and apocenter are often outside the boundaries ($\tilde{r}_a > \tilde{r}_M$, $\tilde{r}_p < \tilde{r}_M$) imposed by the linked-conic model.

We now represent the same trajectory with the T-P graph. We first split the trajectory in three parts, depending on the dominating perturbing body. The first part is dominated by Callisto, the second by Ganymede and the third by Europa. For each part we place a Poincaré section on the negative x-axis of the corresponding rotating reference frame, and build the T-P graph of the transfer. The result is shown in Figure 4.9(b). We see that the spacecraft jumps between resonant orbits using flybys at the moons. Although Ross and Lo's trajectory was computed in the restricted 5 body problem, Figure 4.9(b) shows that the patched CR3BP model is a good approximation and that the T-P graph captures the main dynamics; in fact the spacecraft first shadows the T_M level sets of Callisto, then of Ganymede, and finally of Europa. The T-P graph also shows that the trajectory is quasi-ballistic[4].

4.3.2 The ballistic endgame paradox

Endgame or transfer trajectories designed with the linked-conic model always require some impulsive maneuver (Δv). The Δv is needed to increase/decrease the v_∞ from the escape/capture condition because in general the departure/arrival low-energy (low V_∞) level sets do not intersect, as shown in Figure 4.5 (a) . To decrease the required Δv, a VILT strategy can be implemented using a sequence of almost resonant orbits and small maneuvers (i.e. a zig-zag path in the $r_a - r_p$ leveraging graph). For very long transfer times a theoretical minimum Δv can be computed, as we explained in the previous chapter.

In the patched CR3BP model the T-P graph shows that the same low-energy (high Tisserand) level sets do indeed intersect. Then there might be endgames and transfers between moons which require little or no Δv, and which consist of resonant orbits only; in fact, the multi-moon orbiter trajectory[RL03] is one example of such a transfer.

Yet an interesting paradox arises when considering *planar* ballistic endgames:

---

[4] Another ballistic transfer is explained with the T-P graph in the Saturn-Titan system in [GMCM09]

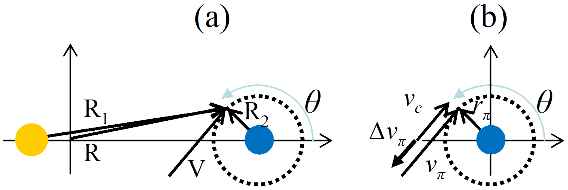

Figure 4.10: Possible orbit insertion locations at the end of an endgame strategy.

> Given a fixed Tisserand energy and arrival circular orbit altitude, the insertion maneuver costs remain essentially fixed for all possible arrival geometries.

The paradox seems to questions the utility of resonant orbits, and of quasi-ballistic endgames in general. In what follows we first prove the paradox, and then we explain why resonant orbits are still necessary for the design of low-energy endgames.

Assume a ballistic endgame begins at Europa with a very high apocenter (for example in the region II^e), and ultimately targets a low altitude circular orbit (e.g. 100 km) at Europa. In the planar case, the orbit insertion location is somewhere on a circle of radius $R_2 = r_\pi$ around Europa. Figure 4.10 shows the possible orbit insertion locations as function of the angle θ. In particular, in Figure 4.10(a) the arrival conditions are represented in the rotating reference frame; in Figure 4.10(b) the arrival conditions and the orbit insertion maneuvers Δv_π are represented in the inertial, moon-centered reference frame.

We now compute the orbit insertion maneuver as a function of the angle θ, for a given Jacobi constant and altitude at the moon. From simple geometric considerations:

$$R_1 = \sqrt{1 + r_\pi^2 + 2 r_\pi \cos\theta} \tag{4.11}$$

$$R^2 = (1-\mu)^2 + r_\pi^2 + 2(1-\mu) r_\pi \cos\theta \tag{4.12}$$

Substituting Eq.(4.11) and Eq.(4.12) in Eq.(2.8) we find that the velocity in the rotating frame is:

Moon	$\Delta v_{MAX}/\Delta v_{MIN}$ (km/s)			
	J_{L1}@100km	J_{L4}@100km	J_{L1}@1000km	J_{L4}@1000km
Europa	421.1/420.1	606.5/605.5	276.7/273.7	513.7/511.1
Titan	668.6/668.5	766.5/776.4	553.7/553.5	667.6/667.5

Table 4.1: The maximum and minimum orbit insertion maneuver (m/s) for given altitudes and Jacobi constant at Europa and at Titan.

$$V^2 = (1-\mu) + r_\pi^2 + 2\,(1-\mu)\, r_\pi \cos\theta + 2\frac{1-\mu}{\sqrt{1+r_\pi^2+2r_\pi\cos\theta}} + 2\frac{\mu}{r_\pi} - J \tag{4.13}$$

The velocity in the inertial frame is (see appendix B):

$$v_\pi = (V + \sigma r_\pi) \tag{4.14}$$

The orbit insertion/escape Δv is:

$$\Delta v_\pi = v_\pi - v_c = V + \sigma r_\pi - v_c \tag{4.15}$$

where $v_c = \sqrt{\mu/r_\pi}$. Then the orbit insertion cost depends on V. It is easy to prove that $V^2\,(\theta)$ has a global maximum at $\theta = 0$ and a global minimum at $\theta = \theta^* = \arccos\left(-r_\pi/2\right)$. Also, $\left(V^2\right)_{MAX} - \left(V^2\right)_{MIN} = r_\pi^2\,(1-\mu)\,\frac{3+r_\pi}{1+r_\pi}$, and because r_π^2 is small compared to other terms in Eq. (4.13) we infer that $V_{MAX} \approx V_{MIN}$, i.e. the velocity and thus the orbit insertion maneuver doesn't depend significantly on the angle θ.[5] Table (4.1) shows $(\Delta v_\pi)_{MAX}$ and $(\Delta v_\pi)_{MIN}$, computed for θ =0 and $\theta = \theta^*$ respectively, for several cases of interest. We see that in all cases the difference in the orbit insertion maneuver is just a few meters per seconds or less, thus given a fixed energy a ballistic endgame (which can only change θ) cannot reduce the cost significantly[6].

---

[5] It would be interesting to know if the paradox extends to the 3D case, where $R^2 = 1 + r_\pi^2\cos^2\alpha + 2r_\pi\cos\theta\cos\alpha$, $R_1 = \sqrt{1+r_\pi^2+2r_\pi\cos\theta\cos\alpha}$ and α is the elevation angle on the xy plane. The velocity in the inertial frame has two components, i.e. V and $\omega \times r$, which are not aligned in general.

[6] Non-ballistic endgame can reduce the orbit insertion maneuver by applying impulsive Δv which results in the highest change in the Jacobi constant. The VILT strategy can be justified with this argument also [Swe93]

The paradox seems to question the utility of the ballistic endgame, at least in the planar case, because no matter how we design a sequence of resonant orbits, the orbit insertion Δv is fixed by the Jacobi constant and cannot change. We wonder then why we need resonant transfers in the first place.

The T-P graph clarifies this point, and enables strategies for the design of low-cost, quasi-ballistic endgames and transfers. A low-cost , quasi-ballistic endgame at Europa, e.g., must end with a low Δv orbit insertion. Referring to Figure 4.4, the corresponding T level sets will probably lie within region II^e. Because the endgame is quasi-ballistic, the initial conditions also lie in the region II^e and according to the boundaries of the region II^e in Figure 4.5, an initial high apocenter requires an initial high pericenter, beyond Europa's orbit. How can the spacecraft, then, ever reach a 100 km altitude to Europa, an impossible scenario based on the conventional wisdom of linked-conics? The T-P graph shows, however, that if the spacecraft has the right phasing, it can use Europa perturbing force to slightly lower its apocenter AND pericenter, thus moving to the left in the T-P graph, along the level set.

Such maneuver is in fact a high altitude flyby performed close to the pericenter of the spacecraft orbit. When several high altitude flybys are linked together by free-return orbits, the pericenter can be lowered to the point where a 100 km approach at Europa is possible. Thus the high altitude flybys are necessary *to reduce the pericenter* and to reach the required altitude at Europa, while the resonant orbits simply provide a mechanism to achieve multiple flybys. We note that energy levels of the endgame scenario require non intersecting spacecraft and minor body orbits (in the exterior problem the spacecraft orbit engulfs completely the orbit of the minor body for all time while the interior problem is reversed). Therefore, the point of closest approach for the two orbits occurs only at a single point in the nonrotating frame: the apse of the spacecraft orbit. Accordingly, the low-cost endgame return orbit must be approximately resonant; whereas a non-resonant returns would necessarily have two intersection points between the spacecraft and minor body orbits.

An alternative way to explain the ballistic endgame is the following: of all the trajectories arriving at 100 km altitude at Europa with a fixed velocity defined by Eq.(3.2), the only one which starts at a very high apocenter must have performed several high altitude flybys and resonant orbits. In the next section we use this concept to design ballistic transfers.

4.4 The design of multi-body transfers with the T-P graph

The previous section showed that even for low energy levels (i.e. Tisserand parameter between J_{L1} and 3) there can be trajectories which reach a low altitude at a moon, starting at a very high apocenter, through a sequence of flybys and resonant orbits. In this section we implement a simple search to find such trajectories and design low-cost transfers between Ganymede and Europa. A similar search was implemented in the design of the BepiColombo capture trajectory at Mercury[JCGK04]; in fact at these energy levels many ballistic capture or escape trajectories can be designed[CL08, PS06, VS03], as we will show in the last chapter of this work.

We first design a transfer between a 100 km altitude orbit at Ganymede and a 100 km altitude orbit at Europa. With this set of boundary conditions we can compare the Δvs of a Hohmann transfer to the Δv of the begin-game and endgame trajectories, designed using either the multi-body technique or the VILT technique. However, we recall that longer time-of-flights yield to higher exposures to the radiation environment at Jupiter, so in practice longer time-of flight transfers are penalized by need of heavier shielding.

A direct Hohmann transfer from a 100 km altitude orbit at Ganymede to a 100 km altitude orbit at Europa requires only a few days, but costs 2.18 km/s. A VILT strategy can reduce this Δv up to a theoretical minimum of 1.71 km/s (see previous chapter). Using the T-P graph and the higher fidelity CR3BP, we demonstrate how a low-cost transfer can require significantly less propellant.

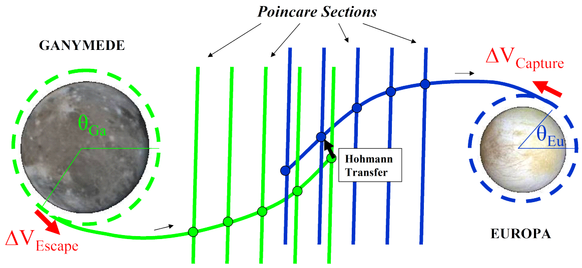

Figure 4.11: Schematic of a transfer between Europa and Ganymede designed using the T-P graph.

The basic scheme for the design is shown in Figure 4.11. We start by fixing an energy value for the escape and for the capture such that the spacecraft starts in the "escape region" II^e and ends in the "capture region" II^i. In particular, we choose

$$T \approx J = \left(J_{L2} + J_{L3}\right)/2 \tag{4.16}$$

From the Jacobi constants we find the velocities at pericenter using Eq. (3.2)[7], and calculate the cost to insert into/escape from a circular orbit at 100 km altitude from Eq.(4.15) : $\Delta v_{Escape} \cong 0.72$ km/s and a $\Delta v_{Capture} \cong 0.51$ km/s. Immediately we see that the floor for a potentially ballistic transfer Δv is $\Delta v_{Escape} + \Delta v_{Capture}$. We then scan the angles θ_{Ga}, propagate the initial conditions and store the transfers that decrease the pericenter the most in the shortest time. We also scan the angles θ_{Eu}, propagate *backwards* the initial conditions and store the transfers that increase the apocenter the most in the shortest time. In both the forward and backward propagations we have a precalculated target value for r_a and r_p respectively - from the intersection point in the TP graph - found from the solution to Eq. (4.9).

We plot the results in the T-P graph. A close up is shown in Figure 4.12. In the graph we plot the level sets corresponding to the value of the Tisserand parameter in Eq. (4.16). One of the most important features of the T-P graph is the availability of a target pericenter-apocenter for both endgame and begin-game strategies, which is at the

---

[7] In this example we do not consider the retrograde solution.

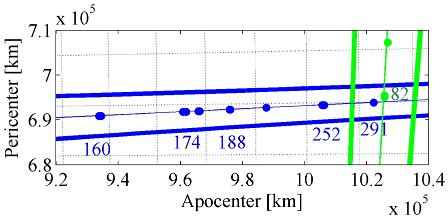

Figure 4.12: Zoom of the T-P graph showing the Ganymede escape options and the Europa capture options.

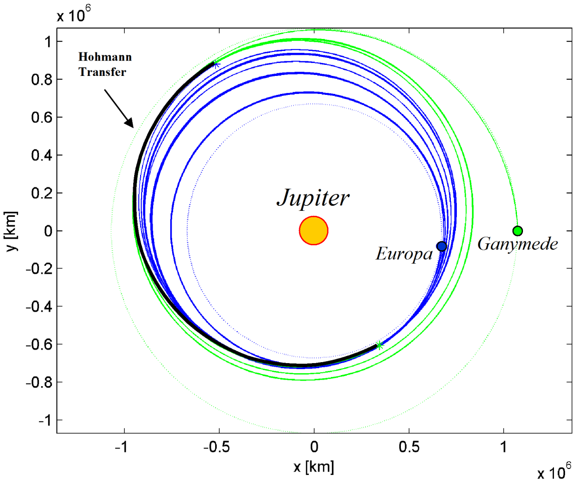

Figure 4.13: Quasi-ballistic transfer in the inertial reference frame.

intersection of the level sets. For clarity we do not plot all the Poincaré crossings from all the trajectories; we only plot the set of Pareto-optimum points (shortest time, highest apocenter) reached by all the solutions. Note that the final points of the begin-game and the initial points of the endgame do not coincide in general. Thus some impulsive maneuvers are needed to patch the two parts of the transfer; the grid in the T-P graph provides a means to estimate a brute force patching cost of a Hohmann-like transfer to connect the points in the graph. For instance we can estimate a Δv of some 70 m/s to patch the 82 day begin-game with a 252 day endgame.

Among all the possible solutions on the graph, we choose the one with lower Δv which takes $(291 + 82)$ days to transfer from Ganymede to Europa. In this case the T-P graph shows that a very little Δv (approx.10 m/s) is required to patch the begin-game with the endgame. Then the total cost of the transfer (to and from 100 km circular orbits) is mostly given by the escape and capture maneuver for a $\Delta v_{TOT} \approx 1.25$ km/s, almost 500 m/s less than the VILT theoretical minimum Δv , and almost 1 km/s less (but one year more!) than the direct Hohmann transfer.

Figure 4.14 shows the endgame and Figure 4.14 shows the begin-game part of this trajectory in the corresponding rotating reference frames. Figure 4.13 shows the same trajectories in the inertial reference frame centered at Jupiter. The figure also shows the Hohmann transfer which patches the two parts of the trajectory.

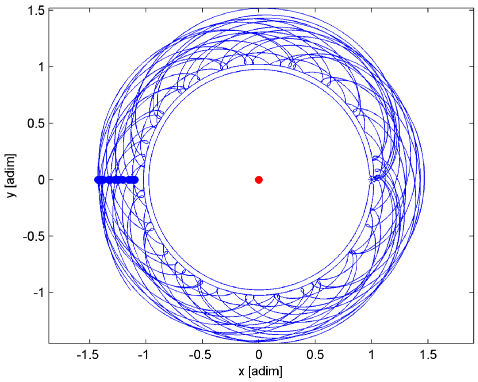

Figure 4.14: Quasi-ballistic transfer in the rotating reference frame: the endgame at Europa.

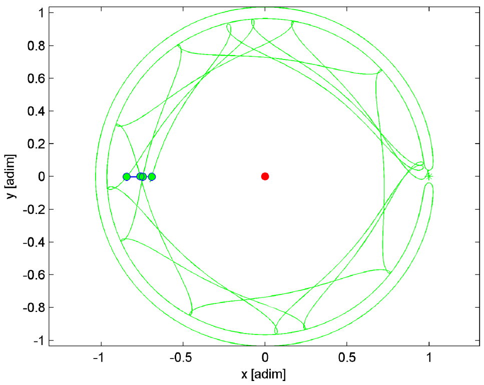

Figure 4.15: Quasi-ballistic transfer in the rotating reference frame: the begin-game at Ganymede.

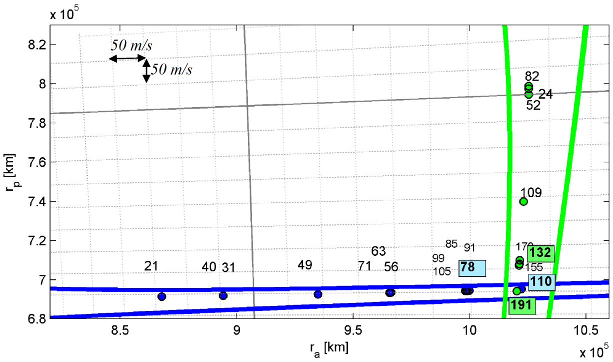

Figure 4.16: T-P graph of the transfer from a halo orbit around Ganymede to a halo orbit around Europa - projection onto the $i = 0$ plane.

A typical mission to the moons of Jupiter would not include a 100 km science orbit at Ganymede, mainly because of the very high costs of the capture and escape Δv at Ganymede. For this reason, a more interesting case for a real mission is the transfer between a halo orbit around Europa and a halo orbit around Ganymede (although the time of flight must be limited because of the radiation exposure). In this case the orbit insertion Δv and the orbit escape Δv are negligible, and the long transfer time is justified by a fully quasi-ballistic transfer. The trajectories are computed in the patched , spatial CR3BP, and the inclination at the Poincaré section never exceeds 1.5 degree.

To find suitable transfers we scan the initial position along the initial and final halo orbits and perturb the starting conditions along the unstable and stable eigendirection respectively. The initial halo orbit has a Jacobi constant in the Jupiter-Ganymede CR3BP of J=3.0052, and the final halo orbit has a Jacobi constant in the Jupiter-Europa CR3BP of J=3.0023. The energy levels are selected to be appropriate for ballistic transfers to a high altitude closed orbits about each moon [RL07].

Of all the solutions found, we show one with a reasonably low flight time and comes close to hitting the target (r_a, r_p) intersection of $(694641\,km,\ 1021834\,km)$, found from the solution to Eq. (4.9). Figure 4.16 shows the T-P graph at $i = 0$ of the begin-game and of the endgame. For simplicity, the osculating pericenter and apocenter and inclination at the Poincaré section are projected on the $i = 0$ plane (we recall that the

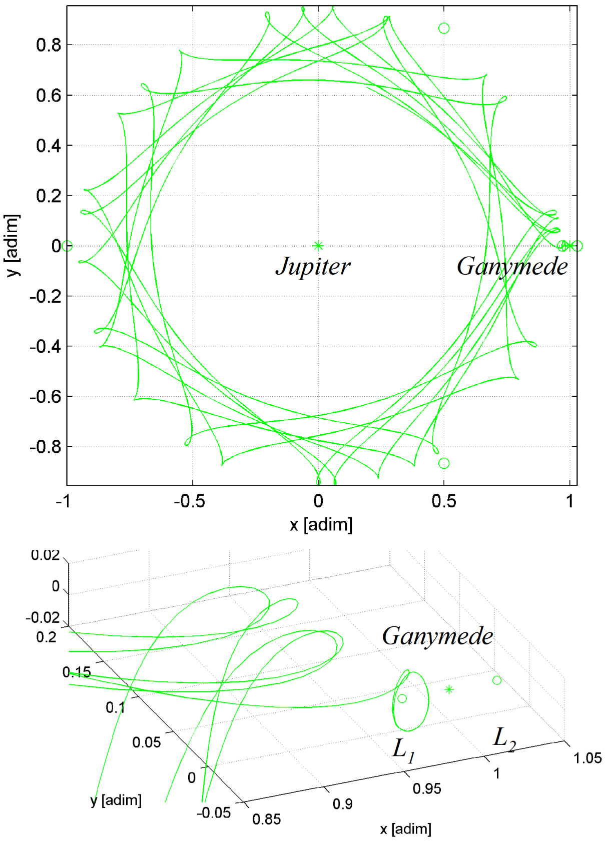

Figure 4.17: Begin-game at Ganymede, the first part of the Ganymede to Europa transfer, in the rotating reference frame.

inclination never exceeds 1.5 degrees) . The Ganymede begin-game takes 191 days to reach a very low pericenter, where it can be patched to the Europa endgame with a very little Δv. The endgame lasts 110 days. Then the whole transfer takes less than 300 days (some initial revolutions are spent on the initial and final halos) and from the T-P graph we see that almost no Δv is required to patch the two trajectories. Note that the begin-game could be reduced by two months with some additional 50 m/s , resulting in a 8-month transfer from Ganymede to Europa. Also, the begin-game can be reduced by one month with some additional 50 m/s, resulting in a 7-month transfer which costs some 100 m/s.

The next figures show some details of the 300-day transfer. Figure 4.17 shows the begin-game in the Jupiter-Ganymede CR3BP , with a close up of the escape from the

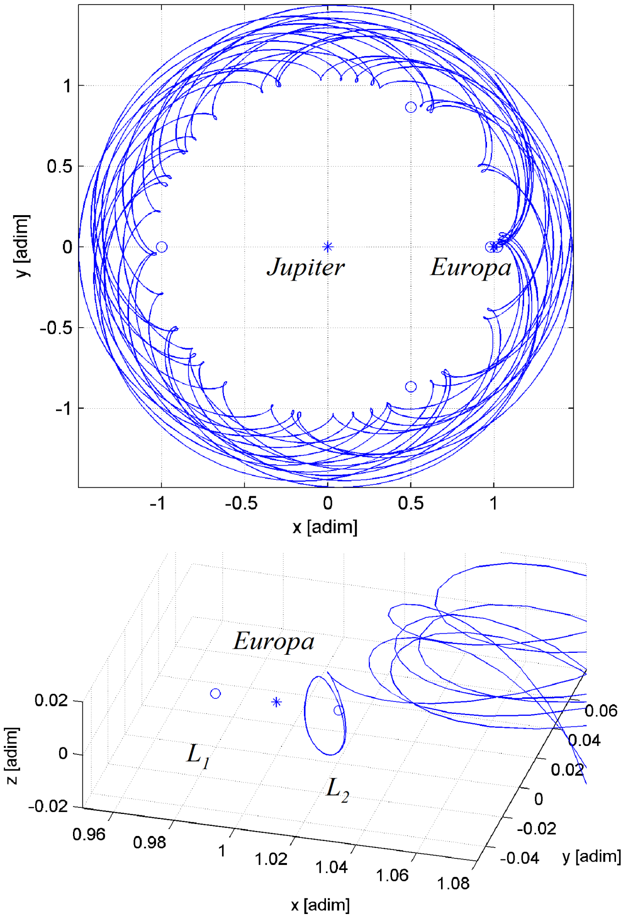

Figure 4.18: Endgame at Europa, the second part of the Ganymede to Europa transfer, in the rotating reference frame.

halo orbit. Figure 4.18 shows the endgame in the Jupiter-Europa CR3BP, with a close up of the capture into the halo orbit. In total there are 3 high altitude flybys of Ganymede and 6 high altitude flybys of Europa.

In future works we plan to optimize this trajectory or similar ones in the full ephemeris model. We do not expect the transfer time of the full-ephemeris trajectory to differ too much from the estimated value on the T-P graph. The total Δv might vary due to two important factors. On one hand the Δv can increase due to change of plane maneuvers and fourth body perturbations. On the other hand we can reduce the Δv by inserting several mid-course maneuvers along the trajectory and using an optimizer to minimize the total cost. Also we can reduce the Δv by fine-tuning the initial and final energies. Future works could also include explicit VILT-type maneuvers to shorter the time of flight of low-energy transfers.

We emphasize that the design approach outlined in this study requires no apriori knowledge of the resonant path and relies only the chaotic nature of the CR3BP and fine-scale perturbations of the initial conditions. Future work includes methods that allow specification of the resonant paths to reduce the computation requirements and provide more systematic searches. Recent works in the field also suggest some ways to achieve this goal[GR09].

Chapter 5

Exploration of low-mass moons

In this chapter we study the general (non-tangent) VILTs, which are an extension of the (tangent) VILT presented in chapter 3. Throughout this chapter, the notation VILT is referred to the general case, as opposed to the tangent VILTs.

The first section present the general VILT problem and its solution space. The main steps of the section are (1) demonstrate that the solution space is almost flat for a specific choice of coordinates, (2) construct approximated solutions using minimal memory storage. In the second section we exploit the large reduction in complexity and computational time resulting from this approximation to develop a new design method amenable for broad design space searches. In the third section we present the Enceladus orbiter trajectory.

Nomenclature

α Pump angle between the v_∞ vector and the minor body velocity vector

δ Turning angle between the incoming and outgoing v_∞ vectors of a gravity assist

$\gamma^s_{v\infty 1}$ Section of the VILT solution manifold for a given s and $v_{\infty 1}$

$\Delta\theta$ Spacecraft angular gain

σ_i Element of s: if $+1$ denotes a long ith arc, if -1 denotes a short ith arc

μ_M, μ_P Gravitational parameter of the minor and major body

EI Element of s: if $+1$ denotes exterior VILTs, if -1 denotes interior VILTs

f, E, M True, eccentric and mean anomaly of the spacecraft with respect to the major body

n Number of minor body revolutions during the VILT

m Number of major body revolutions during the VILT

k_i Element of s: number of full revolutions in the ith arc

r_π Pericenter of the gravity assist hyperbola

r_a, r_p, a Apocenter, pericenter and semi-major axis of the spacecraft with respect to the major body

r_{LA}, r_{VA} Leveraging and vacant apses of the spacecraft with respect to the major body , i.e. the furthers and closest apse to $r = 1$ respectively

s VILT parameter vector; in particular $s = (\sigma_1, k_1, \sigma_2, k_2, n, EI)$

v_p, v_a Velocity of the spacecraft at pericenter and at apocenter with respect to the major body

v_∞ Velocity of the spacecraft relative to the moon at $r = 1$

$\mathcal{V}^s$ VILT solution manifold

$1, 2$ Subscripts indicates the first or second arc

5.1 General VILTs

Generalizing the definition in chapter 3, V-infinity leveraging transfers (VILTs) are trajectories around a major body (e.g., a planet) that start and end at a minor body (e.g., a moon) and include one small impulsive maneuver (Δv) to achieve a large change in the spacecraft velocity relative to the minor body (v_∞). VILTs are usually modeled with two Keplerian arcs patched by a tangential Δv at the leveraging apse r_{LA}, while the

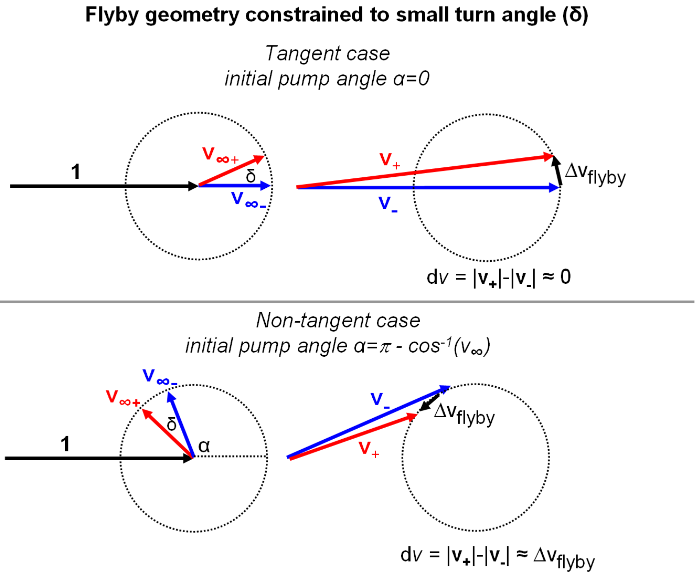

Figure 5.1: Geometry of the gravity assists when the turn angle is small

moon is in a circular coplanar orbit. In most of the literature, and in chapter 3, one of the two Keplerian transfers is assumed tangent to the moon's orbit (*tangent VILT*) to both simplify the analysis and to achieve a near optimal increase or decrease in v_∞ at the moon[VC09].

In cases where VILTs are patched together with flybys of non-massive bodies, the tangent VILT is very inefficient in terms of flight time due to geometry of the flyby. As demonstrated in Figure 5.1, the impulsive Δv vector associated with a gravity assist beginning with the tangent geometry is almost perpendicular to the spacecraft velocity, thereby leaving the magnitude of the velocity relative to the central body almost unchanged. Whereas in the case of the non-tangent flyby geometry, the Δv vector goes almost entirely towards changing the velocity magnitude. In the limit as the available turn angle approaches zero, the tangent geometry flyby provides no change in energy while the most efficient energy change occurs in the non-tangent case with pump angle equal to $(\pi - \arccos v_\infty)$. Following the work of Strange et al[SCR09]., this lack of efficiency for VILTs constrained by small turn angles motivates us to remove the tangent assumption.

We normalize the distances and the times with the scale factors $l^* = \tilde{a}_M$ and $t^* = \sqrt{\tilde{a}_M^3/\tilde{\mu}_P}$, where the tilde denotes the dimensioned variables. As a result of the normalization, $\mu_P = 1$, $v_M = 1$ and the VILTs start and end at $r = 1$. We model the gravity assist as usual by linking two consecutive VILTs with an instantaneous rotation of the v_∞vector by the turning angle $\delta = 2\arcsin\left(\tilde{\mu}_M/(\tilde{\mu}_M + \tilde{v}_\infty^2 \tilde{r}_\pi)\right)$, where $\tilde{r}_\pi$ is the pericenter of the gravity assist.

5.1.1 Classification and special solutions

We classify the VILTs with the parameter vector $s = (\sigma_1, k_1, \sigma_2, k_2, EI, n)$ and the notation:

$$(EI)\ n : m_{k1,k2}^{\sigma 1,\sigma 2}$$

where $m = k_1 + k_2 + 1$ is the number of spacecraft revolutions and the elements of p are:

$$k_i \quad i = 1, 2 \qquad \text{Number of full revolutions in the } i\text{th arc}$$

$$\sigma_i = \begin{cases} -1 & \text{Short transfer } 2k_i\pi < \Delta\theta < \pi + 2\pi k_i \\ +1 & \text{Long transfer } \pi + 2\pi k_i < \Delta\theta < 2\pi + 2\pi k_i \end{cases}$$

$$EI = \begin{cases} -1 & \text{Interior VILT } (\Delta v \text{ at apoapsis}) \\ +1 & \text{Exterior VILT } (\Delta v \text{ at periapsis}) \end{cases}$$

$$n \qquad \text{Number of moon revolutions}$$

Figure 5.2 shows an example of an exterior VILT on the left, and explains the notation for the first arc on the right. In the figure the leveraging apse r_{LA} is the apocenter, while the vacant apse r_{VA} (opposite to the leveraging apse) is the pericenter.

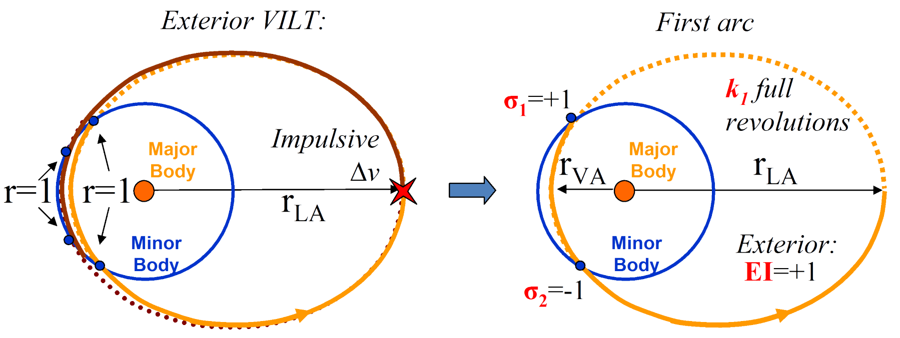

Figure 5.2: Example of exterior VILT on the left. On the right, the first arc of the VILT

A special family of VILTs is the family of tangent VILTs, described in chapter 3 with the notation $n : m^{\overline{\sigma}}(\overline{k})$, where $\overline{\sigma}, \overline{k}$ refers to the non-tangent arc. Note that $n : m^{\overline{\sigma}}(\overline{k})$ is a special case of a $(EI)\ n : m_{k1,\overline{k}}^{\sigma 1,\overline{\sigma}}$ VILT (first arc tangent to the moon's orbit) and of a $(EI)\ n : m_{\overline{k},k2}^{\overline{\sigma},\sigma 2}$ VILT (second arc tangent to the moon's orbit).

A second special family of VILT is the family of ballistic transfers, where $\Delta v = 0$ implies $r_{VA1} = r_{VA2}$. We classify the ballistic transfers with the notation $n : m^{\overline{\sigma}}$, where $\overline{\sigma} = 0$ corresponds to the ballistic *resonant* transfers, and $\overline{\sigma} = \pm 1$ correspond to nonresonant transfers with slightly more or fewer than m revolutions, respectively (also called generic or non-$n\pi$ returns). Note that $n : m^{\pm 1}$ is a special case of a $(EI)\ n : m_{k1,k2}^{\pm 1,\pm 1}$ VILT, while $n : m^{0}$ is a special case of a $(EI)\ n : m_{k1,k2}^{\pm 1,\mp 1}$ VILT.

5.1.2 Phasing constraint

Using our notation, the true and mean anomaly spanned by the spacecraft in either arc are (see also Strange at al.[SCR09]):

$$\Delta f^{(\sigma_i,k_i,EI)} = 2\pi k_i - f|_{r=1}^{(\sigma_i,EI)} + \pi[1 + \sigma_i(EI - 1)/2] \qquad i = 1, 2 \tag{5.1}$$

$$\Delta M^{(\sigma_i,k_i,EI)} = 2\pi k_i - M|_{r=1}^{(\sigma_i,EI)} + \pi[1 + \sigma_i(EI - 1)/2] \qquad i = 1, 2 \tag{5.2}$$

where $f|_{r=1}^{(\sigma_i,EI)} \in (-\pi,\pi]$ and $M|_{r=1}^{(\sigma_i,EI)} \in (-\pi,\pi]$ are the true and mean anomaly of the spacecraft at the moon. Using Eq.(5.1) and Eq.(5.2) we define the *spacecraft angular gain* :

$$(\Delta\theta)_i = \Delta f^{(\sigma_i,k_i,EI)} - a_i^{3/2}\Delta M^{(\sigma_i,k_i,EI)} \qquad i = 1,2 \tag{5.3}$$

where the second term is the true anomaly spanned by the moon , which is also the transfer time.

Due to the symmetry of the problem, each of the two arcs composing the VILT is completely defined with only two independent variables (*coordinates*), like (a_i, e_i) or (r_{ai}, r_{pi}) or $(v_{\infty i}, r_{LAi})$, $\quad i = 1,2$. Thus four coordinates completely define the VILT. However, as we patch the two arcs together, the VILT coordinates must satisfy the *apsis constraint equation*:

$$r_{LA1} = r_{LA2} \tag{5.4}$$

Also, the true anomaly spanned by the moon must equal the true anomaly spanned by the spacecraft, modulo 2π. That is , the VILT must satisfy the *phasing constraint equation*[SCR09] :

$$(\Delta\theta)_1 + (\Delta\theta)_2 = 2\pi(k_1 + k_2 + 1 - n) \tag{5.5}$$

For a choice of the VILT parameter vector $s = (\sigma_1, k_1, \sigma_2, k_2, EI, n)$ and under certain regularity conditions which we do not discuss here, the Submersion Theorem [AMR88] applied to Eq.(5.4) and Eq.(5.5) shows that the solution space of the VILT is a two-dimensional differentiable manifold. In other words, we have a four dimensional space with two constraints leaving two degrees of freedom. We denote the *VILT manifolds* with the notation $\mathcal{V}^s$, where s is the VILT parameter vector.

Table 5.1: Some useful two-body mechanics formulae as functions of r_a, r_p in normalized variables

(a, e, p)	$\left(\frac{r_a+r_p}{2} \, , \, \frac{r_a-r_p}{r_a+r_p} \, , \, \frac{2r_ar_p}{r_a+r_p}\right)$
(v_a, v_p)	$\left(\sqrt{\frac{r_p}{r_a}\frac{2}{(r_a+r_p)}} \, , \, \sqrt{\frac{r_a}{r_p}\frac{2}{(r_a+r_p)}}\right)$
v_∞	$\sqrt{3 - \frac{2}{r_a+r_p} - 2\sqrt{\frac{2r_ar_p}{r_a+r_p}}}$
$f\big\vert_{r=1}^{(\sigma_i,EI)}$	$(-\sigma EI)\arccos\left(\frac{2r_ar_p-r_a-r_p}{r_a-r_p}\right)$ and $(-\sigma EI)2\arctan\left(\sqrt{\frac{r_a}{r_p}\frac{(1-r_p)}{(r_a-1)}}\right)$
$E\big\vert_{r=1}^{(\sigma_i,EI)}$	$(-\sigma EI)\arcsin\left(2\frac{\sqrt{(1-r_p)(r_a-1)}}{r_a-r_p}\right)$ and $(-\sigma EI)2\arctan\left(\sqrt{\frac{(1-r_p)}{(r_a-1)}}\right)$
$M\big\vert_{r=1}^{(\sigma_i,EI)}$	$(-\sigma EI)\left[2\arctan\left(\sqrt{\frac{(1-r_p)}{(r_a-1)}}\right) - 2\frac{\sqrt{(1-r_p)(r_a-1)}}{r_a+r_p}\right]$

5.1.3 Coordinates

In this section we introduce some choice of coordinates (independent variables) which describes a Keplerian arc. In the next section we use these coordinates to write the constraint equations (5.4-5.5), i.e. to define the embedding space and compute the VILT manifold.

If we choose (r_a, r_p) as coordinates, many orbital parameters take a very simple form, as shown in Table 5.1. The formulae[1] in Table 5.1 are derived using the conservation of momentum and energy.

Another two choices of coordinates are (r_{LA}, v_∞) and (r_{LA}, r_{VA}) , for which we derive the following coordinate transformations:

$$\varphi : (r_{LA}, r_{VA}) \mapsto (r_a, r_p) = \begin{cases} (r_{LA}, r_{VA}) & \text{if } EI = +1 \\ (r_{VA}, r_{LA}) & \text{if } EI = -1 \end{cases} \tag{5.6}$$

and

$$\psi : (r_{LA}, v_\infty) \mapsto (r_{LA}, r_{VA}) \tag{5.7}$$

---

[1] In the table, the third third row comes from $v_\infty^2 = 1 + v|_{r=1}^2 - 2h = 1 + (2 - \frac{1}{a}) - 2\sqrt{p}$. The fourth row uses the trigonometry identity $\tan\frac{f}{2} = \pm\sqrt{\frac{1-\cos f}{1+\cos f}}$. The fifth row uses the trigonometry identity $\sin E = 2\frac{\tan(E/2)}{1+\tan^2(E/2)}$.

where r_{VA} is given by Eqs.(5.8) and (5.9)[2]

$$v_{LA} = r_{LA} - EI\sqrt{r_{LA}^2 - 3 + \frac{2}{r_{LA}} + v_\infty^2} \tag{5.8}$$

$$r_{VA} = \left(2/(r_{LA}v_{LA})^2 - 1/r_{LA}\right)^{-1} \tag{5.9}$$

5.1.4 Solution space representation

In this section we use the coordinates introduced previously to represent the VILT solution space. Other choices of coordinates are possible[SCR09].

First we write the spacecraft angular gain of Eq.(5.3) as function of (r_a, r_p) using Table 5.1:

$$\begin{aligned}\Delta\theta_{(\sigma,k,EI)}(r_a, r_p) = {} & 2\pi k + \sigma EI \arccos\left(\tfrac{2r_a r_p - r_a - r_p}{r_a - r_p}\right) + \pi[1 + \sigma(EI - 1)/2] + \\ & -\sqrt{\tfrac{(r_a + r_p)^3}{8}}\left(2\pi k + \sigma EI\left[2\arctan\left(\sqrt{\tfrac{(1-r_p)}{(r_a-1)}}\right) - 2\tfrac{\sqrt{(1-r_p)(r_a-1)}}{r_a+r_p}\right] + \pi[1 + \sigma(EI-1)/2]\right)\end{aligned} \tag{5.10}$$

Then we choose the coordinates $(r_{LA}, v_{\infty 1})$ for the first arc and (r_{LA}, r_{VA2}) for the second arc, and write the phasing constraint Eq. (5.5) using Eq.(5.10) with the coordinate transformations Eq.(5.6-5.7):

$$\Delta\theta_{(\sigma 1,k1,EI)} \circ \psi(r_{LA}, v_{\infty 1}) + \Delta\theta_{(\sigma 2,k2,EI)} \circ \psi \circ \varphi(r_{LA}, r_{VA2}) - 2\pi(k_1 + k_2 + 1 - n) = 0 \tag{5.11}$$

where the circle $\circ$ denotes function composition. For the external VILT, for instance, Eq.(5.11) looks like

---

[2] From the conservation of energy and momentum we find the quadratic: $v_{LA}^2 - 2v_{LA}r_{LA} + 2\left(1 - \frac{1}{r_{LA}}\right) + 1 - v_\infty^2 = 0$. Using energy-based arguments we can pick the correct root, as shown in the formula. The second equation is derived from the conservation of energy.

$$\begin{aligned}
&\sigma_1 \arccos\left(\frac{2r_a - r_a\left(2/\left(r_a^2-\sqrt{r_a^4+(v_{\infty1}^2-3)r_a^2+2r_a}\right)^2-1/r_a\right)-1}{r_a\left(2/\left(r_a^2-\sqrt{r_a^4+(v_{\infty1}^2-3)r_a^2+2r_a}\right)^2-1/r_a\right)-1}\right)+\\
&-\sqrt{\frac{\left(r_a+\left(2/\left(r_a^2-\sqrt{r_a^4+(v_{\infty1}^2-3)r_a^2+2r_a}\right)^2-1/r_a\right)^{-1}\right)^3}{8}}\Bigg\{\pi(2k_1+1)+\\
&+\sigma_1\Bigg[2\arctan\left(\sqrt{\frac{\left(1-\left(2/\left(r_a^2-\sqrt{r_a^4+(v_{\infty1}^2-3)r_a^2+2r_a}\right)^2-1/r_a\right)^{-1}\right)}{(r_a-1)}}\right)+\\
&-\ 2\frac{\sqrt{\left(1-\left(2/\left(r_a^2-\sqrt{r_a^4+(v_{\infty1}^2-3)r_a^2+2r_a}\right)^2-1/r_a\right)^{-1}\right)(r_a-1)}}{r_a+\left(2/\left(r_a^2-\sqrt{r_a^4+(v_{\infty1}^2-3)r_a^2+2r_a}\right)^2-1/r_a\right)^{-1}}\Bigg]\Bigg\}+\sigma_2\arccos\left(\frac{2r_ar_{p2}-r_a-r_{p2}}{r_a-r_{p2}}\right)+\\
&-\sqrt{\frac{(r_a+r_{p2})^3}{8}}\left(\pi(2k_2+1)+\sigma_2\left[2\arctan\left(\sqrt{\frac{(1-r_{p2})}{(r_a-1)}}\right)-2\frac{\sqrt{(1-r_{p2})(r_a-1)}}{r_a+r_{p2}}\right]\right)-2\pi n=0
\end{aligned}$$

For a given VILT parameter vector s, we solve numerically Eq.(5.11) to compute the two dimensional manifold $\mathcal{V}^s$ embedded in $(r_{LA}, r_{VA2}, v_{\infty1})$. We also take sections of the manifold at $v_{\infty1} = const$, which we denote as $\gamma^s_{v\infty1}$. From the Implicit Function Theorem[AMR88], we know that the sections $\gamma^s_{v\infty1}$ can be written as curves

$$r^s_{LA}(r_{VA2}; v_{\infty1}) \tag{5.12}$$

satisfying Eq.(5.11), which we can plot on a Tisserand graph.

The special families of VILTs described previously (ballistic and tangent VILTs) must satisfy one additional constraint equation ($r_{VA1} = r_{VA2}$ for the ballistic solution, $r_{VA1} = 1$ or $r_{VA2} = 1$ for tangent VILT) and are therefore one-dimensional subsets of $\mathcal{V}^s$[CR10a]. Their intersections with $v_{\infty1} = const.$ are points.

Figure 5.3 shows the manifold $\mathcal{V}^{(1,0,-1,3,+1,5)}$ associated to the $(+1)\ 5:4^{1,-1}_{0,3}$ VILT, embedded in the $(r_a, r_{p2}, v_{\infty1})$ space. It also shows the family of ballistic transfers $5:4^0$ and the VILTs tangent at departure $(+1)\ 5:4^{-1}(3)$ and at arrival $(+1)\ 5:4^{+1}(0)$. As expected, the tangent VILTs are the boundaries of the manifold. Note that the VILTs tangent at departure are not defined for $v_{\infty1}$ greater than ~ 0.15.

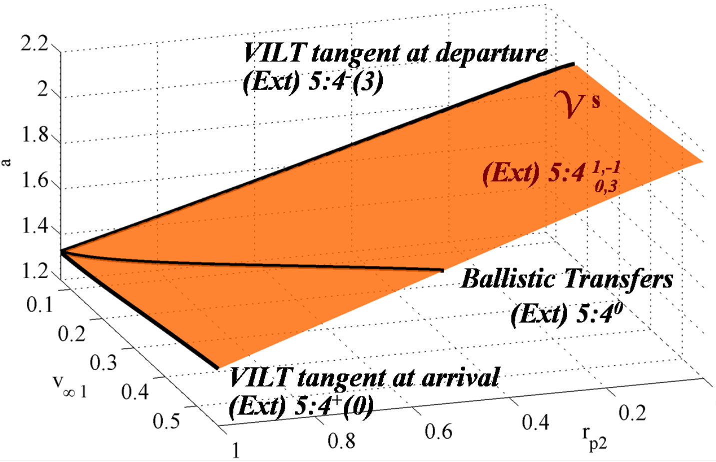

Figure 5.3: The manifold $\mathcal{V}^{(1,30,-1,3,+1,5)}$, set of the solutions to the $(+1)\ 5 : 4^{+1,-1}_{0,3}$ VILT with $v_{\infty 1} = 0.12$. The tangent VILTs $(+1)\ 5 : 4^{-1}(3)$ and $(+1)\ 5 : 4^{+1}(0)$ are at the boundary of the manifold

Figure 5.4 on the left shows a close up of the same manifold $\mathcal{V}^{(1,0,-1,3,+1,5)}$ and of the ballistic and tangent families. In the same space we plot the pericenters of the first arc r_{p1} as function of $(r_a, v_{\infty 1})$, which we compute using Eq.(5.8-5.9). The plane $v_{\infty 1} = 0.12$ generates the section $\gamma^s_{v\infty 1}$,or equivalently the curve $r_{p2} = (r_a; v_{\infty 1})$, and the curve $r_{p1}(r_a; v_{\infty 1})$, i.e. the $v_{\infty 1}$ level set of the Tisserand graph. The plane also intersects the ballistic and tangent VILTs in the points $P1$,$P2$,$P3$. The point $P2$ represents the ballistic transfer, i.e. the solution with $r_{p1} = r_{p2}$. Figure 5.4 on the right shows the same section as a Tisserand graph (see section 3.2). It is effectively a rotated frontal view of the 3D plot. In this example, the tangent VILTs are the vertical jumps from the r_{p1} curve (i.e. the $v_{\infty 1}$ level set) and the r_{p2} curve (the manifold section $\gamma^s_{v\infty 1}$). In particular, the figure shows the tangent VILTs with two solid arrows, noting that the tangent VILTs must begin or end at $r_p = 1$. The dashed arrow is an example of non-tangent VILT.

The manifold sections can have a small fold close to $r_p = 1$, so that their numerical computation using continuation methods is often cumbersome. Therefore, we suggests using $v_{\infty 2}$ as a *continuation parameter*. For advanced continuation methods we refer to Doedel at al.[DKK91].

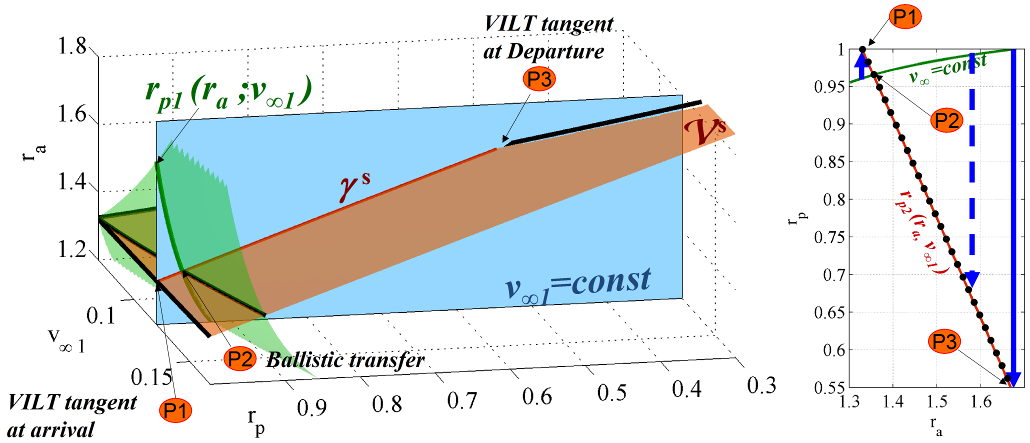

Figure 5.4: On the left, close up of the manifold $\mathcal{V}^{(1,0,-1,3,+1,5)}$ and its section at $v_{\infty 1} = 0.12$. On the right, the manifold section on the Tisserand graph (rotated frontal view of the section in the left). The points $P1$ and $P3$ are the tangent VILTs (represented with the vertical arrows), while $P2$ is the ballistic transfer

5.1.5 Piecewise linear approximation

Figure 5.3 suggests that the manifolds $\mathcal{V}^s$ and their sections $\gamma^s_{v\infty 1}$ are almost flat (with the exception of a very small region close $r_p = 1$ not visible in the picture). Then we can approximate the curves $\gamma^s_{v\infty 1}$ with linear or piecewise linear functions, which we construct using the ballistic and tangent solutions. Another approach would be to approximate the entire manifold $\mathcal{V}^s$ with one plane; in the future we envision investigating the accuracy of this second method, which would allow the storage of a family of solution manifolds with only a few parameters.

The one-dimensional solution spaces of ballistic and tangent VILTs (non-approximated) can be computed and stored easily (much more efficiently than two-dimensional $\mathcal{V}^s$)[CR10a]. In what follows we assume that the families of ballistic and tangent VILTs are stored as points $r_a(v_{\infty 1}), r_{p1}(v_{\infty 1})$ for a discrete set of v_∞ in the feasible domain $[v_{\infty 1 min}, v_{\infty 1 max}]$.

We can now compute a linear approximation of $\gamma^s_{v\infty 1}$ for a given s and $v_{\infty 1}$. We use the stored data to retrieve (up to) three points $(r_{VA2}, r_{LA}) \in \gamma^s_{v\infty 1}$:

- the ballistic solution belonging to the family of ballistic transfers $n : m^{(\sigma 1+\sigma 2)/2}$ (the point $P2$ in the example of Figure 5.4).

- the VILT tangent at departure, belonging to the family of tangent VILTs $n : m^{\sigma 2,k2}$ (the point $P3$ in the example of Figure 5.4).

- the VILT tangent at arrival, belonging to the family of tangent VILTs $n : m^{\sigma 1,k1}$(the point $P1$ in the example of Figure 5.4).

If $v_{\infty 1}$ is outside the allowed range $[v_{\infty min}, v_{\infty max}]$ for one family of tangent VILTs, we can still use two points to construct a linear instead of a piecewise linear approximation, as shown in Figure 5.5 (c). Figure 5.4 on the right shows the piecewise linear approximation with black dots. We note that the approximation completely overlaps the real solution.

For a fixed (EI) $n : m$, and for a given $v_{\infty 1}$, there are in total $4m$ curves $\gamma^s_{v\infty 1}$(one for each possible combination of σ_1, σ_2, k_1). We can compute their linear approximation by retrieving up to $3 + 2m$ stored points (one for each ballistic and tangent VILT solution). Figure 5.5 shows all the twelve curves $\gamma^s_{v\infty 1}$ for a (+1) 4 : 3 VILT with $v_{\infty 1} = 0.15$. The linear approximations are the dotted curves. Note that the VILT tangent at arrival has no solution for $k1 = 2$. In this case we only use $P1$ and $P2$ to compute the linear approximation.

5.2 Design of multiple gravity assist - multiple VILT trajectories

The graphical analysis developed in the previous section forms the basis for a new design method to compute multiple gravity assist - multiple VILT trajectories.

For the sake of clarity, in this section we consider a sequence of VILTs and gravity assists at one moon only. In particular, we are interested in the design of a sequence of VILTs and gravity assists at Dione to bring the spacecraft from a point A to a point Z

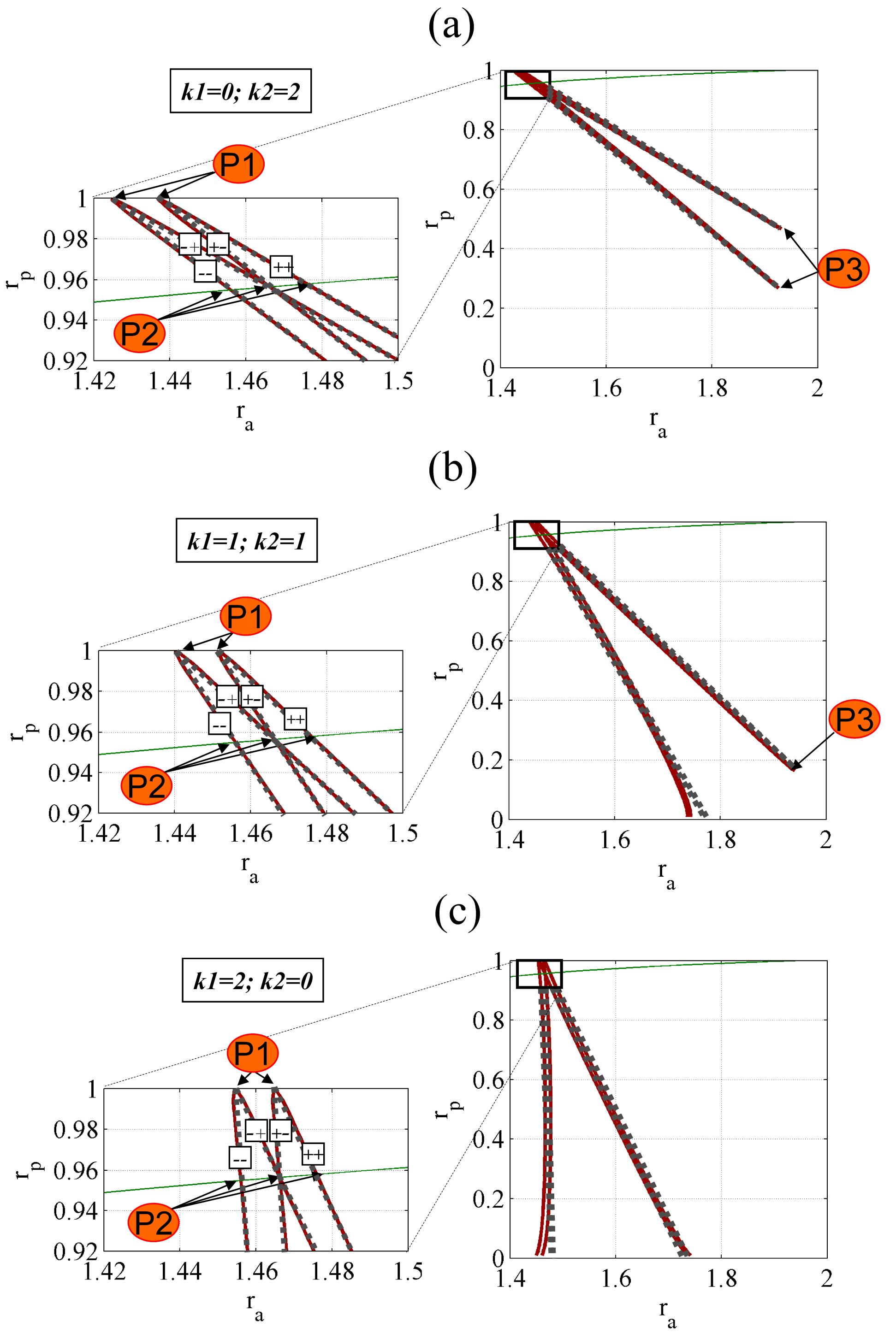

Figure 5.5: Numerical (solid line) and approximate (dots) solutions of the (+1) $4:3^{\sigma1,\sigma2}_{k1,k2}$ VILTs for $k1 = 0$ (a), $k1 = 1$ (b), and $k1 = 2$ (c). The left column shows a close up of the right pictures. The signs in the box are the signs of $(\sigma1, \sigma2)$ for the different curves

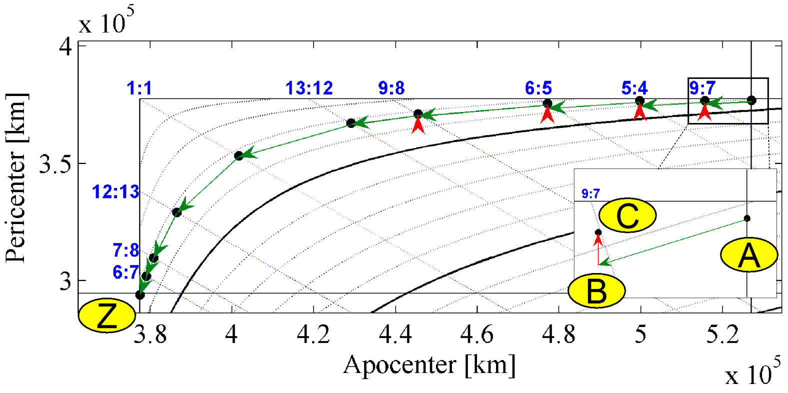

Figure 5.6: A sequence of gravity assists and VILTs at Dione brings the spacecraft from a Rhea-Dione transfer (point A) to a Dione-Tethys transfer (point Z). The solid line curves are v_∞ level sets (bold lines for $v_\infty = 1, 2, ...\text{km/s}$). The lines with slope -1 represent orbits with the same resonance. The box on the bottom right shows a close up of the first gravity assist (from A to B) and of the first VILT(from B to C)

of the Tisserand graph in Figure 5.6. Our design approach however is very general and can be equally implemented to drive the spacecraft everywhere in the Tisserand graph, depending on the mission requirements. Note that a VILT provides a mechanism to efficiently change the v_∞. If points A and Z were on the same v_∞ level set, the A to Z transfer could be accomplished using gravity assists only. In figure 5.6, the four vertical arrows represent VILTs while the arrows following the v_∞ contours are gravity assists.

5.2.1 Building block

We begin the design with one building block of the trajectory, which we call a *phase*, consisting of one gravity assist and one VILT. The first phase of the Dione part of the trajectory is shown in detail in Figure 5.6. The point A represents the initial conditions. The gravity assist moves the spacecraft to the point B on the $v_{\infty 1}$ level set. Then the VILT moves the spacecraft to the point C on a solution curve $\gamma^s_{v\infty 1}$.

How do we design this phase, i.e. how do we find the coordinates of the points B and C? We know that B must be on the $v_{\infty 1}$ level set; in order to choose a single VILT and the associated gravity assist, we could think of plotting all the solution curves $\gamma^s_{v\infty 1}$ for all the possible parameter vectors s , and choose a point on a curve satisfying some heuristic criteria (or just choose a discrete set of them). Unfortunately, for each resonant ratio $n : m$ there are $4m$ curves $\gamma^{s}_{v\infty 1}$, and each point of each curve requires solving numerically Eq(5.11). As a result, even the calculation of a discrete set of possible C would be computationally expensive; it would also produce a clouds of points difficult to visualize and evaluate.

We tackle this problem in two steps: first we limit the time of flight of the phase, i.e. we limit the number of moon revolutions n for the VILT; second for each m we replace the associated $4m$ solutions curves with 2 piecewise linear curves computed with $m+2$ stored data points. This second step is achieved with the following assumptions:

- We assume the gravity assists do not flip the sign of the flight path angle. Note that flipping the flight path angle results in a very large bending angle, and leads to inefficient (if not infeasible) gravity assists. To impose this condition, we put a constraint on σ_1 because $\sigma_1 EI$ is the sign of the flight path angle following the gravity assist. In particular, when patching two phases together we require $\sigma_1 EI = (-\sigma_2 EI)_{previous\, phase}$. This halves the number of $\gamma^{s}_{v\infty 1}$ curves to be computed.

- We use the linearized approximation to $\gamma^{s}_{v\infty 1}$ explained in the previous section; for a fixed $n : m$ and $\sigma 1$ we compute the $2m$ piecewise linear curves using $2+m$ stored data points.

- We disregard suboptimal solutions. In particular, for each $n : m$,$\sigma 1$,$\sigma 2$ we replace the m piecewise linear curves ($k1 = 0, \ldots, m-1$) with one piecewise linear curve, where for each r_{VA} we chose the minimum r_{LA} greater than r_{LAmin}. This last assumption is better explained in Figure 5.7, where we plot the $\gamma^{s}_{v\infty 1}$ for $(+1)\ 5 : 4^{-1,-1}_{k1,k2}$(with $k1 = 0, \ldots, 3\,; k2 = m - k1 - 1$) and $v_{\infty 1} = 0.3$, together with two piecewise linear curves (in bold) obtained for two different initial conditions, hence two different r_{LAmin}.

With these assumptions we compute a discrete set of possible choices for C in a very short time ($\ll 1$ second for a Matlab code on a laptop PC). We can plot the results

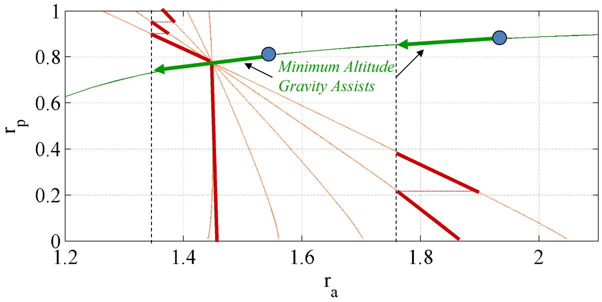

Figure 5.7: Five solution curves for the (+1) $5 : 4^{-1,-1}_{k1,k2}$VILT, and two optimal curves (piecewise linear, in bold) obtained choosing the lowest r_a for each r_p, for two different initial conditions

and apply some heuristic approach to choose the next point, or loop through them in a global search algorithm like branch and bound[LD60].

5.2.2 The sequence

The sequence of Dione VILTs and gravity assists in Figure 5.6 is designed by applying iteratively the approach explained above. The point C of the first phase becomes the new initial condition (point A) of the second phase. The last point of the last phase (the point Z) must allow a transfer to Tethys. Note that the initial and final points A and Z of the sequence are usually at different v_∞s. In Figure 5.6 $\tilde{v}_\infty = 0.82$ km/s at the initial point A , while $\tilde{v}_\infty = 0.64$ km/s at the final point Z. Accordingly, the sequence must reduce the v_∞.

The following comments about VILTs are important for the design:

- It is more efficient to reduce or increase the v_∞ if r_{VA2} is close to 1, that is on the top (left) part of the Tisserand graph for exterior (interior) VILTs. In particular, tangent VILTs maximize the change of v_∞ for a given Δv [CR10a](under the assumption of tangent burns at the apse).

- In direct contrast to the previous bullet, the gravity assist is least efficient in reducing or increasing semi-major axis if r_{VA1} is close to 1 (see Figure 5.1). As a consequence, tangent and near-tangent VILTs have an adverse affect on total transfer time. Therefore the design is a careful trade study balancing the fuel efficiency of tangent VILTs with the time efficiency of non-tangent gravity assists.

- A Δv which increases (decreases respectively) v_∞ can lead to a desired decrease (increase) of semi-major axis. In some cases the only way to reach a short time-of-flight resonance is to accept an increase (decrease) in v_∞.
- Minimum altitude gravity assists always lead to the largest change in r_a and r_p.
- Minimum altitude gravity assists do not always reduce the total transfer time. In some cases a higher altitude gravity assist can lead to a VILT with a preferred resonance (i.e. with a lower n).

Using these comments and the graphical method presented, we design the transfer in Figure 5.6 in a few steps.

5.2.3 Example of design

Using the assumptions and comments presented in the last sections, we design the first phase of the Dione part of the trajectory. The initial conditions and general assumptions are the following:

- The initial apocenter relative to Saturn is 527,063 km and the initial pericenter is 377,000 km, and $\tilde{v}_{\infty 1} = 0.82$ km/s.
- The flight path angle before the gravity assist is positive, which means that the first arc of the VILM must be short ($\sigma_1 = -1$).
- The maximum VILT time of flight is chosen as approximately 36 days, that is: $n < 14$ (the period of Dione is 2.74 days)
- The minimum gravity-assist altitude for the first encounter is 100 km and 50 km for the following gravity assists. A minimum-altitude gravity assists leads to the minimum r_a of 510,495 km.

Figure 5.8 shows the initial condition (point A) and the $\tilde{v}_{\infty 1}$ level set. It also shows some piecewise linear curves marked with empty triangles or filled circles. In the area of interest there are only three $n : m$ VILTs with $n < 14$. The $13 : 10$ VILTs are the two curves on the right, the 9:7 VILTs are the two curves in the center, and the 5:4 VILTs are the two curves on the left.

A possible choice for the design of this phase consists of a gravity assist from A to B', followed by a VILT from B' to C'. This choice has the advantage to decrease the apocenter the most, with a short time of fight of approximately 5 Dione revolutions. However, in order to reach the $5 : 4$ VILT it is necessary to apply quite a large Δv (indicated by the large vertical displacement) and increase the v_∞.

A different option is to make a gravity assist to from A to B, and a VILT from B to C which lies on the $\sigma_2 = -1$ curve. The transfer time is almost twice that of the previous option, however the Δv is much smaller and also results in a desired decrease of v_∞. In this case we choose the second option, because it represents a better compromise in the Δv vs. time-of-flight trade; however it is clear that both presented options, and probably a few more, might be considered for an exhaustive search of trajectory options. Note that the point C is close to but not exactly at $r_p = 1$, where the Δv decreases the v_∞ the most [CR10a] but the zero flight-path angle is the least efficient for an energy changing gravity assist.

Once we select C as the chosen solution, we are ready to design the second phase, with $A_{new} = C$ and $\sigma_{1new} = -\sigma_2 = +1$. We apply this design approach iteratively to find the sequence of gravity assists and VILTs shown in Figure 5.6.

5.3 Enceladus orbiter trajectory design

Using the methodology presented in the previous section, we design a trajectory from a highly elliptical orbit around Saturn (from the post-PRM orbit of the Titan Saturn System Mission[SSL+09]) to a 200 km altitude orbit around Enceladus. The trajectory

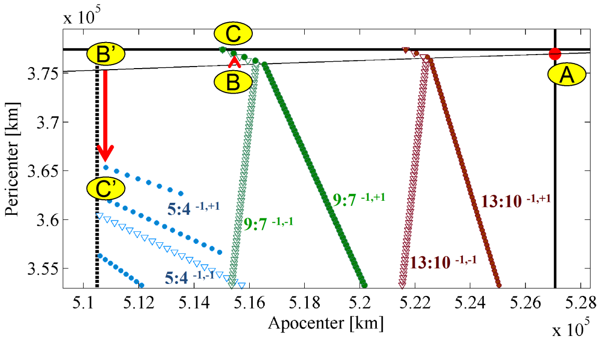

Figure 5.8: Discrete sets of possible choices for the design of the first phase of the sequence of VILTs at Dione. The curves with filled circles represents VILTs with $(\sigma_1, \sigma_2) = (-1, +1)$. The curves with empty triangles represents VILTs with $(\sigma_1, \sigma_2) = (-1, -1)$. The chosen design ABC consists of a 350 km altitude gravity assist and of a 4.7 m/s VILT

comprises 52 gravity assists and VILTs at Titan, Rhea, Dione, Tethys and Enceladus, for a total time of flight $tof \sim 2.7$ years and a total Δv of ~ 450 m/s including the Enceladus Orbit Insertion (EOI). We stress that this Δv is almost ten times less than the Titan- Enceladus Hohmann transfer Δv .

We split the trajectory into five legs : Titan , Rhea , Dione , Tethys , and Enceladus. Each leg is composed of gravity assists and VILTs at one moon only. The final conditions of each leg are taken as initial conditions for the following leg; Note that we do not design the transfer connecting two consecutive legs, which is considered beyond the scope of the work and is expected to give small contributions to the total fime of flight (a few revolutions of the gravity-assist moon) and total Δv.

The time of flights and total Δvs are recomputed solving the numerical VILTs, showing an agreement with the approximate piecewise linear VILT values within 3.3% (less than 0.02 % in most cases).

Figures 5.6 and 5.9-5.12 show the Tisserand graphs of the different legs of the trajectory, while Figures 5.13-5.17 show the trajectory in the $x - y$ plane. In each plot, the star is the location of the first flyby, while the circle is the location of the last flyby. Tables 5.2-5.6 show the Δv, gravity assist altitude, and the time of flight of all the phases of each leg. Table 5.7 summarizes the total Δv and time of flight for each phase. We

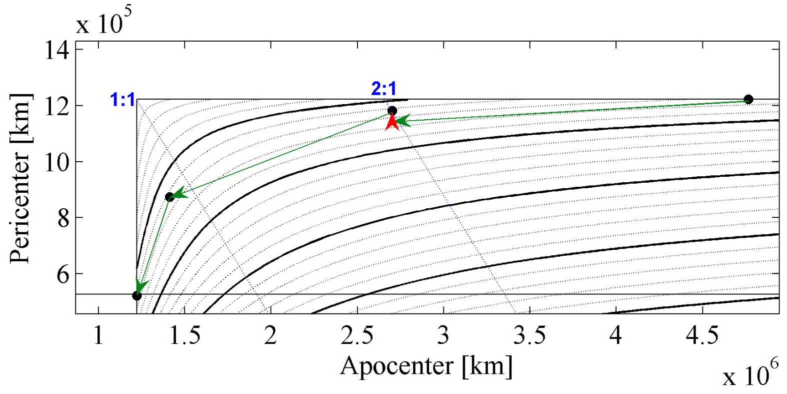

Figure 5.9: VILTs and gravity assists at Titan. The solid line curves are v_∞ level sets (bold lines for $v_\infty = 1, 2, ...\text{km/s}$). The lines with slope -1 represent orbits with the same resonance

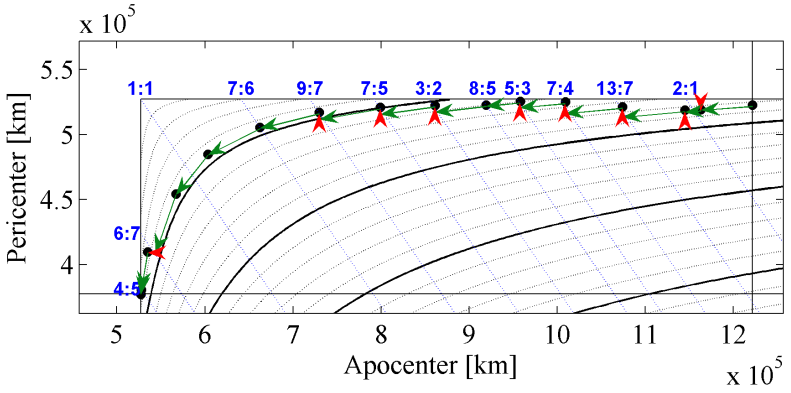

Figure 5.10: VILTs and gravity assists at Rhea. The solid line curves are v_∞ level sets (bold lines for $v_\infty = 1, 2, ...\text{km/s}$). The lines with slope -1 represent orbits with the same resonance

compare the solution described above to a second solution we found previously with a larger Δv and shorter time of flight. This second solution was presented in Strange at al. [SCR09]. We also compare both solutions with a Titan-Enceladus Hohmann transfer. For complenetess we also show the Δv for the Saturn Orbit Insertion (SOI) and Pericenter Raise Maneuver (PRM) and the associated time of flight.

Table 5.2: Titan leg

Flyby	tof [d]	Altitude [km]	Transfer Type N:M(L)	$v_{\infty 1}$ [km/s]	$v_{\infty 2}$ [km/s]	ΔV [m/s]
Titan-1	31.4	2280	$(+1)\ 2:1_{0,0}^{-1,+1}$	1.46	1.26	28.8
Titan-2	21.3	3000	$1:1^{+1,+1}$	1.26	1.26	0.0
Titan-3	—	15090	*transfer to Rhea*			

Table 5.3: Rhea leg

Flyby	tof [d]	Altitude [km]	Transfer Type N:M(L)	$v_{\infty 1}$ [km/s]	$v_{\infty 2}$ [km/s]	ΔV [m/s]
Rhea-1	9.5	100	$(+1)\ 2:1_{0,0}^{+1,+1}$	1.66	1.68	1.9
Rhea-2	17.5	2510	$(+1)\ 2:1_{0,0}^{-1,-1}$	1.68	1.67	1.4
Rhea-3	59.2	60	$(+1)\ 13:7_{1,5}^{+1,+1}$	1.67	1.50	21.5
Rhea-4	39.1	70	$(+1)\ 7:4_{2,1}^{-1,-1}$	1.50	1.30	25.1
Rhea-5	22.7	70	$(+1)\ 5:3_{0,2}^{+1,-1}$	1.30	1.20	12.7
Rhea-6	36.1	270	$8:5^{+1,-1}$	1.20	1.20	0.0
Rhea-7	13.6	150	$(+1)\ 3:2_{0,1}^{+1,-1}$	1.20	1.09	14.6
Rhea-8	31.7	150	$(+1)\ 7:5_{0,4}^{+1,-1}$	1.09	0.99	15.2
Rhea-9	40.7	120	$(+1)\ 9:7_{0,6}^{+1,-1}$	0.99	0.90	16.9
Rhea-10	31.6	230	$7:6^{+1,-1}$	0.90	0.90	0.0
Rhea-11	6.5	220	$1:1^{+1,+1}$	0.90	0.90	0.0
Rhea-12	6.2	310	$1:1^{+1,+1}$	0.90	0.90	0.0
Rhea-13	30.2	60	$(-1)\ 6:7_{6,0}^{-1,-1}$	0.90	0.74	37.2
Rhea-14	18.1	50	$4:5^{+1,-1}$	0.74	0.74	0.0
Rhea-15	—	3660	*transfer to Dione*			

Table 5.4: Dione leg

Flyby	tof [d]	Altitude [km]	Transfer Type N:M(L)	$v_{\infty 1}$ [km/s]	$v_{\infty 2}$ [km/s]	ΔV [m/s]
Dione-1	28.0	350	$(+1)\ 9:7_{0,6}^{-1,-1}$	0.82	0.78	4.7
Dione-2	13.7	270	$(+1)\ 5:4_{0,3}^{+1,-1}$	0.78	0.71	10.3
Dione-3	16.5	100	$(+1)\ 6:5_{0,4}^{+1,-1}$	0.71	0.65	9.3
Dione-4	24.6	60	$(+1)\ 9:8_{0,7}^{+1,-1}$	0.65	0.64	1.9
Dione-5	35.6	960	$13:12^{+1,-1}$	0.64	0.64	0.0
Dione-6	2.7	120	$1:1^{+1,-1}$	0.64	0.64	0.0
Dione-7	32.8	60	$12:13^{-1,+1}$	0.64	0.64	0.0
Dione-8	19.2	190	$7:8^{-1,+1}$	0.64	0.64	0.0
Dione-9	16.4	970	$6:7^{-1,+1}$	0.64	0.64	0.0
Dione-10	—	620	*transfer to Tethys*			

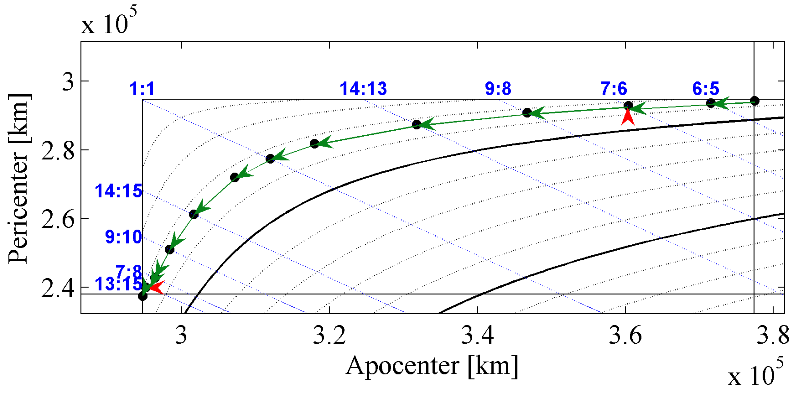

Figure 5.11: VILTs and gravity assists at Tethys.The solid line curves are v_∞ level sets (bold lines for $v_\infty = 1, 2, ...$km/s). The lines with slope -1 represent orbits with the same resonance

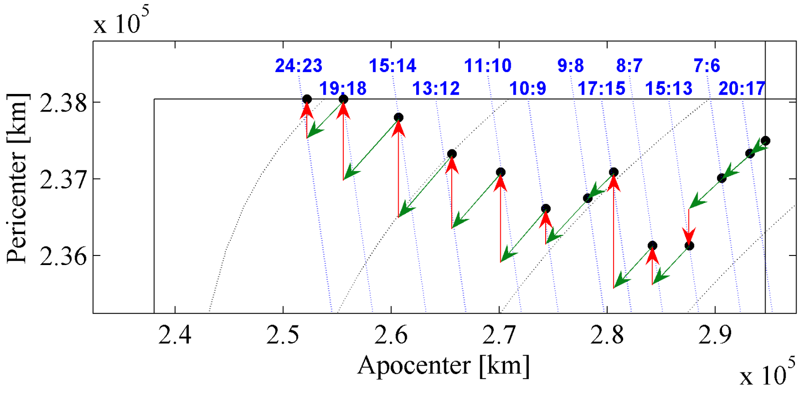

Figure 5.12: VILTs and gravity assists at Enceladus.The solid line curves are v_∞ level sets. The lines with slope -1 represent orbits with the same resonance

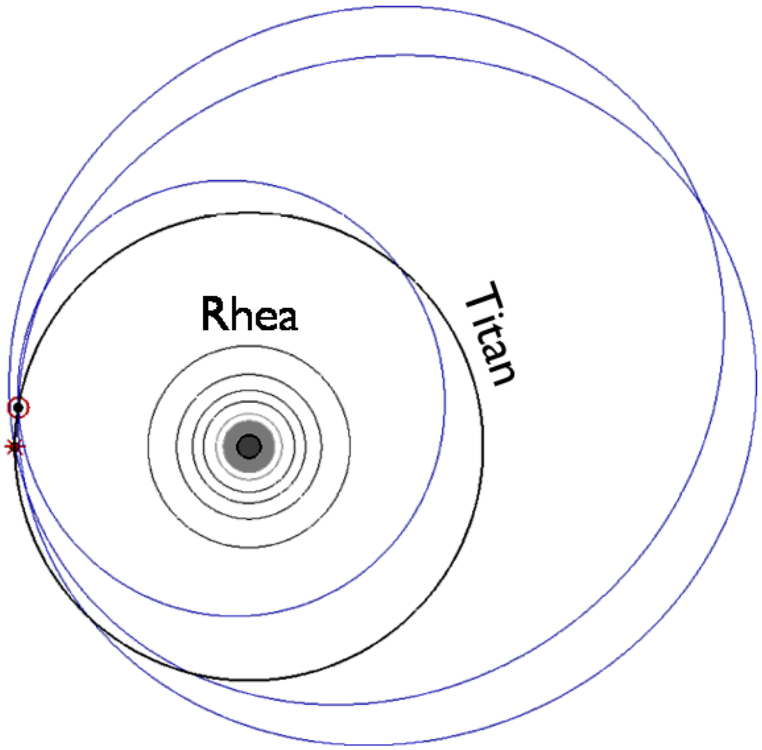

Figure 5.13: VILTs and gravity assists at Titan

Table 5.5: Tethys leg

Flyby	tof [d]	Altitude [km]	Transfer Type N:M(L)	$v_{\infty 1}$ [km/s]	$v_{\infty 2}$ [km/s]	ΔV [m/s]
Tethys-1	13.4	250	$6:5^{-1,-1}$	0.70	0.70	0.0
Tethys-2	13.2	60	$(+1)\ 7:6^{+1,-1}_{0,5}$	0.70	0.66	6.0
Tethys-3	17.0	60	$9:8^{+1,-1}$	0.66	0.66	0.0
Tethys-4	26.4	70	$14:13^{+1,-1}$	0.66	0.66	0.0
Tethys-5	2.7	60	$1:1^{+1,+1}$	0.66	0.66	0.0
Tethys-6	1.9	640	$1:1^{+1,-1}$	0.66	0.66	0.0
Tethys-7	2.6	610	$1:1^{+1,+1}$	0.66	0.66	0.0
Tethys-8	26.4	80	$14:15^{-1,+1}$	0.66	0.66	0.0
Tethys-9	17.0	90	$9:10^{-1,+1}$	0.66	0.66	0.0
Tethys-10	13.2	100	$7:8^{-1,+1}$	0.66	0.66	0.0
Tethys-11	24.5	1020	$(-1)\ 13:15^{-1,+1}_{14,0}$	0.66	0.63	6.2
Tethys-12	—	860	*transfer to Enceladus*			

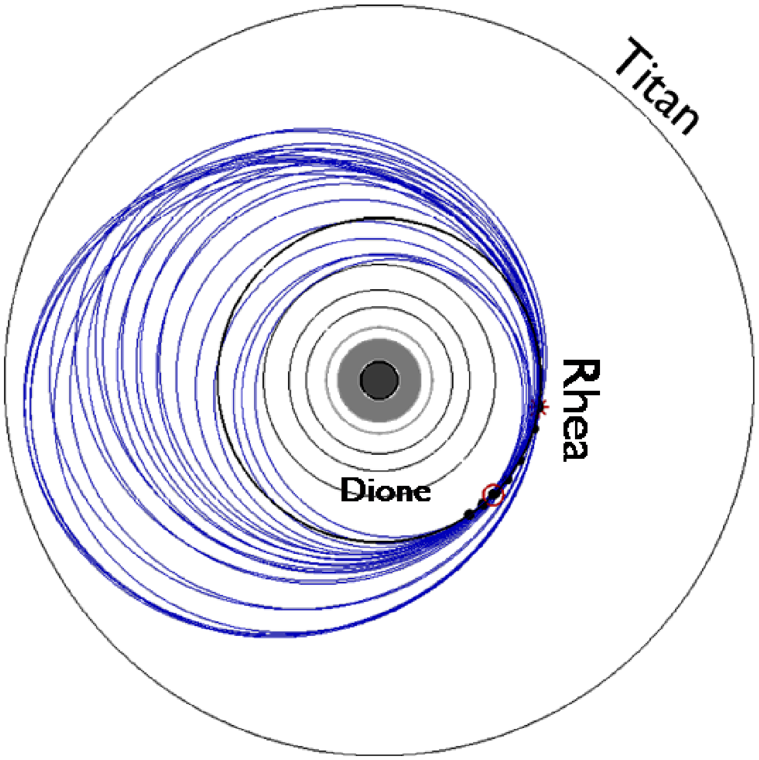

Figure 5.14: VILTs and gravity assists at Rhea

Table 5.6: Enceladus leg

Flyby	tof [d]	Altitude [km]	Transfer Type N:M(L)	$v_{\infty 1}$ [km/s]	$v_{\infty 2}$ [km/s]	ΔV [m/s]
Enceladus-1	27.4	240	$20 : 17^{+1,-1}$	0.70	0.70	0.0
Enceladus-2	9.6	50	$7 : 6^{+1,-1}$	0.70	0.70	0.0
Enceladus-3	20.7	50	$(+1)\ 15 : 13^{+1,+1}_{4,8}$	0.70	0.74	6.1
Enceladus-4	12.3	50	$(+1)\ 8 : 7^{-1,-1}_{3,3}$	0.74	0.70	6.5
Enceladus-5	23.3	50	$(+1)\ 17 : 15^{+1,-1}_{1,13}$	0.70	0.59	19.3
Enceladus-6	12.3	190	$9 : 8^{+1,-1}$	0.59	0.59	0.0
Enceladus-7	13.9	50	$(+1)\ 10 : 9^{+1,+1}_{0,8}$	0.59	0.56	5.8
Enceladus-8	16.4	50	$(+1)\ 11 : 10^{-1,-1}_{0,9}$	0.56	0.47	15.1
Enceladus-9	18.0	50	$(+1)\ 13 : 12^{+1,+1}_{8,3}$	0.47	0.40	12.5
Enceladus-10	20.5	50	$(+1)\ 15 : 14^{-1,+1}_{0,13}$	0.40	0.30	16.8
Enceladus-11	25.9	50	$(+1)\ 19 : 18^{-1,+1}_{1,16}$	0.30	0.22	13.6
Enceladus-12	32.8	50	$(+1)\ 24 : 23^{-1,+1}_{19,3}$	0.22	0.18	6.4

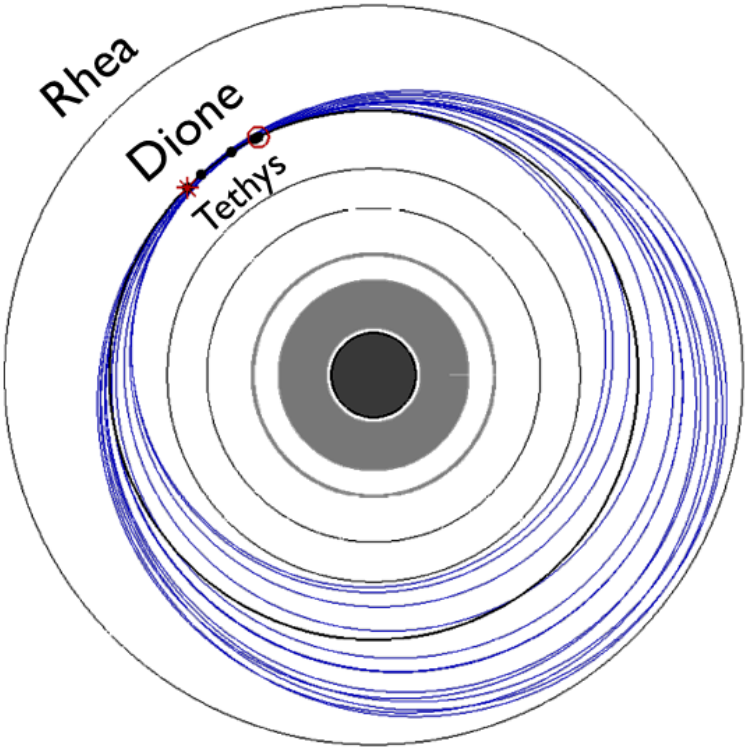

Figure 5.15: VILTs and gravity assists at Dione

Table 5.7: Trajectory comparison

	New tour		Tour from Strange et al.[SCR09]		Titan-Enceladus	
	Δv [m/s]	tof [days]	Δv [m/s]	tof [days]	Δv [m/s]	tof [days]
SOI+PRM	1,310	—	1,310	—	1,292	—
Titan tour	29	53	27	53	0	~ 50
Rhea tour	146	363	251	304	—	—
Dione tour	26	190	90	108	—	—
Tethys tour	12	158	28	134	—	—
Encel. tour	102	233	96	144	—	—
EOI	129	—	242	—	3,933	—
Tours + EOI	445	997 (2.7 y)	734	743 ($\sim$ 2.0 y)	3,933	~ 50

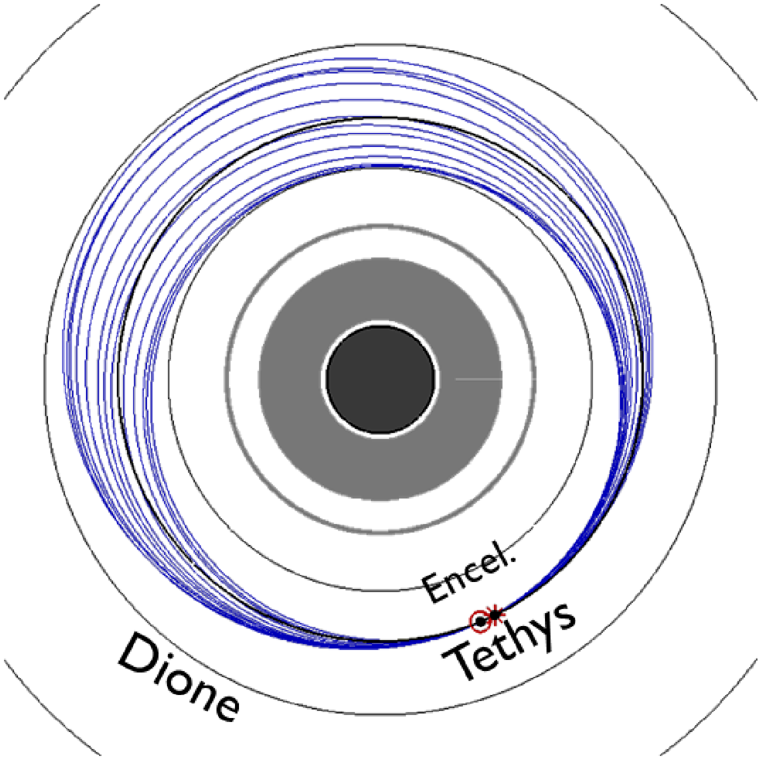

Figure 5.16: VILTs and gravity assists at Tethys

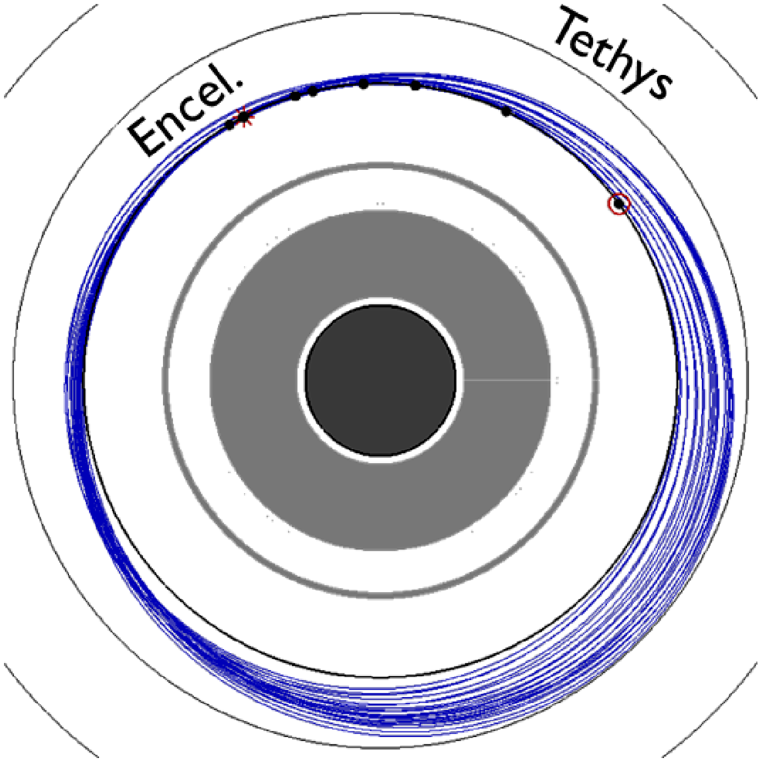

Figure 5.17: VILTs and gravity assists at Enceladus

Chapter 6

Subregions of motion and elliptic halos in the ER3BP

In this chapter we define new regions of motion and families of periodic orbits in the spatial elliptic restricted three body problem (ER3BP). Periodic orbits and regions of motion are fundamental keys to understand any dynamical system; for this reason the Hill's surfaces or the families of halo orbits have been extensively studied in the frame of the circular restricted three body problem. It is our opinion that their natural extensions to the ER3BP have not been studied enough. We divide the configuration space into forbidden subregions, subregions of motion and low-velocity subregions. We use these notions to define necessary condition for a transfer trajectory in the ER3BP. Also we compute branches of elliptic halo orbits bifurcating from halo orbits in the circular restricted three body problem. The new periodic orbits have principal periods and stability properties different from those of the originating halo orbit.

6.1 Introduction

In the last decades, several authors studied the model of the circular restricted three-body problem to explore low-energy transit trajectories [KLMR00], inspiring very challenging mission design.

We recall from chapter 2 that the CR3BP studies the motion of an infinitesimal body under the gravitational attraction of two massive bodies (primaries) in circular motion around their center of mass. Choosing a rotating reference frame that keeps the position of the primaries fixed results in a set of autonomous ordinary differential equations.

The dynamical system is Hamiltonian with the Hamiltonian as integral of motion. The existence of a first integral helps define regions of motion and families of periodic orbits with their stable and unstable manifolds. Those are key elements to understand any dynamical system.

However, the motion of the planets in the solar system is better approximated by elliptic orbits, with eccentricity varying from 0.01 up to 0.2 (for the Sun-Mercury system). The elliptic restricted three-body problem (ER3BP) takes into account the eccentricity of the orbit of the primaries, and it is therefore a more accurate model than the CR3BP. Yet the ER3BP has not been studied much, because it is a more complex system than the CR3BP. The equations of motion of the ER3BP are non-autonomous because the distance between the primaries varies in time. The system does not possess an integral of motion (although it may when averaged appropriately [PYFN06]), which suggests that the ER3BP is a dynamical problem different from the CR3BP.

For instance, the CR3BP model allows one to compute families of periodic orbits, although no real periodic orbit exists in the real solar system. The ER3BP shows that only discrete periodic orbits exist for $e \neq 0$, with a well determined period, rather than families with continuously varying periods. These solutions are (almost) periodic also in the ephemeris model: Figure 6.1 shows a periodic orbit in the sun-Mercury system, integrated in the ER3BP (solid line) and in the full ephemeris (dotted line, one dot per day). We call this periodic orbit an elliptic halo orbit since it is computed from continuation of a halo orbit in the CR3BP into the ER3BP.

The ER3BP should be used in the preliminary or PhaseA space mission trajectory design, if the eccentricity of the system under study is too large to use the CR3BP. In the next chapter we will show that the gravitation capture trajectory of the BepiColombo mission to Mercury is designed in the ER3BP and can be explained using manifolds of quasi-periodic orbits in the ER3BP

In an effort to better understand the differences between the CR3BP and the ER3BP, this chapter describes some of the important feature of the ER3BP: regions of motion

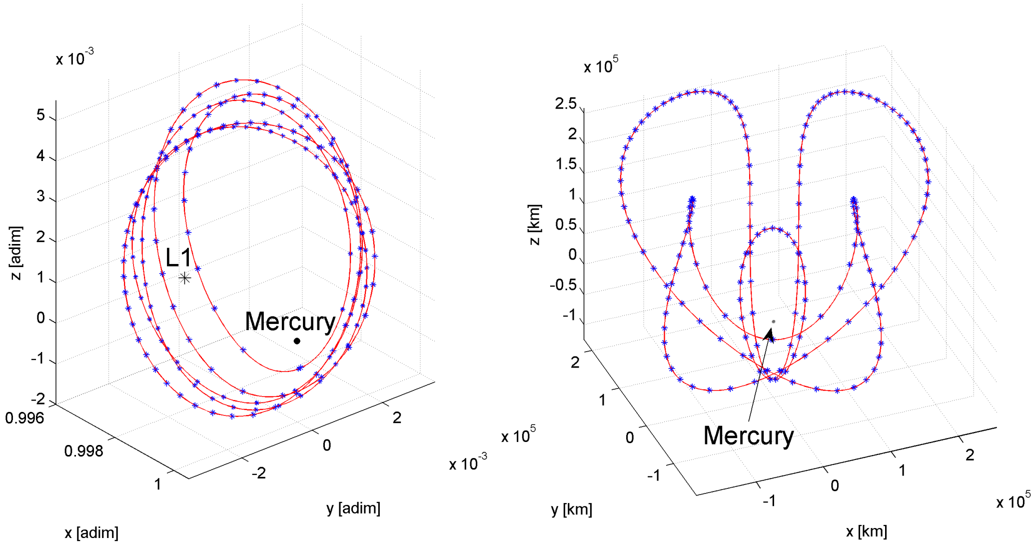

Figure 6.1: Periodic orbit in the Sun-Mercury system. We call these orbits *elliptic halo orbits*, as they are computed starting from halo orbits in the CR3BP . The left plot is in the rotating reference frame, the right plot is in the Mercury equatorial reference frame. the mercury equatorial reference frame is an inertial frame centered in Mercury. The solid line is the trajectory integrated in the ER3BP, the dotted line is the trajectory integrated with full ephemeris (one dot per day). This shows the ER3BP is a very accurate model for trajectories in the Sun-Mercury system.

and periodic orbits. The main approach consists in considering the eccentricity e as a continuation parameter: For $e = 0$ the equations of motion reduce to the CR3BP.

In the first section we introduce the equations of motion of ER3BP isolating the terms containing the eccentricity. In the second section we discuss the properties of the pulsating zero-velocity surfaces and define new subregions of motion for the elliptic problem. The forbidden subregions, subregions of motion and low-velocity subregions are bounded by pulsating surfaces. In the last section we compute branches of periodic orbits at different e, bifurcating from special halo orbits in the CR3BP. We show that the stability properties change as soon as $e \neq 0$, and we believe that a countable infinity of bifurcations occur at $e = 0$, filling the bifurcation diagram with infinitely many (although discrete) branches. This provides some insight on the existence and stability of the quasi-periodic halo orbits in the full ephemeris model.

6.2 Spatial, elliptic, restricted three-body problem

In the elliptic restricted three body problem the two primaries move on elliptic orbits around their barycenter. Unlike the CR3BP, the ER3BP is a non-autonomous system of ODE's. The eccentricity e of the orbit of the primaries appears as a parameter. The motion of the third body m_3 is usually described in a pulsating reference frame, where the position of the primaries is fixed along the $x-axis$ (the *syzygy* axis) and their mutual distance is normalized to 1; as in the CR3BP, we define the the *normal plane* as the plane throught the X-axis perpendicular to the primary orbit. Again, the true anomaly of the primaries is the preferred independent variable instead of time. The system of ODE's can be written in the following form:

$$\begin{cases} \ddot{X} - 2\dot{Y} = \frac{\partial \Omega_C}{\partial X} - \frac{e\cos f}{1+e\cos f}\frac{\partial \Omega^*}{\partial x} \\ \ddot{Y} + 2\dot{X} = \frac{\partial \Omega_C}{\partial Y} - \frac{e\cos f}{1+e\cos f}\frac{\partial \Omega^*}{\partial y} \\ \ddot{Z} = \frac{\partial \Omega_C}{\partial Z} - \frac{e\cos f}{1+e\cos f}\frac{\partial \Omega^*}{\partial Z} \end{cases} \tag{6.1}$$

$$\Omega^*(X,Y,Z) = \Omega_C + \frac{1}{2}Z^2$$

Here we isolated the term $\frac{e\cos f}{1+e\cos f}$ which is the only one containing the independent variable as well as the eccentricity. For $e = 0$, the equations of motion of the ER3BP reduce to Eq. (2.6); therefore solutions of the CR3BP are also solutions of the ER3BP when the eccentricity vanishes. In fact we will show that some special solutions of the CR3BP can be continued to the ER3BP using the eccentricity as continuation parameter, and that a bifurcation occurs at $e = 0$.

The Lagrangian points are also fixed points for the ER3BP. However, it is not possible to find an integral of motion because the equations of motion (and the Hamiltonian $\mathcal{H}$) depend explicitly on the independent variable f. The constant of integration, which was the Jacobi constant in the CR3BP, is now replaced by:

$$J_E = 2\Omega_C - V^2 - (A + I) = J_C - (A + I) \tag{6.2}$$

where we introduced an integral term I and a pulsating term A[1]

$$I = 2\int_{f_0}^{f} \Omega^* \frac{e \sin f}{(1 + e\cos f)^2} df$$

$$A = 2\Omega^* \frac{e \cos f}{1 + e \cos f}$$

Note that J_E is not an integral of motion for the ER3BP as it is no longer constant along a trajectory, but depends on the initial $\mathbf{X}(t_0)$ and the initial true anomaly, f_0. However, Eq (6.2) is actually a function f as well. The interesting thing is that $J_E(f_0, \mathbf{X}(f_0), f)$ is a constant, equal to $J_E(f_0, \mathbf{X}(f_0), f)$. However, choosing different initial conditions within the same trajectory results in different J_E's: we cannot uniquely associate a trajectory to a single value of J_E. This is one of the important consequence of the loss of the integral of motion in the ER3BP when $e \neq 0$. In the rest of the paper we will discuss how this loss affects the forbidden regions and the periodic orbits.

6.3 Subregions of motion

From the definition of the constant of integration J_E, the velocity squared is given by:

$$V^2 = 2\Omega_C - A - I - J_E$$

---

[1] In literature:

$$\begin{cases} x'' - 2y' = \frac{\partial \omega_E}{\partial X} \\ y'' + 2x' = \frac{\partial \omega_E}{\partial Y} \\ z'' = \frac{\partial \omega_E}{\partial Z} \end{cases}$$

with $\omega_E\,(x, y, z, f; e) = \frac{\Omega_E}{1+e\cos(f)}$ and $\Omega_E\,(x, y, z, f; e) = \frac{1}{2}\left(x^2 + y^2 - z^2 e\cos f\right) + \frac{1-\mu}{r_1} + \frac{\mu}{r_1} + \frac{1}{2}\mu(1-\mu)$.

Also the constant of integration is commonly expressed as $J_E = 2\omega_E - V^2 - 2e\int_{f_0}^{f} \Omega_E \frac{\sin f}{(1+e\cos f)^2} df - 2e\int_{f_0}^{f} \frac{z^2 \sin f}{(1+e\cos f)}$, so that by comparing with Eq. (6.2) : $I \equiv 2e\int_{f_0}^{f} \Omega_E \frac{\sin f}{(1+e\cos f)^2} df + 2e\int_{f_0}^{f} \frac{z^2 \sin f}{(1+e\cos f)}$ and $2\Omega_C - A \equiv 2\omega_E$

Given a set of initial condition , zero-velocity surfaces in the ER3BP are the level sets of the function:

$$2\Omega_C - A - I = J_E(f_0, \mathbf{x_0}) \tag{6.3}$$

The forbidden region is the set $\mathcal{F}_f = \{(X, Y, Z)|(2\Omega_C - A - J_E) < I\}$ and the region of motion is the set $\mathcal{A}_f = \{(X, Y, Z)|(2\Omega_C - A - J_E) > I\}$, where the subscript f indicates that the set changes with the true anomaly.

In this section we discuss the quasi-steady approach, first proposed by Szebehely[Sze67a] to compute approximate zero-velocity surfaces, and then introduce an alternative approach leading to the definition of subregions of motions.

6.3.1 Pulsating zero-velocity surfaces

Because of the integral term I, Eq. (6.3) cannot be solved for (X, Y, Z) at a time $f_1 \neq f_0$. The *quasi-steady* approach neglects the integral term when $|f_1 - f_0| = \delta f$ is sufficiently small. The quasi-steady approach was formulated for the planar ER3BP and it is often used assuming small out-of-plane motion. Eq. (6.3) then becomes

$$\frac{2\Omega_C}{1 + e\cos(f)} = 2\Omega_C - A = J_E$$

At each instant $f^* \in [f_0, f_1]$, the level set of $2\Omega_C = J_E(1 + e\cos f^*)$ defines new zero-velocity surfaces[2]. Because of the $\cos f*$ term, these surfaces get closer and further to the primaries (in the non-dimensional reference frame) as the true anomaly f goes from $-\pi$ to π. Thus they are usually referred to as *pulsating* zero-velocity surfaces.

Yet even for very small δf the quasi-steady approach can result in very large errors. Figure 6.2 shows an orbit with period 2π in the Sun-Mercury ER3BP. At $f_0 = \pi$ the third body is on the X-axis with zero velocity; thus the initial zero-velocity surfaces include the initial position. After just a few instants, the zero-velocity surfaces shrinks

---

[2] For $z \neq 0$ the zero-velocity surfaces are the level sets of $2\Omega_C - z^2 e\cos f^* = J_E(1 + e\cos f^*)$

to half their initial initial sizes, and the forbidden regions now include the instantaneous third body location.

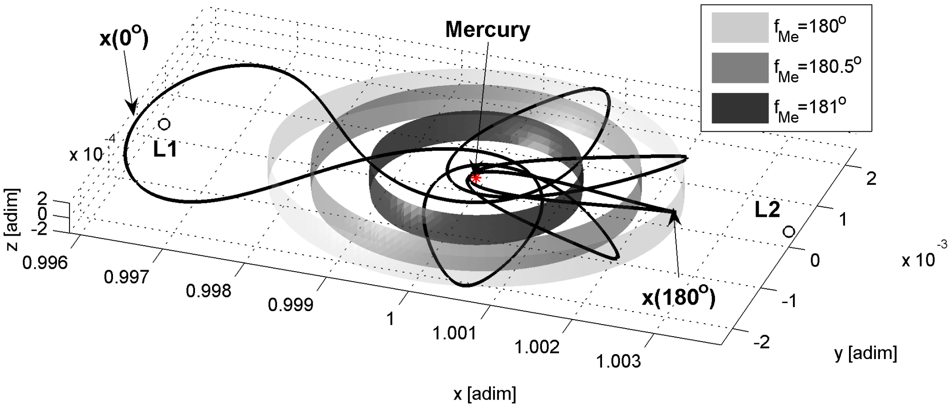

Figure 6.2: Pulsating zero-velocity surfaces in the Sun-Mercury system. f_{Me} is the true anomaly of Mercury. At time $f_{Me} = 180^o$ the initial velocity is zero; the zero-velocity surfaces are tangent to the initial point. However, after just a few instant the pulsating surfaces have shrunken to half their size, while the third body has barely moved.

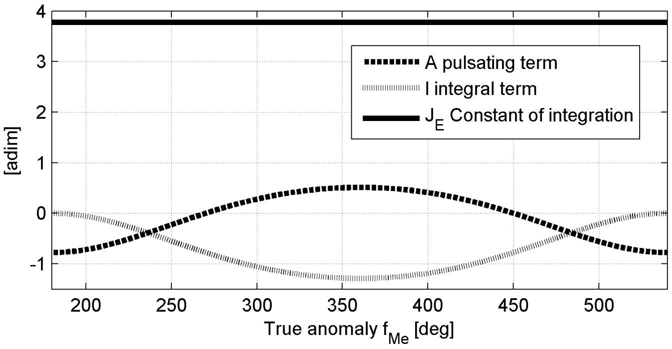

Figure 6.3: The integral term I (numerically computed) and the pulsating term A of the constant of integration J_E for the periodic orbit of Figure 6.2 as function of the true anomaly of Mercury. When summed together, the integral term almost cancel the pulsating term. Neglecting the integral term results in a large artificial pulsation of the constant of integration J_E, hence to the pulsating zero-velocity surfaces.

Figure 6.3 explains this paradox showing that the neglected integral term I (computed numerically) is of the same order of magnitude of the pulsating term A; in fact the two terms almost cancel each other out. This suggests that at least in some cases the pulsating behavior is a spurious consequence introduced by the approximation.

When the third body is at equilibrium , for instance, the zero-velocity surface is the invariant set containing the equilibrium point. At any instant $f$the integral term I and the pulsating term A cancel each other (except for a constant term). By neglecting the integral term, however, the quasi-steady approach creates artificial zero-velocity surfaces which pulsates periodically. This pulsation is an *over-estimation* of either the regions of motion or the forbidden regions. Even if the third body is in equilibrium at $L1$, for instance, we can find forbidden regions that include the current position of the spacecraft $L1$, or regions of motion that open up at $L2$.

6.3.2 Forbidden subregions, subregions of motion and low-velocity subregions

We propose an alternative approach which yields the definition of under-estimated regions of motion and forbidden regions. In between them we define a region which include the zero-velocity surfaces which we call low-velocity region .

First we note that the integral term $I(f; f_0)$ has local minima and maxima at each planet pericenter and apocenter respectively. In fact[3]:

$$\frac{dI}{df} = 0 \rightarrow \bar{f} = n\pi \tag{6.4}$$

and:

$$\left.\frac{d^2 I}{df^2}\right|_{f=n\pi} = (-1)^n k \qquad (k > 0) \tag{6.5}$$

Hence even if the integral term cannot be computed without the knowledge of the full solution $\mathbf{X}(t)$, we can still evaluate its upper and/or lower boundaries for any finite interval of true anomaly.

If the initial condition $\mathbf{X}_0$ is given at $f_0 = 0$, Eq. (6.4) and Eq. (6.5) imply $I(f; f_0) \geq 0$ for all $f \in [-\pi, \pi]$. We can then define the subset

---

[3] Assuming $\left|\frac{d\Omega^*}{df}\right| < \infty$

$$\mathcal{F}_f^* \subset \mathcal{F}_f,\ \mathcal{F}_f^* = \left\{(X,Y,Z)|(2\Omega_C - A - J_E^p) < 0\right\}$$

with $J_E^p = J_E\left(0, \mathbf{X}(0)\right)$. We call the subset $\mathcal{F}_f^*$ forbidden subregion of motion, as it represents an under-estimation of the forbidden region. The forbidden subregions give useful information in the entire interval $[-\pi, \pi]$. Because they shrink and expand as the true anomaly f goes from $-\pi$to 0 and from 0 to π (their boundaries are defined by the same equation of the pulsating curves). We use them to formulate a necessary condition for transfer trajectories in the ER3BP:

Given a set of initial condition $f_0 = 2n\pi; \mathbf{x_0} = \mathbf{X}\left(f_0\right)$*, a transfer trajectory between the primaries cannot occur in the interval* $[2n\pi - \pi, 2n\pi + \pi]$ *if* $L1 \in \mathcal{F}^*_{(2n-1)\pi}$ *and* $L1 \in \mathcal{F}^*_{(2n+1)\pi}$*.*

Similarly, given a set of initial condition $f_0 = \pi; \mathbf{x_0} = \mathbf{X}\left(\pi\right)$, Eq. (6.4) and Eq. (6.5) imply $I(f; f_0) \leq 0$ for all $f \in [0, 2\pi]$. We define the subregions of motion

$$\mathcal{A}_f^* \subset \mathcal{A}_f,\ \mathcal{A}_f^* = \{\mathbf{X}|(2\Omega_C - A - J_E^a) > 0\}$$

with $f \in [0, 2\pi]$ and $J_E^0 = J_E\left(0, \mathbf{X}(0)\right)$.

Finally, if we know the state $\mathbf{X}$ at two consecutive apsidal positions of the primaries we can compute both J_E^a and J_E^p, hence the low-velocity subregions

$$\mathcal{L}_f^* = \left\{(X,Y,Z)|(2\Omega_C - A - J_E^p) > 0, (2\Omega_C - A - J_E^a) < 0\right\}$$

This set is the complement to the subregions of motion and the forbidden subregions, and by definition it includes the zero-velocity surfaces. For true anomaly intervals $[f_L, f_U] \subset [0, 2\pi]$ we can still define low-velocity surfaces, by replacing J_E^p and J_E^a with $J_E^L = J_E(f_L)$ and $J_E^U(f_U)$.

Figure 6.4 show the subregions of motion on the xy plane of a third body in the Earth-Moon ER3BP ($e = 0.054$, $\mu = 0.0123$) in the interval $[0, 2\pi]$. The third-body is on a small quasi-periodic orbit around $L1$. In this case the low-velocity subregions always include the quasi-periodic orbit.

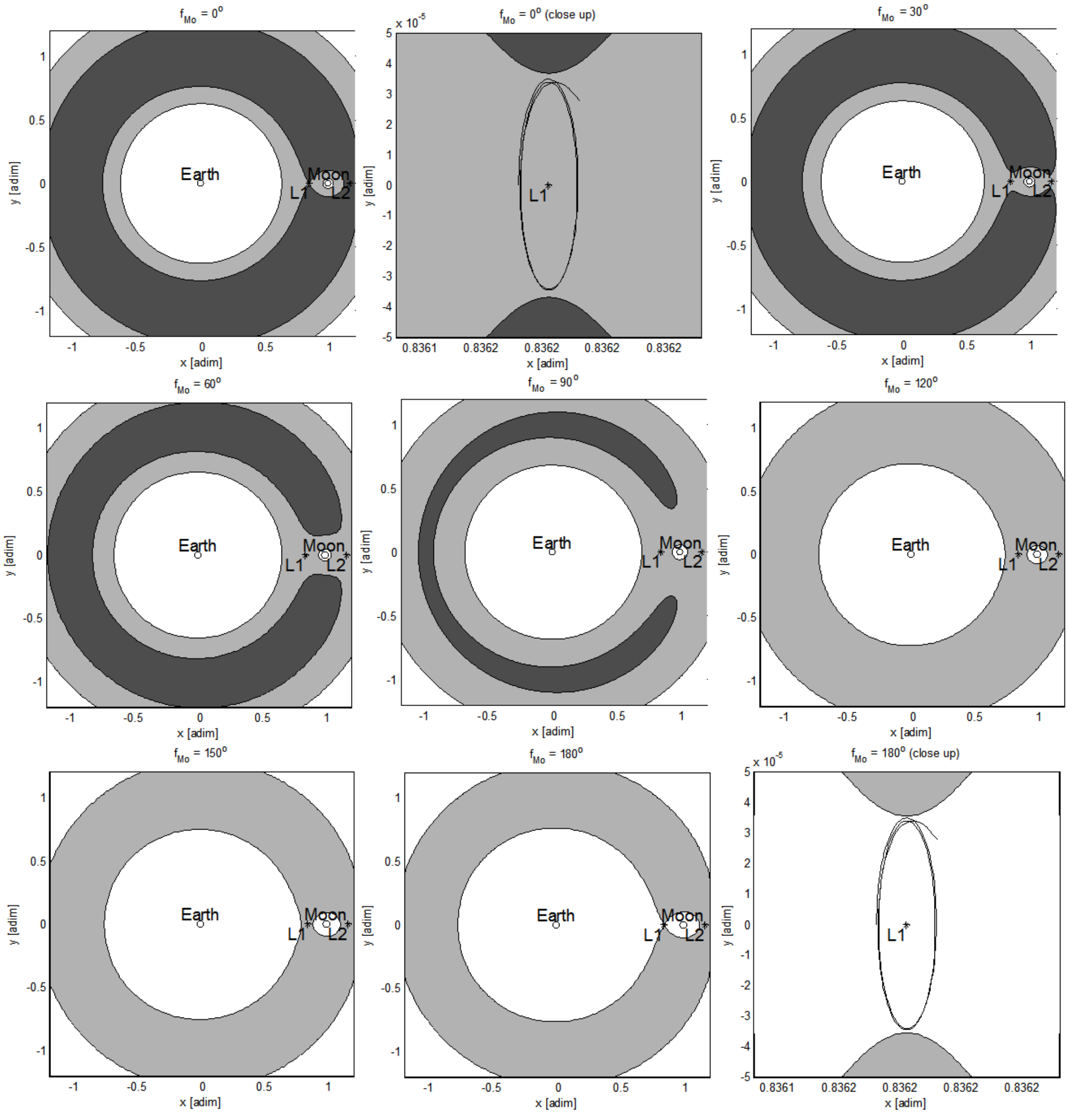

Figure 6.4: Subregions of motion for a third body on a small $L1$ quasi-periodic orbit of the Earth-Moon ER3BP. f_{Mo} is the true anomaly of the Moon. The subregions of motion are plotted each 30^o of true anomaly of Mercury. The white region is the subregion of motion. The dark gray region is the forbidden subregion. The light gray region is the low-velocity region.

6.4 Periodic orbits

In this section we show how to compute periodic orbits in the ER3BP. In particular, we compute and study the stability of some orbits which we call *elliptic halo orbits* since they bifurcate from special halo orbits of the CR3BP. We first introduce the periodic orbits in the ER3BP.

The right hand side of the equations of motion Eq. (6.1) is periodic with period 2π. Thus, periodic solutions of the ER3BP must have principal period $T = 2N\pi$, $N = 1, 2, \ldots$; they are also periodic in the inertial reference frame. In the context of the *planar* ER3BP, Moulton[MBB$^+$20] used these considerations and the symmetry properties of the system Eq. (6.1) to formulate the Strong Periodicity Criterion :

For an orbit to be periodic [in the planar ER3BP] it is sufficient that it has two perpendicular crossing with the syzygy-axis, and that the crossings happen at moments when the two primaries are at an apse, (i.e. , at maximum or minimum elongation, or apoapsis and periapsis).

In the late 1960es Broucke[Bro69] used Moulton's criterion to compute planar orbits in the ER3BP. He chose 150 orbits of the planar CR3BP with period $T = 2N\pi$ as starting points, with $N = 1, 2, 3, 4, 5$, and computed them in the planar ER3BP for different eccentricities using a continuation method. In particular, each of the 150 orbits was continued into two branches of orbits, which he called periapsis orbits and apoapsis orbits, depending on the true anomaly of the primaries at the starting point on the syzygy axis ($f = 0$ or $f = \pi$).

We use a similar approach to compute elliptic halo orbits. We extend Moulton's criterion and Broucke's approach as the elliptic halo orbits are 3D and in general have periods smaller than 2π. First we consider the following symmetries of the system Eq. (6.1):

$$S1 : \left(k\pi + f, X, Y, Z, \dot{X}, \dot{Y}, \dot{Z}\right) \to \left(k\pi - f, X, -Y, -Z, -\dot{X}, \dot{Y}, \dot{Z}\right) \qquad (6.6)$$

$$S2 : \left(k\pi + f, X, Y, Z, \dot{X}, \dot{Y}, \dot{Z}\right) \rightarrow \left(k\pi - f, X, -Y, Z, -\dot{X}, \dot{Y}, -\dot{Z}\right) \tag{6.7}$$

which we use to formulate the Elliptic Periodicity Conditions:

For an orbit to be periodic in the ER3BP, it is sufficient that it has two perpendicular crossing with either the normal plane *(from S1) or the* syzygy axis *(from S2), or both of them, when the primaries are at an apse .*

Second, we choose halo orbits with principal period $T_C = 2r\pi$, where $r = \frac{N}{M}$ is the resonant ratio between the number of the primary revolutions N and number of the third body revolutions M. By assembling M revolutions of a halo orbit, we build an orbit with period $T_E = MT_C = 2N\pi$ which is a solution of Eq. (6.1) for $e = 0$, and which has $2M$ perpendicular crossings with the normal plane (M left X-intercepts and M right X-intercepts).

If the first crossing of the orbit occurs when the primaries are an apse, then the $M + 1$th crossing also occurs when the primaries are at an apse. More precisely, the $M + 1$th crossing occurs $N\pi$ after the first crossing. Such orbit is an elliptic halo orbit for $e = 0$, and satisfies the Elliptic Periodicity Condition as it has two perpendicular crossing with the normal plane when the primaries are at an apse. Next we compute elliptic halo orbits for $e > 0$ using the eccentricity as a continuation parameter and we impose a perpendicular crossing on the 1st and on the $M + 1$th intercepts at fixed times.

Different kinds of elliptic halo orbits can be assembled starting from the same halo orbit in the CR3BP. For instance, if M is odd we can compute periapsis or apoapsis families depending on whether the first crossing occurs at the periapse or apoapse as described by Broucke for $M = 1$[Bro69]. However, if M is even we can continue two new families of orbits, which we call the left and right family, depending on whether the first crossing is a left X-intercept or a right X-intercept.

We apply our approach to two different cases. In the first case, we consider a system with a small mass ratio $\mu \approx 1e - 6$, corresponding to the Mercury-Sun system, and choose as $L1$ halo orbit with $T_C = \frac{4}{5}\pi$, i.e. $N = 2$ and $M = 5$. We build the elliptic halo orbit by assembling five revolutions of the halo orbit ($T_E = 4\pi$), and we compute the periapsis and apoapsis families for eccentricities up to $e \approx 0.02$. Figure 6.5 shows the two families, in both the rotating and inertial reference frames. We also compute an orbit of the pericenter family for $e \approx 0.2$, corresponding to the eccentricity of Mercury's orbit, and compare our solution to one integrated with the full ephemeris model - see Figure 6.1.

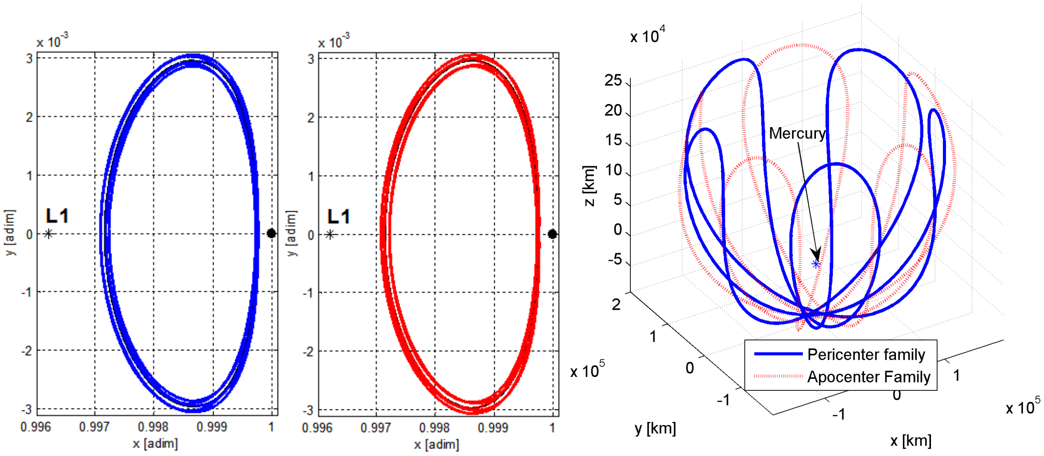

Figure 6.5: Periapsis and apoapsis elliptic halo orbits in the ER3BP ($e = 0.02$) generated from a 2:5 halo orbit in the CR3BP. The first and second figure from the left show the periapsis and apoapsis halo orbits in the rotating reference frame. The last figure shows both orbits in the inertial reference frame.

In the second case, we consider a system with a relatively high mass ratio: $\mu = 0.012$, similar to the Earth-Moon system, and choose a halo orbit orbit with period $T_C = \pi$, i.e. $N = 1$ and $M = 2$. We build the elliptic halo orbit by assembling two revolutions of the halo orbit, and we compute the left and the right elliptic halo orbits for eccentricity up to $e = 0.3$. Note that when continuing the orbit from $e = 0$ to $e > 0$, the principal period of the elliptic halo orbits changes from T_C to $T_E = 2T_C$. Also one single halo orbit generates two new elliptic halo orbits. Those elements suggest that a period doubling bifurcation occurs at $e = 0$. In the next section we show that the stability properties of the left and right elliptic halo orbits differ from those of the originating halo orbit. Figure

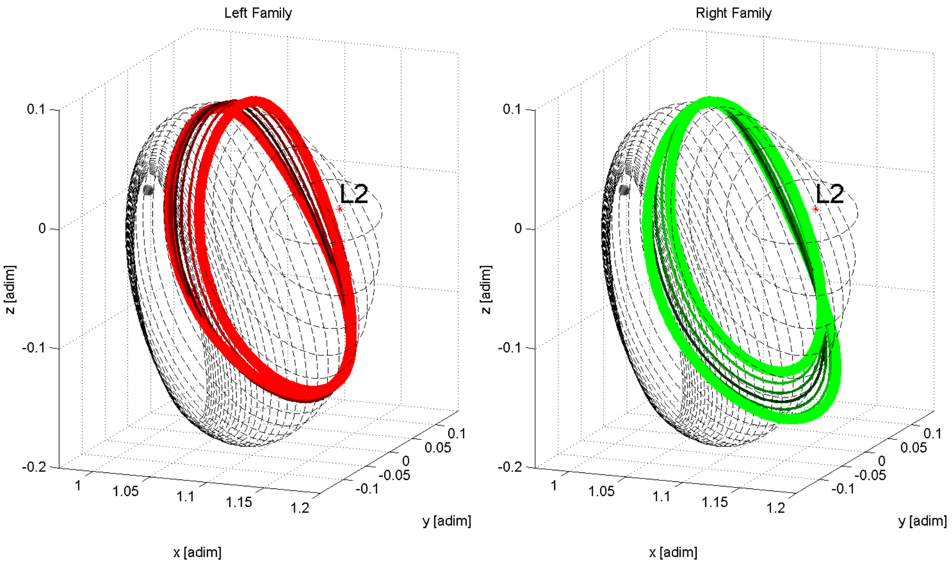

Figure 6.6: Left and Right elliptic halo orbits in the ER3BP ($0 < e < 0.3$, $\mu \approx 0.0123$). The dash lines are the L2 halo orbits in the CR3BP. The bold solid line is the elliptic halo for $e = 0.3$. On the Left: 'Left' family that bifurcates from the L2 halo in the pulsating reference frame. On the Right: 'Right' family that bifurcates from the L2 halo in the pulsating reference frame.

6.6 shows the left and right families together with the family of halo orbits at $e = 0$. Each color corresponds to an elliptic halo orbit computed with a distinct eccentricity.

6.4.1 Stability

In order to study the linear stability of the elliptic halo orbits, we briefly recall some important results of Floquet's theory. Consider a system of equations:

$$\dot{\mathbf{Y}}(t) = A(t)\mathbf{Y}(t) \tag{6.8}$$

where $A(t)$ is periodic with period T, and $\mathbf{Y} \in \mathbb{R}^n$. Also consider a fundamental matrix $\psi(t)$ for the system Eq. (6.8), and the matrix $E = \psi(0)^{-1}\psi(T)$ [4]. If E has n distinct eigenvalues λ_i, then there are n solutions $\mathbf{Y}_i(t) = \mathbf{q}_i(t)e^{\rho_i(t+T)}$, where $\mathbf{q}_i(t)$ are periodic function with period T, and ρ_i are the characteristic exponents associated to

---

[4] Assume $t_0 = 0$

λ_i. Also, it can be shown that $\mathbf{Y}_i(t+T) = \lambda_i \mathbf{Y}_i(t)$, and the eigenvalues λ_i determine the stability properties of the system Eq. (6.8).

We can now apply Floquet's theory to the ER3BP. The linearized first order system of ODEs is:

$$\delta\dot{\mathbf{X}}(f) = A(f)\delta\mathbf{X}(f)$$

where

$$A(f) = \begin{bmatrix} 0 & I \\ \frac{\partial^2 \omega_E}{\partial \mathbf{r}^2} & 2J \end{bmatrix}$$

and:

$$\begin{aligned} \frac{\partial^2 \omega_E}{\partial \mathbf{r}^2} &= \frac{\partial^2 \Omega_C}{\partial \mathbf{r}^2} - \frac{e\cos f}{1+e\cos f}\frac{\partial^2 \Omega^*}{\partial \mathbf{r}^2} = \\ &= \frac{3\frac{1-\mu}{r_1^3}\hat{\mathbf{r}}_\mathbf{1} \otimes \hat{\mathbf{r}}_\mathbf{1} + 3\frac{\mu}{r_2^3}\hat{\mathbf{r}}_\mathbf{2} \otimes \hat{\mathbf{r}}_\mathbf{2} + (1 - \frac{1-\mu}{r_1^3} - \frac{\mu}{r_2^3})\underline{\underline{I}}}{1+e\cos f} - \mathbf{e_Z} \otimes \mathbf{e_Z} \end{aligned}$$

The state transition matrix $\phi(f)$ is solution of the system:

$$\dot{\phi}(f) = A(f)\phi(f) \quad \phi(f_0) = I$$

In the ER3BP $\phi(f)$ is in fact a fundamental matrix $\psi(t)$ for the system, and the matrix E is the monodromy matrix $M = \phi(T)$ and can be computed by integrating $\phi(f)$ or by using approximation methods [GM07]. As mentioned in the previous section, the eigenvalues of the monodromy matrix M still come in reciprocal pairs, but there are no more unitary eigenvalues[BLB76] associated to perturbation $\delta\mathbf{X}$ tangent to the trajectory. In the case of the left elliptic halo orbits of Figure 6.6 on the left, the eigenvalues move on the unit circle, hinting at the existence of quasi-periodic orbits. In the case of the right elliptic halo orbits of Figure 6.6 on the right, the eigenvalues move on the real axis generating new stable and unstable manifolds; the stability properties of the halo orbits changes when the eccentricity is $e \neq 0$.

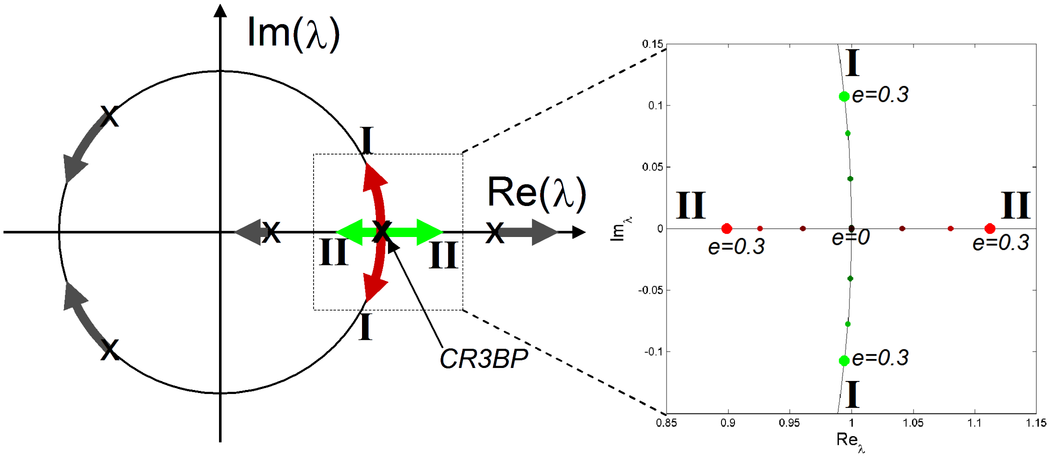

Figure 6.7: The real unitary eigenvalues of the halo orbit change as the eccentricity changes. A pair of complex conjugated eigenvalues on the unit circle is generated in the case of the left elliptic halo orbits (branches I), while a stable/unstable pair of eigenvalues is generated in the case of the elliptic right halo orbits (branches II). The left picture is schematic, while the right is the result of the numeric computation.

Chapter 7

The capture in the ER3BP

This chapter present two different approaches to solve the capture problem. In particular, we used the mission constraint given by the BepiColombo mission to Mercury[GdPJ08]. Although the models and results are mission specific, the approaches can be applied to any missions once the main constraints on the science orbits are known.

The first approach to solve the capture was used in the original design of the BepiColombo nominal trajectory, and consist of exploring the solution space by varying selected orbital elements of the spacecraft before orbit insertion. The BepiColombo gravitational capture provides several recovery opportunities at nominal conditions and orbit insertion. We extend this approach with the software tool GraCE.

The second approach consists of choosing a suitable quasi-periodic orbits in the elliptic, restricted 3-body problem, and compute the stable manifold onto it. We show that the BepiColombo trajectory near Mercury follows the invariant manifolds to its final capture.

7.1 The BepiColombo gravitational capture

BepiColombo is the ESA mission to Mercury. Two spacecraft will be launched jointly in 2013 and will reach their destination in 2019. The nearly 6-year long transfer includes several gravity assists and SEP (solar electric propulsion) thrust arcs [GdPJ08].At Mercury a chemical burn (Mercury Orbit Insertion OI) inserts the spacecraft into a 400km x 12000 km polar orbit, with the line of apsides almost aligned with the Sun-Mercury eccentricity vector.

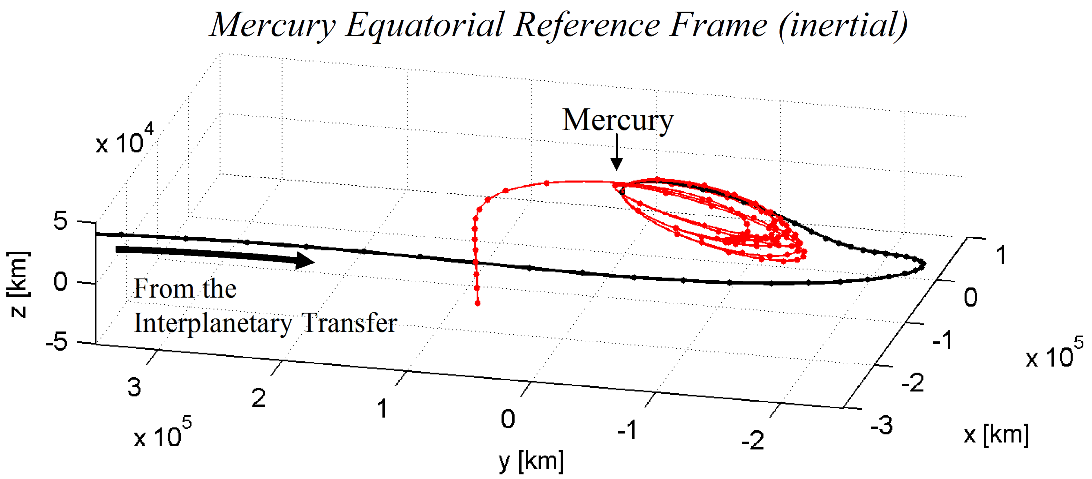

Figure 7.1: BepiColombo Gravitational Capture in the inertial frame. Mercury is at the origin, the z-axis is perpendicular to Mercury equator. In the 2012 baseline BepiColombo approaches Mercury from the negative x-axis. The dots are points along the trajectory one day apart computed in the real ephemeris model. The solid line is the trajectory computed using the equations of the elliptic restricted three-body problem. The Gravitation Capture trajectory has no deterministic maneuvers: in case of failure of the Mercury Orbit Insertion (OI), there are three backup OIs before the spacecraft eventually leaves Mercury sphere of influence.

To avoid a potential single point failure of a classical hyperbolic approach, an arrival scenario is implemented where the gravity of the Sun is exploited to weakly capture the spacecraft. This technique is called gravitational capture.

Gravitational capture trajectories can be designed by exploring the solution space spanned by all the admissible incoming trajectories (i.e. consistent with the mission constraint) and assuming a failure of the orbit insertion. In the case of the BepiColombo mission, such solution space is bounded and only two-dimensional. The gravitational capture trajectory for the 2012 launch option[1] in Figure 1 was designed with this simple

---

[1] In the last year the mission was redesigned and approved for launch in 2013; the gravitational capture trajectories under consideration are all very similar to the 2012 baseline.

approach, which we extend and implement in the software tool GraCE (Gravitation Capture Explorer) presented in the next section.

Yet gravitational capture trajectories are better understood in the frame of the restricted three-body problem. Figure 2 shows the gravitational capture in the pulsating reference frame, where Mercury and the Sun are at fixed position on the X-axis, and the Z-axis is perpendicular to Mercury's orbital plane. Part of the trajectory is almost symmetric to the XZ plane, and crosses the syzygy axis when Mercury is at apohelium. This suggests that the elliptic restricted three-body problem ER3BP can give valuable insight on such solutions, and possibly lead to alternative design techniques.

In fact, the simple approach implemented in GRaCE fails for most of the mission feasibility study, where the target trajectory may not be completely fixed and the solution space becomes seven-dimensional, too computationally expensive to explore, and too difficult to visualize.

In this chapter we show that BepiColombo gravitational capture trajectories shadow the stable and unstable manifolds of a special quasi-periodic orbit in the ER3BP, suggesting that future design should make use of these tools. Ryan and Lam [RL07] designed gravitational capture trajectories to Europa using unstable periodic orbits and their stable manifolds in the CR3BP, and they implemented a technique to reproduce the trajectory in the full ephemeris model. In this paper trajectories in the Sun-Mercury ER3BP are easily reproduced in the full ephemeris model with no corrections on the initial conditions (see Figure 1).

7.2 GraCE – Exploring Gravitational Capture Trajectories

When an interplanetary spacecraft approaches its target planet, an Orbit Insertion maneuvers (OI) inserts the spacecraft into a closed orbit. If the approach trajectory is hyperbolic, a failure of the orbit insertion maneuver results in an inadverted gravity

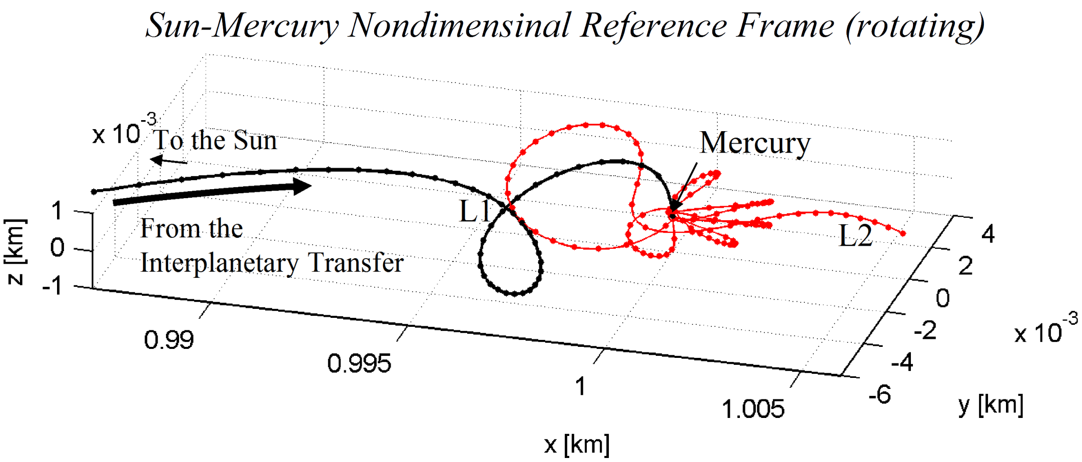

Figure 7.2: Fig. 2 BepiColombo Gravitational Capture in the pulsating reference frame. The Sun-Mercury barycenter is at the origin (not in the plot); Mercury and the Sun are at fixed position on the X-axis at unit distance. The Z-axis is perpendicular to the orbital plane of Mercury. In this reference frame the Lagrangian points are at fixed location. In the 2012 baseline BepiColombo approaches Mercury from the negative X-axis. The dots are points along the trajectory one day apart computed in the real ephemeris model. The solid line is the trajectory computed using the equations of the elliptic restricted three-body problem.

assist and often the mission is lost; in such cases the orbit insertion maneuvers is a single point of failure.

The gravitation capture is a mechanism by which the spacecraft attains low relative velocity with respect to the planet or moon and even can orbit around it temporarily. Thus gravitational capture trajectories offer several orbit insertion opportunities in case of failure of the nominal OI. In this work, gravitational capture trajectories are designed to maximize the number of backup OIs with almost no deterministic maneuvers in between them while satisfying the mission constraints.

If the target orbit around the planet is completely fixed by mission constraints, gravitational capture trajectories can be found by simply varying the capture time and speed of the spacecraft right before OI. The first gravitational capture trajectory for BepiColombo was thus designed by exploring the solution space [JCGK04]. Initial conditions were propagated backward and forward in a full ephemeris model with three different initial speeds and with the initial times varying on a half-day grid for a revolution of Mercury. Among the computed solutions [CJCVD04], the trajectory selected for the 2012 baseline (shown in Figure 1 and 2) is a good compromise of number of recovery opportunities at allowed capture times, deterministic ΔV for the trajectory correction maneuvers and safe periherm passages. In case of failure of the orbit insertion there are three more MOI opportunities at almost nominal condition before the spacecraft eventually leaves Mercury's sphere of influence.

We extend this approach in GraCE (Gravitational Capture Explorer), a software tool developed in Matlab which computes the entire solution space in ephemeris model and allows the user to filter and explore it through a GUI. Given a Δv allocated for trajectory correction maneuvers, GraCE shows level sets of feasible trajectories for each number of the backup opportunities. GraCE also shows all the main parameters for the design (time and osculating parameters of each periherm passages, recovery Δv for each opportunity) for each trajectory. In Figure 3 we use GraCE's GUI to visualize the solution space for the 2013 launch option of BepiColombo.

This way of computing gravitational capture trajectories quickly provides a baseline trajectory to the mission team. Yet a full exploration of the solutions space would become impractical if only one additional parameter is allowed to vary. Also, the current approach does not provide any insight on the families of "good" solutions which usually cross the Sun-Mercury syzygy line in opposition when Mercury is at apohelium. Also, many solutions seem to loop around the Lagrangian points, when plotted in the pulsating reference frame.

In what follows we show that gravitational capture trajectories like the one in Figure 2 are better understood in the frame of the elliptic restricted three-body problem (ER3BP), which we briefly introduce in the next section.

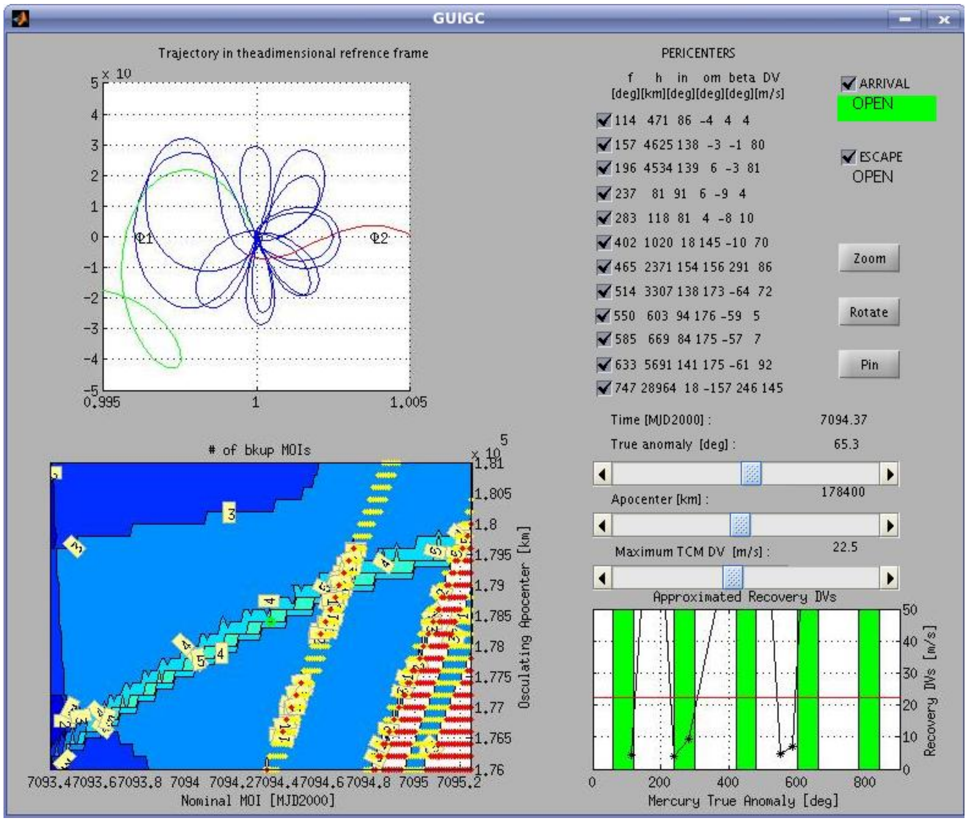

PERICENTERS

	f [deg]	h [km]	in [deg]	om [deg]	beta [deg]	DV [m/s]
☑	114	471	86	-4	4	4
☑	157	4625	138	-3	-1	80
☑	196	4534	139	6	-3	81
☑	237	81	91	6	-9	4
☑	283	118	81	4	-8	10
☑	402	1020	18	145	-10	70
☑	465	2371	154	156	291	86
☑	514	3307	138	173	-64	72
☑	550	603	94	176	-59	5
☑	585	669	84	175	-57	7
☑	633	5691	141	175	-61	92
☑	747	28964	18	-157	246	145

☑ ARRIVAL OPEN

☑ ESCAPE OPEN

Time [MJD2000] : 7094.37

True anomaly [deg] : 65.3

Apocenter [km] : 178400

Maximum TCM DV [m/s] : 22.5

Figure 7.3: Fig. 3 GraCE explores gravitational capture trajectories for the 2013 launch option of BepiColombo. On the bottom left: the solution space computed by GraCE; the x-axis is the nominal arrival day, the y-axis is the osculating apoherm before OI. For the selected recovery ΔV of 22.5 m/s, the contour lines show the number of recovery opportunities before BepiColombo eventually leaves Mercury's sphere of influence or collides with the planet. Not that sometime the backward propagation results in a collision trajectory (red stars in the solution space). We call these solutions unfeasible as they cannot match the interplanetary transfer.

7.3 BepiColombo and unstable orbits in the ER3BP

We first recall some facts form the ER3BP. The system of equations Eq.6.1 define a non-autonomous system, periodic with period 2π. Thus orbits of the ER3BP have principal period $2k\pi$ (k integer), and are periodic both in the pulsating and in the rotating reference frame [MBB$^+$20, Bro69].

In the previous chapter we showed that almost all (a countable infinity of an uncountable set) periodic orbits of the CR3BP can generate branches of periodic orbits in the ER3BP; in fact, we showed that periodic orbits in the CR3BP with period $2\pi n/m$ can be continued in new periodic orbits of the ER3BP with principal period $2\pi n$. As the periodic orbits in the ER3BP close only after several revolutions of the primaries, most of the orbits in the ER3BP will appear to be quasi-periodic in practical application. For this reason we compute two quasi-periodic orbits and portions of their manifolds in the ER3BP, and compare such trajectories with the BepiColombo gravitational capture.

Because the system is non-autonomous, we compute approximated invariant manifolds of the augmented system by integrating trajectories departing from the quasi-periodic orbits. We choose the initial perturbation aligned to the maximum stretching direction of the deformation tensor, computed for short time intervals.

First we compute periodic and quasi-periodic orbits around the libration points. We expect gravitational capture trajectories to follow the stable manifolds of such orbits. In particular we compute a Lissajous orbit around L1 with amplitude close to 4e-3 (by comparison with the BepiColombo gravitational capture). Figure 5 (top left) shows the Lissajous orbit and a single trajectory on its stable manifold and a single trajectory on its unstable manifold.

We then look at quasi-periodic around Mercury. We compute orbits with special symmetric features, allowing for several recovery options at nominal conditions. In particular, we use the symmetry in Eq.(6.6) and we require the quasi-periodic orbit to cross the syzygy axis perpendicularly when Mercury is at apohelium. Figure 5 (top-right) shows the quasi-periodic orbit with trajectories from the stable and unstable manifolds which shadow the gravitational capture trajectory. Note that the orbits from the manifolds are also symmetric.

Finally we compare the unstable orbits and their manifolds to the BepiColombo gravitational capture in Figure 5 (bottom). Coming from the interplanetary transfer,

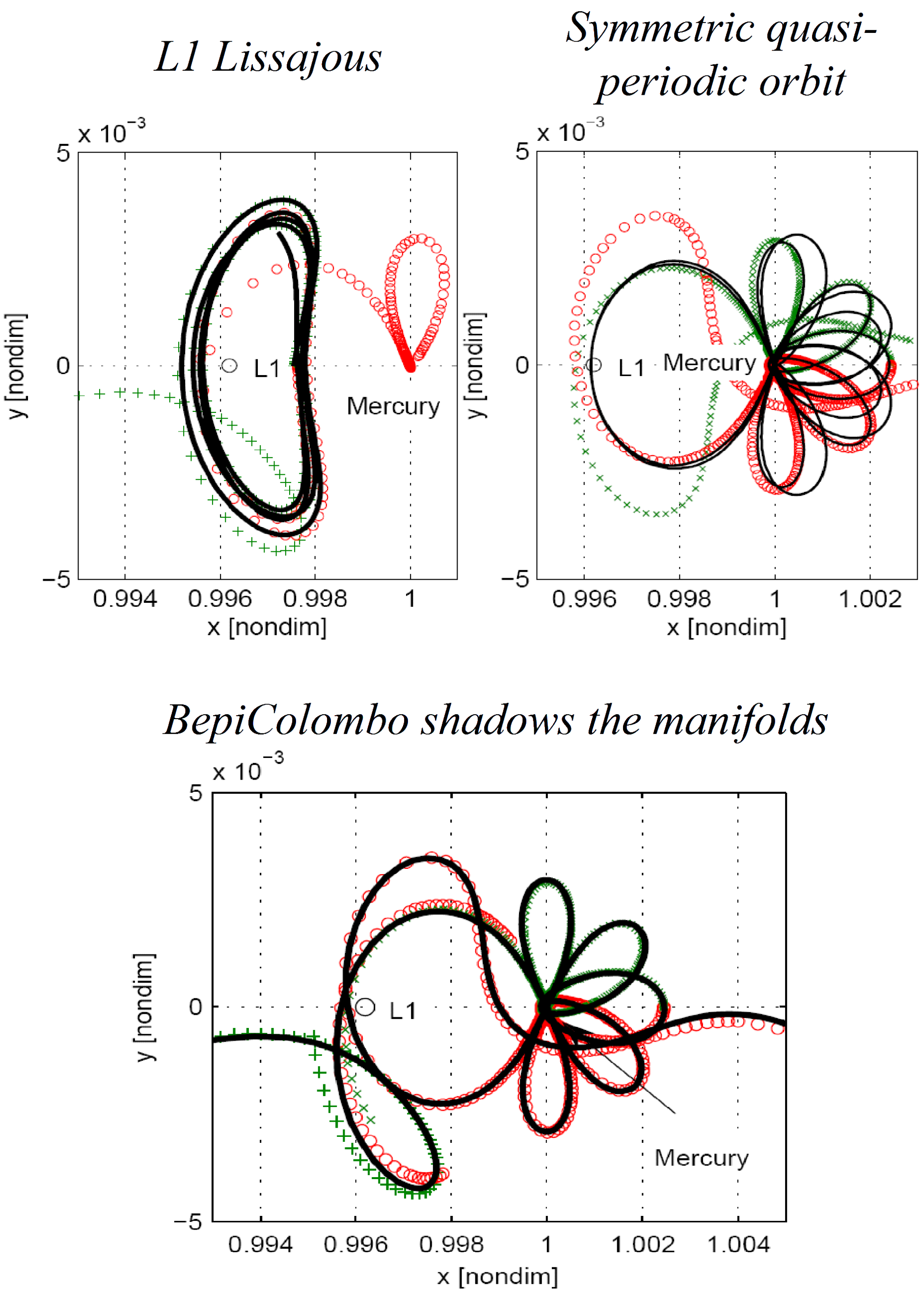

Figure 7.4: Fig. 5 Trajectories in the pulsating reference frame (projection onto the xy plane). Left: The Lissajous orbit is plotted together with one trajectory of the stable manifold (star) and one trajectory of the unstable manifold (circle). Center: The symmetric quasi-periodic orbit around Mercury is plotted with one trajectory of the stable manifold (star) and one trajectory of the unstable manifold (circle). Note the manifolds are also symmetric. Right: The BepiColombo gravitational capture (solid line) shadows the stable and unstable manifolds.

the spacecraft follows the stable manifold of the Lissajous and approaches L1. After less then one revolution around the libration point, the trajectory shadows a heteroclinic connection between the Lissajous orbit and the quasi-periodic orbit around Mercury. In case the first MOI fails, the spacecraft continues to shadow the symmetric orbit and will eventually escape Mercury's attraction along the unstable manifold after several MOI opportunities at nominal condition.

Figure 6 shows all the trajectories generated by perturbing the quasi-periodic orbit (thick solid line) together with the BepiColombo gravitational capture trajectory (thick dashed line).

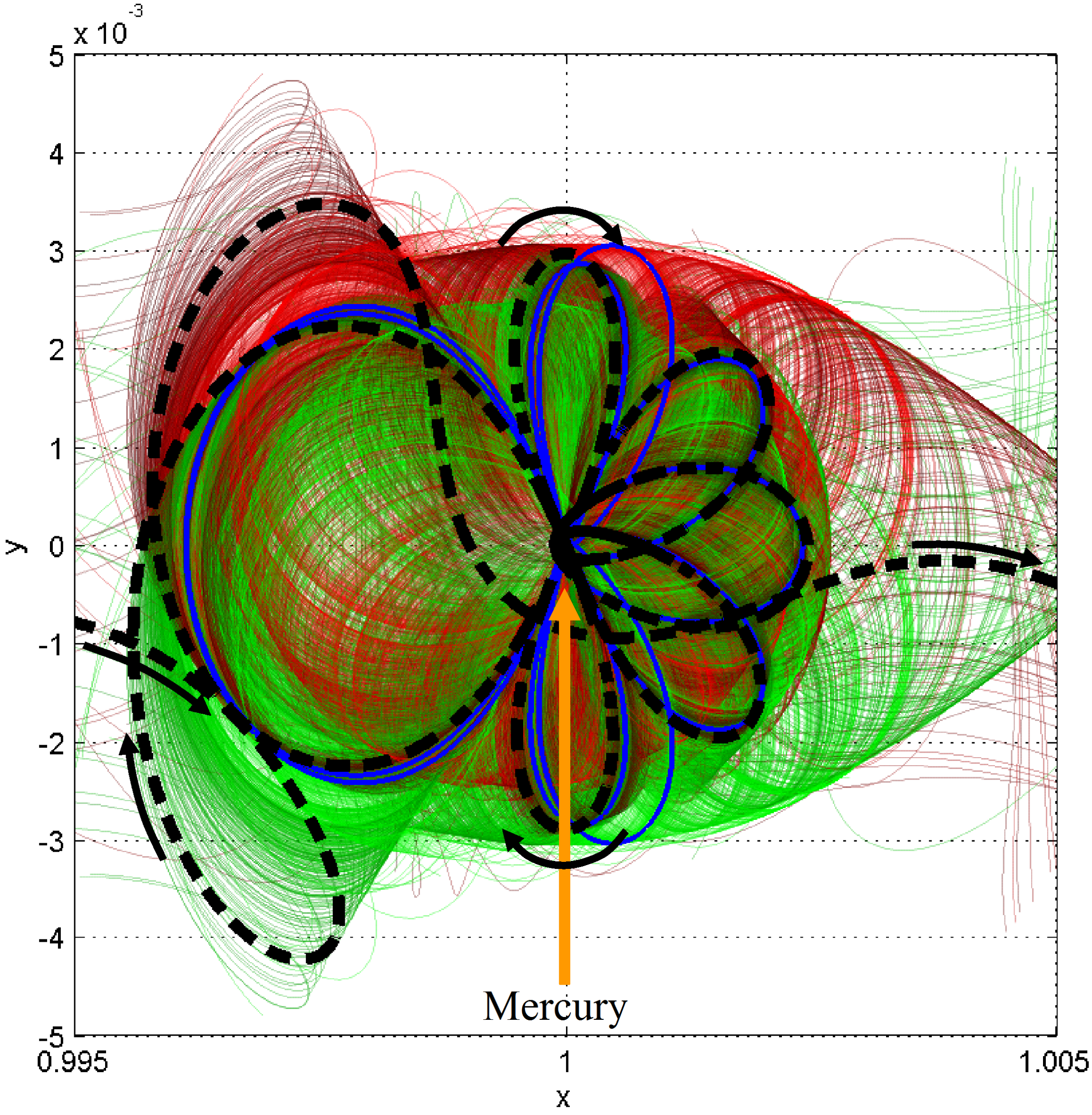

Figure 7.5: Fig. 6 The BepiColombo trajectory (dashed line) shadows the manifolds of the quasi-periodic orbit around Mercury (solid thick line).

Chapter 8

Conclusions

In this report we present new techniques for the design of trajectories touring moon systems.

In chapter 3 we derive new formulae for the v_∞-leveraging transfer (VILT). We use these formulae to show that the VILT is only efficient when the v_∞ is larger than a minimum value. We also use the formulae to build a new graphical tool, the leveraging graph, which gives insight on the VILT problem and allows for a fast, intuitive, preliminary design of VILTs. The analysis of the VILT efficiency reveals that the total Δv of a sequence of VILTs decreases when implementing high altitude gravity assists. This suggests a simple way to compute the theoretical minimum Δv to transfer a spacecraft between arbitrary initial conditions using sequences of VILTs. The minimum Δv is found by solving a simple quadrature formula. We use this formula to compute the minimum Δvs for different transfers between the Jupiter or Saturn moons. This new design capability is the first important result of this work. The leveraging graphs and associated formulae provide for a fast, accurate method for estimating Δvs on the complex endgame and general multi-moon tour problems.

In chapter 4 we present a new graphic technique, the Tisserand-Poincaré (T-P) graph, which is the second important result of this work. We use the T-P graph to understand and design low-cost endgames and transfers - in the context of both linked-conics and patched three body systems. While the T-P graph can be used like the Tisserand graph, it extends beyond the limits of the linked-conic approach into the domain of the patched circular restricted 3-body problem (CR3BP) showing that low-energy ballistic orbits around the moons are energetically connected. The T-P graph also provides target points and a simple rationale for the design of such transfers.

With a very simple search, we designed a transfer between a circular orbit at Europa and a circular orbit at Ganymede which requires only 1.25 km/s, almost 500 m/s less than the theoretical minimum cost achieved by v_∞-leveraging maneuvers (VILT) transfers, and almost 1 km/s less that the direct Hohmann transfer. With the same approach we found a transfer between a halo orbit around L1 of the Ganymede-Jupiter system and a halo orbit around L2 of the Europa-Jupiter system. The transfer is quasi-ballistic and lasts 300 days, and can be shortened by two months for an additional 50 m/s, or by three months by an additional 100 m/s.

In chapter 5 we study the solution space of the general (non-tangent) VILT problem and demonstrate that the space is almost flat for a proper choice of coordinates. We derive an approximation to the solution space which allows for fast computation of the transfers. Using the approximation and the Tisserand graphs, we introduce a fast graphical design method for multiple-VILT transfers, which is the third important result of this work. Using the new method we quickly compute a trajectory from a highly eccentric orbit at Saturn to a 200 km orbit at Encaladus. The trajectory includes 52 gravity assists at Titan, Rhea, Dione, Tethys and Enceladus. The time of flight is 2.7 years, and the total Δv is only 445 m/s, including the Enceladus orbit insertion. For comparison, the Enceladus orbit insertion from a Titan-Enceladus Hohmann transfer is almost 4 km/s. The low Δv and flight time solutions presented in this study embolden the already strong arguments to send an orbiter to Enceladus. The new method and demonstrated results generally apply to any mission that tours and ultimately orbits small mass moons. This class of high-science-value missions was previously considered impractical due to flight time and Δv constraints.

In chapter 6 we define regions of motion and periodic orbits in the elliptic, restricted three-body problem (ER3BP). The Hill's zero-velocity surfaces in the CR3BP are replaced by the low-velocity regions, which divides the subregions of motion from the forbidden subregions. Periodic trajectories are computed using a continuation method, starting with orbits in the CR3BP with period synchronous to the period of the primaries. We show that different branches of periodic orbits bifurcates in the ER3BP and that the new branches have different linear stability properties, which is the fourth important result of this work.

In chapter 7 we study the capture problem. We first extend the method used for the BepiColombo capture at Mercury, and develop a software tool to explore the solution space. We then reproduce the nominal trajectory in the elliptic, restricted three body problem, showing that it follows the stable and unstable manifolds of quasi-periodic orbits. In particular, the manifolds of a symmetric quasi-periodic orbit around Mercury play a key role as their symmetry properties provide several recovery opportunities to the mission. This last important result that capture trajectories can also be computed exploiting the symmetries of the elliptic, restricted, three-body problem.

Bibliography

[AMR88] R. Abraham, Jerrold E. Marsden, and Tudor S. Ratiu. *Manifold, Tensor, Analysis, and Applications*, pages 107–108 and 174–175. Springer, 1988.

[And05] Rodney L. Anderson. *Low Thrust Trajectory Design for Resonant Flybys and Captures Using Invariant Manifolds*. PhD thesis, University of Colorado at Boulder, 2005.

[BB79] J. V. Breakwell and J. V. Brown. The 'Halo' family of 3-dimensional periodic orbits in the Earth-Moon restricted 3-body problem. *Celestial Mechanics*, 20:389–404, November 1979.

[BdPC] Arnaud Boutonnet, Paolo de Pascale, and Elisabet Canalias. Design of the Laplace mission. Paper IAC-08-C1.6, 59th International Astronautical Congress, Glasgow, Scottland, 2008.

[BLB76] Roger Broucke, H. Lass, and D. Boggs. A note on the solution of the variational equations of a class of dynamical system. *Celestial Mechanics*, 14:383–392, 1976.

[BR09] Adam T. Brinkerhoff and Ryan P. Russell. Pathfinding and v-infinity leveraging for planetary moon tour missions. In *Proceedings of the AAS/AIAA Space Flight Mechanics Meeting, Savannah, GA*, Feb 2009. Paper AAS 09-222.

[Bro69] Roger Broucke. Stability of periodic orbit in the elliptic, restricted, three-body problem. *AIAA Journal*, 7:1003–1009, 1969.

[CJCVD04] Stefano Campagnola, Ruediger Jehn, and Carlos Corral Van Damme. Design of lunar gravity-assist for the BepiColombo mission to Mercury. In *(AAS 04-130), Advances in the Astronautical Sciences, Vol. 119, pp. 427-442*, 2004.

[CL08] Stefano Campagnola and Martin W. Lo. BepiColombo gravitational capture and the elliptic, restricted three-body problem. *Proceedings in Applied Mathematics and Mechanics*, 7(1):1030905 – 1030906, 2008. Published Online: Aug 6 2008 7:16AM. doi: 10.1002/pamm.200700330.

[CLN08] Stefano Campagnola, Martin W. Lo, and Paul Newton. Subregions of motion and elliptic Halo orbits in the elliptic restricted three-body problem,. In *Advances in the Astronautical Sciences*, volume 130, Part II, pages 1541–1556. Univelt, San Diego, 2008. also AAS Paper 08-200.

[Con68] C. C. Conley. Low energy transit orbits in the restricted three-body problem. *Journal on Applied Mathematics*, 16:732–746, 1968.

[CR10a] Stefano Campagnola and Ryan P. Russell. Endgame problem part 1: V-infinity leveraging technique and leveraging graph. *Journal of Guidance, Control, and Dynamics.*, 33(2):463–475, Mar/Apr 2010.

[CR10b] Stefano Campagnola and Ryan P. Russell. Endgame problem part 2: Multibody technique and T-P graph. *Journal of Guidance, Control, and Dynamics.*, 33(2):476–486, Mar/Apr 2010.

[CSR10] Stefano Campagnola, Nathan J. Strange, and Ryan P. Russell. A fast tour design method using non-tangent, v-infinity leveraging transfers. In *Proceedings of the AAS/AIAA Space Flight Mechanics Meeting, San Diego, GA*, Feb 2010. Paper AAS 10-164. Submitted to Celestial Mechanics and Dynamical Astronomy.

[DKK91] Eusebius J. Doedel, Herbert B. Keller, and Jean Pierre Kernévez. Numerical analysis and control of bifurcation problems: (i) bifurcation in finite dimension. *International Journal of Bifurcation and Chaos*, 1(3):493–520, 1991.

[DRP$^+$07] G. W. Deodel, V. A. Romanov, R. C. Paffenroth, H. B. Keller, D. J. Dichmann, J. Galán-Vioque, and A. Vanderbauwhede. Elemental periodic orbits associated with the libration points in the circular restricted 3-body problem. *International Journal of Bifurcation and Chaos in Applied Sciences and Engineering*, 17(8):2625–2678, 2007.

[GdPJ08] Daniel Garcia, Paolo de Pascale, and Ruediger Jehn. BepiColombo cornerstone consolidated report on mission analysis (CReMA). Technical report, ESOC/ESA, Darmstadt, 2008.

[Geh09] Martin Gehler. On transport and collision of near Earth objects using restricted dynamical systems; diplomarbeit (diploma thesis - in preparation). Technical report, Institute of Aeronautics and Astronautics, RWTH Aachen University, 2009.

[GGH98] Troy D. Goodson, Donald L. Gray, and Yungsun Hahn. Cassini maneuver experience: Launch and early cruise. In *AIAA Guidance, Navigation, & Control Conference, Boston, MA*, Aug. 1998. AIAA Paper 98-4224.

[GM07] Pini Gurfil and Dani Meltzer. Semi-analytical method for calculation the elliptic restricted three-body problem monodromy matrix. *Journal of Guidance*, 30:266–271, 2007.

[GMCM09] Evan S. Gawlik, Jerrold E. Marsden, Stefano Campagnola, and Ashley Moore. Invariant manifolds, discrete mechanics, and trajectory design for a mission to Titan. In *Proceedings of the AAS/AIAA Space Flight Mechanics Meeting, Savannah, GA*, Feb 2009. Paper AAS 09-226.

[Góm79] G. Gómez. Effect of mass-parameter on the periodic orbits of the restricted problem of three bodies. In *Instabilities in dynamical systems*, pages 285–286, 1979.

[GR09] Piyush Grover and Shane D. Ross. Designing trajectories in a planet-Moon environment using the controlled Keplerian map. *Journal of Guidance, Control, and Dynamics*, 32(2):437–444, 2009. doi:10.2514/1.38320.

[Hil78] G. W. Hill. Researches in the lunar theory. *American Journal of Mathematics*, 1(1,2):5–26, 129–147, 245–260, 1878.

[Hol75] G.R. Hollenbeck. New flight techniques for outer planet missions. In *AAS Microfishe series*, volume 26, 1975. Supplement to the Advances in the Astronautical Sciences, Vol. 33, Univelt, San diego, also AAS Paper 75-087.

[How84] Kathleen C. Howell. Three-dimensional, periodic, 'Halo' orbits. *Celestial Mechanics*, 32:53–71, 1984.

[Jac36] Carl Gustav Jacob Jacobi. Sur le movement d'un point et sur un cas particulier du probleme des trois corps. In *Comptes Rendus de l'Académie des Sciences de Paris*, volume 3, pages 59–61. 1836.

[JBC05] Guy Janin, Arnaud Boutonnet, and Stefano Campagnola. Solar orbiter mission analysis. Technical Report WP 481, ESA, European Operation Center, Darmstadt, Germany, March 2005.

[JCGK04] Ruediger Jehn, Stefano Campagnola, D. Garcia, and Steven Kemble. Low-thrust approach and gravitational capture at Mercury. In *ESA special pubblication for the 18th International Symposium on Space Flight Dynamics*, volume 548, page 487. ESA Publications Division, The Netherlands, 2004.

[JD99] Jennie R. Johannesen and Louis A. D'Amario. Europa orbiter mission trajectory design. In *Advances in the Astronautical Sciences*, volume 103, part III, pages 895–908. Univelt, San Diego, 1999. also AAS Paper 99-360.

[KCC04] Michael Kahn, Stefano Campagnola, and Michael Croon. End-to-end mission analysis for a low-cost, two-spacecraft mission to Europa. In *Advances in Astronautical Sciences*, volume 119, pages 463–472. Univelt, San Diego, 2004. also Paper AAS-132.

[KJT08] Theresa D. Kowalkowski, Jennie R. Johannesen, and Lam Try. Launch period development for the Juno mission to Jupiter. In *AIAA/AAS Astrodynamics Specialist Conference and Exhibit, Honolulu, Hawaii*, 2008. Paper AIAA-2008-7369.

[KLMR00] W. S. Koon, M. W. Lo, J. E. Marsden, and S. D. Ross. Heteroclinic connections between periodic orbits and resonance transitions in celestial mechanics. *Chaos*, 10:427–469, 200.

[Lan00] Yves Langevin. Chemical and solar electric propulsion option for a cornerstone mission to Mercury. *Acta Astronautica*, 47(2-9):443–452, 2000.

[LD60] A. H. Land and A. G. Doig. An automatic method of solving discrete programming problems. *Econometrica*, 28(3):497–520, Jul 1960.

[LPS98] A.V Labunsky, O.V. Papkov, and K.G. Sukhanov. *Multiple Gravity Assist Interplanetary Trajectories*, pages 33–68. Earth Space Institute Book Series, Gordon and Breach Publishers, London, 1998.

[MBB$^+$20] F. R. Moulton, D. Buchanan, T. Buck, F. L. Griffin, W. R. Longley, and W. D. MacMillan. *Periodic Orbits*. Washington, Carnegie institution of Washington, 1920.

[MD00] Carl D. Murray and Stanley F. Dermott. *Solar System Dynamics*, pages 456–467. Cambridge University Press, February 2000.

[MDF$^+$06] James V. McAdams, David W. Dunham, Robert W. Farquhar, Anthony H. Taylor, and B. G. Williams. Trajectory design and maneuver strategy for the MESSENGER mission to Mercury. *Journal of Spacecraft and Rockets*, 43 5:1054–1064, 2006. doi: 10.2514/1.18178.

[Mey99] Kenneth R. Meyer. *Periodic Solutions of the N-Body Problem*. Springer-Verlag, 1999.

[MW] J. K. Miller and Connie J. Weeks. Application of Tisserand's criterion to the design of gravity assist trajectories. Paper AIAA 2002-4717 AAS/AIAA Astrodynamics Specialist Conference and Exhibit, Monterey, GA, August 2002.

[PLB00] Anastassios E. Petropoulos, James M. Longuski, and Eugene P. Bonfiglio. Trajectories to Jupiter via gravity assists from Venus, Earth, and Mars. *Journal of Spacecraft and Rockets*, 37(6):776–783, 2000. doi: 10.2514/2.3650.

[Poi92] Henri Poincaré. *Les Méthodes Nouvelles de la Mécanique Celeste*. Paris, Gauthier-Villars et fils, 1892.

[PS06] Marci E. Paskowitz and Daniel J. Scheeres. Robust capture and transfer trajectories for planetary satellite orbiters. *Journal of Guidance, Control, and Dynamics*, 29(2):342–353, 2006. doi: 10.2514/1.13761.

[PYFN06] Jesús F. Palaciána, Patricia Yanguasa, Silvia Fernández, and Mariano A. Nicotra. Searching for periodic orbits of the spatial elliptic restricted three-body problem by double averaging. *Physica D: Nonlinear Phenomena*, 213:15–24, 2006.

[RJJ09] Shane D. Ross, S. Jerg, and O. Junge. Optimal capture trajectories using multiple gravity assists. *Communications in Nonlinear Science and Numerical Simulations*, 14(12):4168–4175, 2009. doi: 10.1016/j.cnsns.2008.12.009.

[RL03] Shane D. Ross and Martin W. Lo. Design of a multi-moon orbiter. In *Advances in the Astronautical Sciences*, volume 114, pages 669–684. Univelt, San Diego, 2003. Paper AAS 03-143.

[RL07] Ryan P. Russell and Try Lam. Designing ephemeris capture trajectories at Europa using unstable periodic orbits. *Journal of Guidance, Control, and Dyanmics*, 30(2):482 – 491, 2007.

[RS07] Shane D. Ross and Daniel J. Scheeres. Multiple gravity assists, capture, and escape in the restricted three-body problem. *SIAM Journal on Applied Dynamical Systems*, 6(3):576–596, Jan. 2007. doi:10.1137/060663374.

[SCR09] Nathan J. Strange, Stefano Campagnola, and Ryan P. Russell. Leveraging flybys of low mass moons to enable an Enceladus orbiter. In *Proceedings of the Astrodynamics Specialist Conference, Pittsburgh, PA*, Aug 2009. Paper AAS 09-435. Submitted to Journal of Spacecraft and Rockets.

[SL02] Nathan J. Strange and James M. Longuski. Graphical method for gravity-assist trajectory design. *Journal of Spacecraft and Rockets*, 39(1):9–16, 2002. doi: 10.2514/2.3800.

[SLS97] Jon A. Sims, James M. Longuski, and A.J. Staugler. V-infinity leveraging for interplanetary missions: Multiple-revolution orbit techniques. *Journal of Guidance, Control, and Dynamics*, 20(3):409–415, 1997. doi: 10.2514/2.4064.

[SPC99] J. Schoenmaekers, J. Pulido, and J. Cano. SMART-1 Moon mission: trajectory design using the Moon gravity. Technical Report SI-ESC-RP-5501, ESA, European Space Operation Center, Darmstadt, Germany, 1999.

[SS01] Nathan J. Strange and Jon A. Sims. Methods for the design of v-infinity leveraging maneuvers. In *Advances in the Astronautical Sciences*, volume 109, pages 1959–1976. Univelt, San Diego, 2001. also Paper AAS 01-437.

[SSL$^+$09] Nathan J. Strange, T. L. Spilker, D. F. Landau, T. Lam, D. T. Lyons, and J. J. Guzman. Mission design for the Titan Saturn System Mission concept. In *Astrodynamics Specialist Conference, Pittsburgh, PA*, Aug. 2009. Paper AAS 09-356.

[Swe93] Ted H. Sweetser. Jacobi's intergal and DV-Earth- gravity assist (DV-EGA) trajectories. In *Advances in the Astronautical Sciences*, volume 85, pages 417–430. Univelt, San Diego, 1993. also Paper AAS 93-635.

[Sze67a] V. Szebehely. *Theory of orbits. The restricted problem of three bodies.* New York: Academic Press, 1967.

[Sze67b] V. Szebehely. *Theory of orbits. The restricted problem of three bodies*, pages 557–587. New York: Academic Press, 1967.

[Tis96] Francois Felix Tisserand. *Traité de Méchanique Céleste*, volume 4, pages 203–205. Gauthier-Villars et fils, Paris, 1896.

[VC09] Massimilano Vasile and Stefano Campagnola. Design of low-thrust multi-gravity assist trajectories to Europa. *Journal of the British Interplanetary Society*, 62(1):15–31, Jan 2009.

[vKZA+05] Carlo von Kirchbach, Huan Zheng, Jeffrey Aristoff, Jonathan Kavanagh, Benjamin Villac, and Martin Lo. Trajectories leaving a sphere in the restricted 3-body problem. In *AAS paper 05-221*, 2005.

[VS03] Benjamin F. Villac and Daniel J. Scheeres. Escaping trajectories in the Hill three body problem and application. *Journal of Guidance, Control and Dyanmics*, 26(2):224–232, 2003. doi: 10.2514/2.5062.

Appendix A

Derivation of the phase-free formula

From Figure 3.2 we see that

$$v_L = 1 \pm v_{\infty L} \longrightarrow v_{\infty L}^2 = (v_L - 1)^2 \tag{1}$$

$$v_B = v_A \mp \Delta v_{AB} \longrightarrow v_B^2 = v_A^2 + (\Delta v_{AB})^2 \mp 2 v_A \Delta v_{AB} \tag{2}$$

with the upper sign referring to the exterior v_∞leveraging, and the lower sign referred to the interior v_∞leveraging. The velocity of the moon is $v_M^2 = k_P / a_M$. We start considering the leg $L - A$ (the dash lines in Figure 3.2).

From the vis-viva equation $\frac{1}{2} v_L^2 - 1 = -1/(1 + r_a)$ we obtain

$$r_A = \frac{v_L^2}{2 - v_L^2} \tag{3}$$

Note that

$$\frac{dr_A}{dv_L} = \frac{4 v_L^2}{\left(v_L^2 - 2\right)^2} = \frac{4 r_A^2}{v_L^3} \tag{4}$$

and

$$\frac{1}{r_A} = \frac{2}{v_L^2} - 1 \tag{5}$$

From the conservation of the energy and momentum respectively we have

$$\frac{1}{2}v_L^2 - 1 = \frac{1}{2}v_A^2 - \frac{1}{r_A} \longrightarrow 2\left(1 - \frac{1}{r_A}\right) = v_L^2 - v_A^2 \tag{6}$$

$$v_A = \frac{v_L}{r_A} \tag{7}$$

Using Eq. (5), we have

$$v_A = \frac{2 - v_L^2}{v_L} \tag{8}$$

We now use r_A in Eq. (3), v_A in Eq. (8), and $v_L$in Eq. (1) to define

$$\begin{aligned} \Gamma\left(v_{\infty L}\right) &\equiv \pm\left(r_A - v_A\right) = \pm\left(\frac{v_L^2}{2 - v_L^2} - \frac{2 - v_L^2}{v_L}\right) = \\ &= v_{\infty L}\frac{v_{\infty L}^3 \pm 3v_{\infty L}^2 - v_{\infty L} \mp 7}{v_{\infty L}^3 \pm 3v_{\infty L}^2 + v_{\infty L} \mp 1} \end{aligned} \tag{9}$$

Note that Γ is positive, monotonic strictly increasing function of $v_{\infty L}$ because $\Gamma(0) = 0$ and

$$\begin{aligned} \frac{d\Gamma}{dv_{\infty L}} &= \pm\frac{d\Gamma}{dv_L} = \frac{d\left(r_A - v_L/r_A\right)}{dv_L} = \frac{dr_A}{dv_L}(1 + v_L/r_A^2) - \frac{1}{r_A} = \\ &= \frac{4r_A^2}{v_L^3} + \frac{4}{v_L^2} - \frac{2}{v_L^2} + 1 = \frac{4r_A^2}{v_L^3} + \frac{2}{v_L^2} + 1 > 0 \end{aligned} \tag{10}$$

Now we consider the leg $H - B$.

Considering the triangle composed by v_M, $v_{\infty H}$ and v_H in Figure 3.1, and using the conservation of momentum:

$$v_{\infty H}^2 = 1 + v_H^2 - 2v_H\cos\gamma = 1 + v_H^2 - 2v_B r_A \tag{11}$$

From the conservation of the energy and from Eq. (6)

$$v_H^2 - v_B^2 = 2\left(1 - \frac{1}{r_A}\right) = v_L^2 - v_A^2 \longrightarrow v_H^2 = v_L^2 + v_B^2 - v_A^2 \qquad (12)$$

From combining Eq. (11) and Eq. (12) we get

$$\begin{aligned} v_{\infty H}^2 &= 1 + v_B^2 - v_A^2 + v_L^2 - 2v_B r_A = \\ &= 1 + \left(\Delta v_{AB}\right)^2 \mp 2v_A \Delta v_{AB} + v_L^2 - 2v_A r_A \pm 2\Delta v_{AB} r_A = \\ &= 1 + v_L^2 - 2v_L + \left(\Delta v_{AB}\right)^2 \pm 2\Delta v_{AB}\left(r_A - v_A\right) = \\ &= v_{\infty L}^2 + \left(\Delta v_{AB}\right)^2 \pm 2\Delta v_{AB}\left(r_A - v_A\right) \end{aligned} \qquad (13)$$

Using the function Γ defined in Eq. (9) we finally get

$$v_{\infty H}^2 = v_{\infty L}^2 + \Delta v_{AB}^2 + 2\Delta v_{AB}\Gamma$$

and also

$$\Delta v_{AB} = -\Gamma + \sqrt{\Gamma^2 + \left(v_{\infty H}^2 - v_{\infty L}^2\right)}$$

Note that we exclude the negative root as Δv_{AB} has to be positive.

On the sign of $\Gamma \frac{d\Gamma}{dv_{\infty L}} - v_{\infty L}$

First note that

$$\frac{d\Gamma}{dv_{\infty L}}\Gamma - v_{\infty L} = \frac{1}{2}\frac{d\left(\Gamma^2\right)}{dv_{\infty L}} - v_{\infty L} \qquad (14)$$

We recall that

$$r_A = \frac{v_L^2}{2 - v_L^2} = -\frac{2}{v_L^2 - 2} - 1 \tag{15}$$

$$v_A = \frac{v_L}{r_A} = \frac{2}{v_L} - v_L \tag{16}$$

So that

$$v_A^2 = v_L^2 + \frac{4}{v_L^2} - 4 = v_L^2 + 2\left(\frac{2}{v_L^2} - 1\right) - 2 = v_L^2 - 2\left(\frac{1}{r_A} - 1\right)$$

Also because $\frac{d}{dv_{\infty L}} = \pm \frac{d}{dv_L}$

$$\frac{dr_A}{dv_{\infty L}} = \pm \frac{dr_A}{dv_L} = \pm \frac{2v_L}{\left(v_L^2 - 2\right)^2} \tag{17}$$

Now let's compute

$$\begin{aligned}
\left(\Gamma^2\right) &= (r_A - v_A)^2 = r_A^2 + v_A^2 - 2r_A v_A = r_A^2 + v_L^2 - 2\left(\frac{1}{r_A} - 1\right) - 2v_L \\
&= r_A^2 + \frac{2}{r_A} + (v_L - 1)^2 - 3 = r_A^2 + \frac{2}{r_A} + (v_{\infty L})^2 - 3
\end{aligned}$$

Then

$$\begin{aligned}
\frac{d\Gamma}{dv_{\infty L}}\Gamma - v_{\infty L} &= \frac{1}{2}\frac{d\left(\Gamma^2\right)}{dv_{\infty L}} - v_{\infty L} = \frac{1}{2}\left(2r_A - \frac{2}{r_A^2}\right)\frac{dr_A}{dv_{\infty L}} + v_{\infty L} - v_{\infty L} = \\
&= \pm \frac{2v_L}{\left(v_L^2 - 2\right)^2}\left(\frac{r_A^3 - 1}{r_A^2}\right) = \pm\left(r_A^3 - 1\right)\frac{2v_L}{\left(v_L^2 - 2\right)^2}\frac{\left(v_L^2 - 2\right)^2}{v_L^4} = \left|r_A^3 - 1\right|\frac{2}{v_L^3} > 0
\end{aligned}$$

Appendix B

Coordinate transformations

In this appendix we recall the coordinate transformations for the CR3BP and some useful expressions used in the paper. The steps are standard and can be found in the literature[And05].

We start by recalling the coordinate transformation from the rotating reference frame centered in the barycenter, to the inertial reference frame centered in either body. We define the state vector in the rotating frame:

$$S = \left(X, Y, Z, \dot{X}, \dot{Y}, \dot{Z}\right)^T \tag{18}$$

the state vector in the inertial reference frame, centered in the barycenter:

$$s_{(B)} = \left(x_{(B)}, y_{(B)}, z_{(B)}, \dot{x}_{(B)}, \dot{y}_{(B)}, \dot{z}_{(B)}\right)^T \tag{19}$$

the state vector in the inertial reference frame, centered in either body:

$$s = (x, y, z, \dot{x}, \dot{y}, \dot{z})^T \tag{20}$$

We recall that all the variables are normalized using the scale factors defined in the paper, so that the angular velocity of the rotating frame is 1. Assuming the rotating frame has no initial phase w.r.t. the inertial frame, the transformation from S to $s_{(B)}$ is given by:

$$s_{(B)} = \left(X, Y, Z, \dot{X} - Y, \dot{Y} + X, \dot{Z}\right)^T \tag{21}$$

The transformation from $s_{(B)}$ to s is given by:

$$s = \left(x_{(B)} - d, y_{(B)}, z_{(B)}, \dot{x}_{(B)}, \dot{y}_{(B)} - d, \dot{z}\right)^T \tag{22}$$

where $d = -\mu$ if the inertial reference frame is centered in the major body, and $d = 1 - \mu$ if the inertial reference frame is centered in the minor body.

Thus the transformation from the rotating reference frame to the body-centered inertial reference frame and viceversa is given by the following equations:

$$(x, y, z, \dot{x}, \dot{y}, \dot{z})^T = \left(X - d, Y, Z, \dot{X} - Y, \dot{Y} - (X - d), \dot{Z}\right)^T \tag{23}$$

$$\left(X, Y, Z, \dot{X}, \dot{Y}, \dot{Z}\right)^T = (x + d, y, z, \dot{x} + y, \dot{y} - x, \dot{z})^T \tag{24}$$

In our work we are interested in the velocities in both reference frames. We first recall that the components of the velocity in the major/minor body reference frame are related to the magnitude of the angular momentum and inclination of the spacecraft w.r.t to the major/minor body through:

$$\dot{y}x - \dot{x}y = h \cos i \tag{25}$$

We use Eq.(24) and Eq. (25) to derive the an expression for the square of the velocity V^2:

$$V^2 = \dot{X} + \dot{Y} + \dot{Z} = (\dot{x} + y)^2 + (\dot{y} - x)^2 + \dot{z}^2 = v^2 + \left(x^2 + y^2\right) - 2h \cos i \tag{26}$$

Now we consider the special case in which :

$$s = (r_\pi \cos\theta, r_\pi \sin\theta, 0, -\sigma v_\pi \sin\theta, \sigma v_\pi \cos\theta, 0) \tag{27}$$

where $\sigma = +1$ for direct orbits and $\sigma = -1$ for retrograde orbits, and $r_\pi = R_2$ is the distance from the minor body.

Applying Eq. (24):

$$S = ((1-\mu) + r_\pi \cos\theta, r_\pi \sin\theta, 0, -\left(\sigma v_\pi - r_\pi\right)\sin\theta, \left(\sigma v_\pi - r_\pi\right)\cos\theta, 0) \tag{28}$$

so that

$$V = |\sigma v_\pi - r_\pi| = |v_\pi - \sigma r_\pi| \tag{29}$$

Assuming $v_\pi > r_\pi$, we find:

$$V = v_\pi - \sigma r_\pi \quad , \quad v_\pi = V + \sigma r_\pi \tag{30}$$

Tisserand Parameter, Jacobi constant, and v_∞

For completeness, in this appendix we derive the Tisserand parameter from the Jacobi constant. Similar derivations can be found in the literature[Tis96, MW].

Using Eq.(24) and Eq. (26) we express the Jacobi constant in the inertial reference frame centered in the major body:

$$J = \left((x-\mu)^2 + y^2\right) + 2\frac{1-\mu}{r} + 2\frac{\mu}{R_2} + (1-\mu)\,\mu - v^2 - r^2 + 2h\cos i \tag{31}$$

Using the *vis-viva* equation and the expression for the angular momentum

$$v^2 = 2\frac{1-\mu}{r} - \frac{1-\mu}{a} \tag{32}$$

$$h=\sqrt{a\left(1-e^2\right)(1-\mu)} \tag{33}$$

we find:

$$J=\frac{1-\mu}{a}+2\sqrt{a\left(1-e^2\right)(1-\mu)}\cos i+2\frac{\mu}{R_2}-x\mu+\mu^2+(1-\mu)\,\mu \tag{34}$$

If we let $\mu\rightarrow 0$, and assuming R_2 is not too small (as in the case when far from the minor body), Eq. (34) becomes:

$$J\approx\frac{1}{a}+2\sqrt{a\left(1-e^2\right)}\cos i=T \tag{35}$$

Now we assume that the spacecraft's orbit crosses the minor body orbit. At the crossing point, we can write the v_∞as:

$$v_\infty^2=1+v^2-2v\cos\gamma\cos i \tag{36}$$

where γ is the flight path angle. We recall the *vis-viva* equation for $r=1$ and $\mu\rightarrow 0$ and the expression of the angular momentum

$$\frac{1}{a}=2-v^2 \quad , \quad h=v\cos\gamma \tag{37}$$

to find:

$$\frac{1}{a}=2-v_\infty^2+1-2h\cos i \tag{38}$$

substituting Eq. (38) into Eq. (35) we finally find:

$$J\approx T=3-v_\infty^2 \tag{39}$$